2014

Phosphodiesterase Inhibition and Adenosine A2B Receptor Signaling in Mitochondrial Function: Pharmacology and Toxicology of 3-isobutyl 1-methylxanthine (IBMX) in the 661w Retina-Derived Cell Line

Anthony Presley Leonard
Medical University of South Carolina

Phosphodiesterase Inhibition and Adenosine A$_{2B}$ Receptor Signaling in Mitochondrial Function: Pharmacology and Toxicology of 3-isobutyl 1-methylxanthine (IBMX) in the 661w Retina-Derived Cell Line

Anthony Presley Leonard

A dissertation submitted to the faculty of the Medical University of South Carolina in partial fulfillment of the requirement for the degree of Biomedical Sciences in the College of Graduate Studies.

Department of Drug Discovery and Biomedical Sciences

2014

Approved by:

Chairperson, Advisory Committee

_____

_____

_____

_____

_____

_____

Copyright Notice

Dedication

This work is dedicated to my wife, Emily, for her steadfast support and for giving me the greatest gift in the world while writing this dissertation, our daughter Avery.

i. Acknowledgments

ii. Table of Contents

iii. List of Tables

iv. List of Figures

v. Key to Symbols, Abbreviations

- Ψ – membrane potential (generic)

- Ψ_m – absolute mitochondrial membrane potential

- $\Delta\Psi_m$ – mitochondrial membrane potential relative to a compartment of interest; in these studies, mitochondrial membrane potential is reported relative to that of the nucleus

- 2D – an image or array with two spatial and/or temporal dimensions (in the context of this work, an image with vertical (y) and horizontal (x) spatial dimensions)

- 3D – an image or array three spatial and/or temporal dimensions (in the context of this work, an image with vertical (y), horizontal (x), and depth of field (z) spatial dimensions)

- A_1 – Adenosine Receptor A_1 subtype (gene symbols: human ADORA1, mouse Adora1)

- A_{2A} – Adenosine Receptor A_{2A} subtype (gene symbols: human ADORA2A, mouse Adora2a)

- A_{2B} – Adenosine Receptor A_{2B} subtype (gene symbols: human ADORA2B, mouse Adora2b)

- A_3 – Adenosine Receptor A_3 subtype (gene symbols: human ADORA3, mouse Adora3)

- AC – adenylate cyclase

- ADP – adenosine 5'-diphosphate

- AL – Anthony Leonard (used to distinguish between classifying authors in Chapter 1)

- AMP – adenosine 5'-monophosphate

- ANOVA – analysis of variance

- ATP – adenosine 5'-triphosphate

- cAMP – cyclic adenosine 3'-5'-monophosphate

- cGMP – cyclic guanosine 3'-5'-monophosphate

- CNG – cyclic nucleotide-gated cation channel

- CNS – central nervous system

- CRAN – computerized R archive network; consortium of developers that maintain R computing language

- cRNA – complementary ribonucleic acid; Synthetic RNA produced by transcription from a specific DNA single stranded template.

- CREB – cAMP-response element binding protein

- CsA – cyclosporin(e) A

- CyD – cyclophilin D

- DAG – diacyl glycerol

- DAPI – 4',6-diamidino-2-phenylindole

- DCF – dihydrodichlorofluorescein, reactive oxygen species indicator

- DMEM – Dulbecco's modified Eagle's medium

- DMSO – dimethyl sulfoxide

- Drp1 – dynamin-related peptide 1, GTP-binding molecular motor that aids in mitochondrial membrane scission (fission)

- EGTA – ethylene glycol tetraacetic acid (EGTA)

- ELWD – extra-long working distance, characteristic of microscopic objectives that allow for imaging thick specimens

- ER – endoplasmic reticulum

- ETC – mitochondrial electron transport chain, composed of 5 multimeric Complexes, assigned Roman numerals I-V

- FCCP – carbonyl cyanide-p-trifluoromethoxyphenylhydrazone, protonophore and uncoupler of mitochondrial respiration

- FCS – fetal calf serum

- $G\alpha_s$ – G protein alpha subunit, stimulatory type

- $G\alpha_q$ – G protein alpha subunit, phospholipase-coupled

- $G\alpha_{11}$ – G protein alpha subunit, phospholipase-coupled

- GC – guanylate cyclase

- GMP – guanosine 5'-monophosphate

- GDP – guanosine 5'-diphosphate

- GTP – guanosine 5'-triphosphate

- GPCR – G protein-coupled receptor

- GSK-3β – glycogen synthase kinase 3, β isoform

- IBMX – 3-isobutyl 1-methylxanthine

- IP_3 – inositol 1,4,5-triphosphate

- MAPK – mitogen activated protein kinase

- MD – mitochondrial dynamics, combination of fission, fusion, biogenesis, mitophagy

- mRNA – messenger RNA

- MTDR – MitoTracker Deep Red™

- NA – numerical aperture, characteristic of microscopic objective lenses that describes ability of lens to capture light (and thus defines resolution)

- OCR – oxygen consumption rate

- PBS – phosphate buffered saline

- PDE – cyclic nucleotide phosphodiesterase (11 numbered isoforms in mouse and human, PDE1-PDE11)

- PI3K – Phosphatidylinositol-4,5-bisphosphate 3-kinase

- PIP_2 – Phosphatidylinositol 4,5-bisphosphate

- PKA – cAMP-dependent protein kinase (protein kinase A)

- PKC – protein kinase C, family of protein kinases; isoforms categorized by whether Ca^{2+}, DAG, or neither is necessary for activation

- PKG – cGMP-dependent protein kinase (protein kinase G)

- PLCβ – phospholipase C beta class (isoforms PLCβ1, PLCβ2, PLCβ3)

- PMA – phorbol myristate acetate

- PND – postnatal day (days after birth)

- PTP – mitochondrial permeability transition pore (also commonly in the literature as mPTP)

- QO_2 – oxygen consumption, mitochondria major intracellular consumer

- R – computer programming language; cran.us.r-project.org

- R – electrical resistance (only used in this context in **Equation 4-1** and **Equation 4-2**)

- RC – Robert Cameron (used to distinguish between classifying authors in Chapter 1)

- RNA – ribonucleic acid

- ROS – reactive oxygen species

- ROS – rod outer segments (not used in this context in this dissertation, but frequently in retina literature)

- RP – retinitis pigmentosa, an inherited retina degeneration

- sAC – soluble adenylate cyclase

- TBHP – tert-butyl hydroperoxide

- TBS – tris-buffered saline

- TMRM – tetramethylrhodamine methyl ester

- UDP – uridine diphosphate

vi. Abstract

ANTHONY PRESLEY LEONARD. Phosphodiesterase Inhibition and Adenosine A_{2B} Receptor Signaling in Mitochondrial Function: Pharmacology and Toxicology of 3-isobutyl 1-methylxanthine (IBMX) in the 661w Retina-Derived Cell Line. (Under the direction of Bärbel Rohrer and Craig Beeson)

3-isobutyl 1-methylxanthine (IBMX) is a commonly used inhibitor of cyclic nucleotide phosphodiesterases (PDE) and G protein coupled adenosine receptors. Administration of IBMX to retina photoreceptor-derived 661w cell line results in decreased mitochondrial respiration followed by cell death, mimicking phenomena observed in inherited retina neurodegeneration in humans and animals and thus suggesting their use as a cell-based model of retina degeneration. In this dissertation, the temporal relationship between pathways altered by IBMX and how these pathways affect mitochondrial physiology are evaluated. These studies utilize a novel high content microscopic method for simultaneously measuring mitochondrial morphology and membrane potential in living cultured cells to identify an increase in networked morphology (pro-fusion) and mitochondrial membrane potential within 1-4 h of IBMX administration that is sustained and accompanied by decreased uncoupled respiration at 24 h. cGMP PDE inhibition was observed to recapitulate both the immediate and sustained physiological alterations as selective inhibitors of PDE3 and PDE5 increased mitochondrial membrane potential and interconnected morphology at 1 h which was followed by a decrease in mitochondrial respiration at 24 h similar to that elicited by IBMX. Administration of selective inverse agonist of adenosine A_{2B} receptor

recapitulated the latent (24 h), but not early (1 h) IBMX-induced alterations in mitochondrial physiology. Administration of a selective agonist and antagonist prior to IBMX abrogated latent but not early IBMX-induced alterations. A similar pattern of reductions in latent but not early alterations were achieved by activating adenylate cyclase or protein kinase C. Inhibition of protein kinase A resulted in increased mitochondrial membrane potential at 1 h and 24 h. The concomitant increase of mitochondrial membrane potential with decreased respiration suggested decreased permeability of the mitochondrial inner membrane to inward proton flux, perhaps due to lack of ADP availability or decreased mitochondrial Complex V activity. Inhibiting mitochondrial permeability transition pore (mPTP) regulator GSK-3β prior to IBMX administration prevented increases in both membrane potential and networked morphology, suggesting GSK-3β activation follows IBMX. Taken together, this work demonstrates that IBMX first increases cGMP via inhibition of PDEs at 1 h to modulate a rise in mitochondrial membrane potential and networked morphology, followed by inverse agonism at the adenosine A_{2B} receptor at 24 h. Downstream pathways invoked at 24 h include decreased adenylate cyclase and PKA signaling, as well as PKC. GSK-3β activation following loss in PKA and PKC activity may integrate these PDE- and adenosine A_{2B} receptor-dependent signals.

1.   Introduction

These studies use a cell-based model of retina mitochondrial dysfunction, in which concentration-dependent decreases in mitochondrial respiratory capacity (which corresponds to maximal ability to produce ATP [2]) occur following 24 h administration of IBMX (3-isobutyl 1-methylxanthine) to 661w photoreceptor cells, followed by cell death at 48 h [3, 4]. Although this model recapitulated mitochondrial dysfunction prior to cell death featured in rodent models of inherited retinal degeneration, the upstream mechanism or mechanisms by which IBMX leads to these cell-death associated decreases in mitochondrial respiration were unknown.

The present work uses a high content imaging assay for mitochondrial morphology and function (**Section 3—Chapter 1**) to demonstrate that losses in mitochondrial respiratory capacity at 24 h and cell death at 48 h are preceded by mitochondrial membrane hyperpolarization and an increase in networked morphology as early as 1-4 h following IBMX treatment (**Section 4—Chapter 2**). Next, the modes of action of IBMX on two pharmacologically relevant target classes are evaluated: cyclic nucleotide phosphodiesterases (PDE, discussed in **Section 5—Chapter 3**) and the G protein-coupled receptor adenosine A_{2B} receptor (Adora2b, discussed in **Section 6— Chapter 4**).

Taken together, these results lead to the hypothesis that IBMX alters mitochondrial physiology via two distinct modes of action – inhibition of phosphodiesterases and inverse agonism of the adenosine receptor A_{2B} (Adora2b) – and that these distinct pathways show the potential for crosstalk as well as for

convergence on common downstream mediator GSK-3β to effect changes in

mitochondrial physiology.

2.   Review of Literature

2.1   Mitochondrial Function and Retina Neurodegeneration

In humans, the typical course of the inherited retina neurodegenerative disease retinitis pigmentosa (RP) is characterized by a progressive loss of rod photoreceptors, leading to symptoms of decreased peripheral vision and night vision over months to decades. After loss of peripheral vision, many patients will also lose central vision [5]. RP comprises 50% of all inherited retina degenerations, which as a whole affect 200,000 Americans. Highly heterogeneous in its genetic etiology, RP may appear by itself or as part of a syndrome or other complex disease (e.g. Usher, Bardet-Biedl). The Retina Information Network (RetNet) to date has identified 252 genes and loci associated with diseases and syndromes that feature inherited retina degeneration, 57 of which are associated with isolated RP (accessed May 1, 2014: https://sph.uth.edu/retnet). 3100 mutations have been identified in these genes associated with isolated RP, and RP arising from just Usher or Bardet-Biedl syndromes alone are associated with 1200 mutations in 29 genes. This genetic diversity leads to not only difficulty in identifying the genotype associated with RP, but highlights the difficulty of developing a single therapy to treat a genetically heterogeneous disease. As an example, even with modern deep sequencing methodologies, successful identification of a mutation is achieved in only 80% of patients, whereas with more common genotyping strategies identification may be as poor as 30% [6].

Therapeutic strategies for RP may be broadly classified into two categories: those which aim to protect still living photoreceptors from degeneration (e.g. gene

3

therapy to correct loss of function mutations, neuroprotective drugs, and biologicals),

and those that aim to recover loss of retina function (e.g. stem cell transplantation,

regeneration, optogenetic modification of surviving retina neurons) [7]. Although the

retina is particularly amenable to gene therapy approaches due to its immunoprivileged

status and ease of access via its anatomical location [8], the genetic heterogeneity of RP

suggests that either a single gene replacement therapy or a series of gene replacement

therapies will likely face significant research, development, and/or regulatory hurdles in

seeking approval. Thus, the identification of common phenotypic features amongst

heterogeneous genotypes of RP is of paramount importance as such work may identify

common targets to perturb that may mitigate or eliminate disease progression.

Furthermore, support of these common phenotypic features may synergize with

regenerative strategies or support cellular function in gene therapy strategies.

One common phenotype of RP is bioenergetic failure as evidenced by decreases

in mitochondrial function that is succeeded by cellular death. Indeed, mutations in

nuclear or mitochondrial genes encoding for mitochondrial proteins often feature retina

degenerative phenotypes in humans, such as Kearns-Sayres syndrome, Leber's

hereditary optic neuropathy, and Leigh syndrome [9]. Several groups have characterized

that mitochondrial dysfunction is common to several mouse models of RP resulting from

mutations in non-mitochondrial genes, including PDE6b$^{rd1/rd1}$, Rho$^{-/-}$, PDE6b$^{atrd1/atrd1}$, and

Prph2$^{rds/rds}$ [10]. The best characterized animal model of RP, the rd1 mouse

(PDE6b$^{rd1/rd1}$), is characterized by a rapid death of rod photoreceptor cells beginning at

postnatal day (PND) 15 [5, 11-14]. However, as early as at PND 11 in the rd1 mouse,

intramitochondrial Ca^{2+} (Ca$^{2+}_m$) levels significantly rise as evidenced by increased Rhod2

fluorescence intensity [15].

Based on these studies, it was hypothesized that support of mitochondrial function, and thus maintaining bioenergetic capacity, may serve as a therapeutic option for photoreceptor neurodegeneration. To evaluate this hypothesis, the Rohrer lab developed a cell-based model of retina degeneration that mimics the mitochondrial dysfunction preceding cell death. Briefly, in this model, following administration of 3-isobutyl-1-methylxanthine (IBMX) to the 661w photoreceptor cell line, loss in mitochondrial respiratory capacity occurs at 24 h followed by cell death at 48 h [4]. This sequence recapitulates the sequence observed in RP.

2.2   3-isobutyl 1-methyl xanthine (IBMX)

IBMX is a commonly used non-selective small molecule inhibitor of cyclic nucleotide phosphodiesterase (PDE) enzymes and adenosine receptors (ADOR) [16, 17]. Our lab previously published that administration of 1 mM IBMX leads to an increase in reactive oxygen species (ROS) as evidenced by increased fluorescence intensity of redox-sensitive dye dihydrodichlorofluorescein (DCF) as early as 15 min, calpain activation as early as 1 h and caspase activation as early as 6 h [3]. Any one of these changes in and of themselves may lead to mitochondrial dysfunction by damage of electron transport chain (ETC) proteins. However, the upstream regulation of these effectors of cell death is poorly understood as are other relevant pathways that may mediate cellular mitochondrial dysfunction. Thus, it is the **goal of this work to characterize the role of IBMX-induced alterations in PDE activity and adenosine receptor signaling, two early-stage events that may be directly modulated by IBMX administration**.

2.3   The 661w Photoreceptor Cell Line

The 661w cell line was first generated by the generation of a transgenic mouse line expressing the viral oncoprotein SV40 T antigen driven by the human IRBP (interphotoreceptor binding protein) promoter. These mice developed spontaneous, bilateral tumors in the brain and retina [18]. Cells from these tumors were found to survive in culture and later characterized to express a number of photoreceptor proteins [19]. When transfected with RPE65 hydrolase, 661w cells were determined to cycle exogenously administered 11-cis retinol to all-trans retinal, indicating functional activity of the phototransduction cascade [20]. However, 661w cells lack some key members of the phototransduction cascade, including subunits of the cyclic nucleotide gated-cation channel (CNG) [21, 22]. Investigations confirmed that 661w cells do not conduct a plasma membrane current in response to stimulation of this channel by exogenously administered IBMX, cGMP, or activation of guanylate cyclase with nitric oxide donors (**Supplementary Figure 11**). Further studies using Ca^{2+}-sensitive dye Fluo-4 AM demonstrated no increase in intracellular Ca^{2+} following IBMX administration (unpublished results). Therefore, early-onset changes in 661w cell physiology as a result of IBMX administration are not likely due to increased Ca^{2+} current through CNG but are instead due to alteration of other intracellular pathways, including elevation of intracellular concentrations of cAMP and/or cGMP.

Of importance to note is that in the absence of CNG channel-mediated influx of Ca^{2+} into the cytoplasm, 661w cells may be able to achieve even greater intracellular cGMP accumulation. Ca^{2+} influx normally inactivates guanylate cyclase (GC), a negative feedback mechanism which offsets the increase induced by inhibition of cGMP-specific PDE's [23]. Evidence of this feedback mechanism in photoreceptors has been demonstrated; administration of PDE inhibitors to purified rod outer segments resulted in

6

only 20-30% increases in intracellular cGMP in the absence of Ca^{2+} buffer EGTA but when EGTA was included, 400% increases were observed, suggesting compensatory GC inactivation was overcome by removing Ca^{2+} stimulus [24].

2.4 Cyclic Nucleotide Phosphodiesterases (PDE) and Retina Neurodegeneration

Cyclic nucleotide phosphodiesterase (PDE) enzymes are present in virtually all tissues and catalyze the conversion of one or both biological cyclic nucleotides cyclic adenosine monophosphate (cAMP) and cyclic guanosine monophosphate (cGMP) into their non-cyclic forms (AMP, GMP) [25]. In humans, there are 11 PDE isoforms which are each comprised by one or more subunits encoded by one gene for each. Although the PDEs have been primarily popularized as a drug target by the advent of PDE5 inhibitors to treat erectile dysfunction, other PDEs play important physiological roles [26, 27]. In the retina, two distinct trimeric isoforms (one in rods, one in cones) of PDE6 aid in the transduction of light to a neuronal (electrical) signal by loss of inhibition via their gamma, or inhibitory subunits, following binding of the G protein alpha subunit transducin. Thus, when stimulated by light, the G protein coupled receptor cone opsin (or rhodopsin in rods) leads to PDE6 activation, catalyzing the turnover of cGMP, which subsequently leads to the closure of cGMP-cated cation channels to stop the influx of Ca^{2+} into the cell. This cessation of Ca^{2+} hyperpolarizes the photoreceptor, which is interpreted by multiple downstream neurons as light.

In the rd1 mouse (also known as C3H or rd), a non-sense mutation in the β, or catalytic, subunit of PDE6, PDE6B[rd/rd], leads to rapid photoreceptor death characterized both by increased intracellular Ca^{2+} and cGMP [11-14, 28, 29]. Interestingly, however, either pharmacological or genetic inhibition of the CNG channel in the rd1 mouse have each been demonstrated to achieve only partial recovery against photoreceptor cell

7

death [30, 31]. Further evidence suggests that protein kinase G (PKG, another cGMP-activated protein) activation in the absence of CNG-mediated Ca^{2+} influx is toxic to photoreceptors in that pharmacologic inhibition of PKG partially rescued rd1 retina explants against photoreceptor cell death and activation of PKG in wild type retina explants induced cell death [32]. These findings are important as in the IBMX/661w model of photoreceptor degeneration there is no Ca^{2+} influx owing to the absence of CNG channels (**Supplementary Figure 11**), and highlights the possibility that cGMP/PKG may mediate the cytotoxicity observed.

Sparked by multiple reports that PDE5 inhibitor sildenafil has toxicity issues in some humans (patients report seeing blue), Nivison-Smith et al. studied sildenafil exposure in rd1 mice. Firstly, they demonstrate that electroretinogram (ERG) responses in wild type mice experience a dose-responsive decrease following sildenafil exposure which typically recovered within two days. They showed that mouse carriers (heterozygous) for the rd1 mutation in PDE6B (PDE6Brd1/wt) in comparison to wild type controls displayed a prolonged (2 week) decrease in ERG responses following exposure to PDE5 inhibitor sildenafil. Additionally, retinas showed an increase in cytochrome C expression [33]. These data lend credence to the hypothesis that inhibition of cGMP-specific phosphodiesterase enzymes (PDE5 and PDE6) and the subsequent increase in intracellular [cGMP] leads to mitochondrial dysfunction.

3'-5' cyclic guanosine monophosphate (cGMP) is a common intracellular messenger best known for its vasodilatory effects in response to endothelial cell-derived nitric-oxide in turn activating cGMP synthesis in vascular smooth muscle via activation of guanylate cyclase [34]. However, cGMP has tissue- and subcellular-specific roles as well. Its role in photoreceptor cell phototransduction and viability in retina degeneration has been discussed earlier. cGMP has been shown to modulate signaling events as

diverse as neuronal long-term potentiation (important for learning) [35] and renal mitochondrial biogenesis [36]. Therefore, measuring the concentration of cGMP alone is not predictive of cellular response, as both the tissue and subcellular context are of paramount importance. The role of subcellular compartmentalization of these cyclic nucleotides, their generators adenylate/guanylate cyclase, and their resolvers the PDEs has been underscored in a recent review [37]. For instance, PDE5 has been shown to localize to the plasma membrane, ER, and cytoplasm. In these three compartments, respectively, PDE5 has been shown to have an effect in cardiac myocyte contractility, platelet aggregation, and cardiac contractility. PDE3A and PDE3B demonstrate even more complex and varied subcellular localization patterns that result in the regulation of processes as varied as cardiac/myocyte contractility, plasma membrane potential, vesicular transport, and insulin-mediated lipolysis. Quite interestingly, PDE4A and PDE4B have even been reported to bind to mitochondrial A kinase anchoring protein AKAP149 in T lymphocytes [38], mutations in which result in a more fissioned mitochondrial morphological phenotype in HeLa cells [39]. Further evidence for a linkage between cAMP elevation and increased mitochondrial network elongation has been demonstrated by Merrill et. al. in that PC12 cells exogenously administered a cell-permeable analog of cAMP or forskolin increased mitochondrial length [40].

2.5 Adenosine Receptor Function

Adenosine signaling is an important regulator of myriad physiological functions, from wakefulness and metabolic regulation in the central nervous system (CNS) and heart, and from photoreceptor coupling (increasing sensitivity to dim light at the cost of resolution) in the retina to mitochondrial susceptibility to damage following ischemia/reperfusion injury in central nervous system, heart, and kidney [41-44].

Signaling through extracellular release of adenosine or conversion of extracellular ATP to adenosine are two methods by which plasma membrane adenosine receptors may be activated [45]. Adenosine and its biological or pharmacological derivatives bind to a number of extracellular G protein-coupled receptors (GPCRs) and ligand-gated ion channels split into three broad classes. The first major class of adenosine-binding receptors are deemed the P2X receptors, and are oligomeric ion channels activated by various phosphorylated purines and pyrimidines (e.g. adenosine di- and tri-phosphate [ADP, ATP], and uridine diphosphate [UDP] and UDP-glucose). P2Y receptors are the second major class of purine phosphate-binding receptors, and are GPCRs displaying low affinity for unmodified adenosine. The P1, or simply termed adenosine receptor class, is represented currently by four GPCRs, the A_1, A_{2A}, A_{2B}, and A_3 adenosine receptors. Each receptor has varying specificity as to which G protein subunit(s) it couples to, and are involved in diverse intracellular signaling mechanisms within the cell (**Table 6-1**). As the xanthine derivative 3-isobutyl 1-methylxanthine (IBMX) has been previously described to inhibit the P1 or adenosine receptor subclass, and this subclass has been linked to the regulation of mitochondrial physiology, the studies in this dissertation will focus on understanding the role of P1 adenosine receptor signaling.

Regulation of A_{2B} signaling kinetics, like most GPCRs, is multifactorial; an important regulatory step in desensitization is manifest in post-translational modification of the A_{2B} receptor by beta adrenergic receptor kinase 1 (BARK1/GRK2) [46], and by subsequent or independent regulation of its internalization/subcellular localization by arrestins or other known mechanisms of GPCR regulation [47].

Indeed, retinal adenosine regulates retinal vascular function like it does in the heart and central nervous system, as well as regulating intraocular pressure [48]. Namely, agonism of adenosine receptors results in vasodilation and decreased

10

intraocular pressure. Although not a direct link between adenosine and retinal vasomotor

responses, Brandli and Stone provide an argument for a soluble mediator (perhaps

adenosine) by demonstrating that 10 min of ischemia induced in the hindlimb of rats

resulted in significant (14%) increases in the a wave and b wave of the electroretinogram

despite no changes in system vascular response (blood pressure, heart rate, oxygen

saturation) [49].

In the teleost retina, cone photoreceptor cells undergo elongation and shortening

in a circadian pattern as a means of regulating sensitivity. Burnside et. al. showed that

this process of myoid elongation is regulated by an A_2-like adenosine receptor [50].

Activities of both the high-affinity A_{2A} and a low-affinity (likely A_{2B}) receptor were

demonstrated in bovine rod outer segments, but the A_{2B} subtype predominated in retinal

pigment epithelium [51, 52].

2.6   RGC-5 Is a Subclone of the 661w Cell Line

Very interestingly, a series of recent reports have demonstrated that the cell line

RGC-5, originally characterized as a rat retina ganglion cell line [53], actually arose out

of contamination in the originator's lab with the murine 661w cell line [54, 55], leading to

retraction of the former publication characterizing the cell line. Therefore, many of the

publications using this cell line (which number 246 by keyword search "RGC-5" in

MEDLINE at time of writing) may indeed be indicative of 661w (photoreceptor)

physiology, and not that of retina ganglion cells. Of particular interest is a 2007

publication using the RGC-5 cell line that demonstrated an increase in fissioned

mitochondrial morphology, mitochondrial localization of Drp1 and decreased cellular

ATP content following culture at 30 mmHg pressure (to simulate increased intraocular

pressure seen in glaucoma) [56]. In a subsequent study, the same lab demonstrated

Opa1 (fusion protein) and cytochrome c release from mitochondria cytoplasm and

activation of caspase 3 and apoptotic cell death following elevation of hydrostatic pressure [57]. Together, these studies demonstrate the feasibility of measuring mitochondrial morphology in 661w and highlights the possibility that increased hydrostatic pressure alone (in the absence of ischemia) may alter mitochondrial bioenergetics.

2.7 Regulation of Mitochondrial Morphology

Mitochondrial morphology is an actively regulated and dynamic feature altered by a number of molecular processes which can be generally segregated into two categories: those that promote fission and those that promote fusion. Small dynamin-like GTPase protein dynamin-related protein 1 (Drp1) assembles into a molecular motor that forms constricting rings around the mitochondrial outer membrane, utilizing energy derived from GTP hydrolysis to aid in membrane scission, or simplification of mitochondrial networks into smaller, simpler shapes (e.g. rod-like, puncta). Regulation of Drp1 occurs via several upstream modulators, including isoforms of cAMP-dependent protein kinase (PKA) and phosphatase PP2A [40, 58-63], translocation of Bax [63], and ubiquitylation by E3 ubiquitin ligase parkin [64]. The physiological importance of Drp1 is underscored as mutation in mice leads to embryonic lethality, and a single case report in a human neonate describes classical mitochondrial defects (lactic acidemia, abnormal brain development, and optic atrophy) prior to lethality at 37 days [65, 66]. On the other hand, the molecular motors that regulate mitochondrial membrane fusion serve at two distinct subcellular locations, the mitochondrial outer membrane and the mitochondrial inner membrane. Outer membrane regulators include mitofusin 1 (Mfn1) and mitofusin 2 (Mfn2) while inner membrane fusion (and therefore cristae structure) is regulated by the protein optic atrophy 1 (Opa1) [67-69].

Frequently, mitochondrial morphology has been characterized by manual scoring. In an effort to reduce the selection bias and observer bias made necessary by the laborious process of manual inspection, a method was developed to classify and measure mitochondrial morphology, and is described in **Section 3, Chapter 1— Quantitative Analysis of Mitochondrial Morphology and Membrane Potential in Living Cells Using High Content Imaging, Machine Learning, and Morphological Binning**.

3. Chapter 1—Quantitative Analysis of Mitochondrial Morphology and Membrane Potential in Living Cells Using High Content Imaging, Machine Learning, and Morphological Binning

3.1 Highlights

- Automated analysis of mitochondrial morphology & membrane potential in live cells

- Mitochondrial shapes fit in four "bins": punctate, rod, networked and large & round

- Machine learning-derived algorithm categorizes mitochondria into morphological bins

- Automated assessment of mitochondria-specific membrane potential ($\Delta\Psi_m$) using TMRM

- Large and round category represents mitochondrial swelling

3.2 Abstract

Understanding the processes of mitochondrial dynamics (fission, fusion, biogenesis, and mitophagy) has been hampered by the lack of automated, deterministic methods to measure mitochondrial morphology from microscopic images. A method to quantify mitochondrial morphology and function is presented here using a commercially available automated high content wide field fluorescent microscopy platform and R programming language-based semi-automated data analysis to achieve high throughput morphological categorization (puncta, rod, network, and large & round) and quantification of mitochondrial membrane potential. In conjunction with cellular respirometry to measure mitochondrial respiratory capacity, this method detected that

increasing concentrations of mitochondrial toxicants (t-butyl hydroperoxide [TBHP], rotenone, antimycin A, oligomycin, ouabain, and carbonyl cyanide-p-trifluoromethoxyphenylhydrazone [FCCP]), decreased mitochondrial networked area in cultured 661w cells by 20-60% at concentrations that inhibited respiratory capacity 30-80%. Mitochondrial swelling was indicated by 40-130% increases in large & round areas in response to TBHP, oligomycin, or ouabain. The automated identification of mitochondrial location enables accurate quantification of mitochondrial membrane potential by measuring tetramethylrhodamine methyl ester (TMRM) fluorescence intensity specifically within mitochondria. Administration of 1 µM FCCP or 10 µM oligomycin resulted in depolarization and hyperpolarization of mitochondria, respectively, as evidenced by changes in intramitochondrial TMRM fluorescence intensities to 10% and 300% of vehicle control values. In summary, this method demonstrates sensitivity to rapidly and accurately quantify mitochondrial morphology and membrane potential in hundreds of thousands of cells on a per-cell basis, with sufficient throughput for pharmacological or toxicological evaluation.

3.3 Introduction

Mitochondrial morphology is an actively regulated and dynamic feature altered via mitochondrial dynamics (MD) – the combination of mitochondrial fission, fusion, biogenesis, and mitochondrial autophagy (mitophagy). These changes have been associated with regulation of oxidative metabolism, calcium homeostasis, and apoptotic or necrotic cell death [69, 70].

The evaluation of mitochondrial morphology using microscopy was originally limited to electron microscopy and manual classification. The development of multi-photon microscopy and fluorescent dyes, coupled with high-definition videography, greatly improved the observation of MD. However, the scale of mitochondrial content

within cells makes manual classification and quantification prohibitive; the ~100

individual mitochondria observed within each cell translates to > 10^4 mitochondria per

high power (40 x) microscopic field. Furthermore, quantification of mitochondrial

morphology across a series of experiments quickly scales the volume of data and

complexity of the analysis. Due to these limitations, many researchers report

mitochondrial morphology via display of representative fields per treatment group and

without robust quantification. Consequently, throughput is insufficient and the resultantly

small subsets of mitochondria evaluated may be affected by sampling bias.

Previous studies using microscopy and computational image analysis, commonly

referred to as High-Content Microscopy or Image Cytometry, demonstrate the strength

of this approach with regards to limiting observer and selection bias in morphological

evaluations while increasing throughput [1, 71-75]. While several groups have made

efforts to apply high-content fluorescence microscopy to the task of mitochondrial

morphological evaluation [71-75], only the approach of Koopman et. al. has

demonstrated the throughput necessary for pharmacological/toxicological evaluation

[75]. However, by looking at morphometric measures across the diverse range of

mitochondrial morphological subtypes in aggregate, that approach loses power to detect

subtler changes in interconnectedness, and is not well suited to quantify the abundance

of rare subtypes.

The method presented here for analyzing individual mitochondrial morphologies

is capable of large-scale mitochondrial measurement; that is to say millions to billions of

mitochondria across thousands of cells can be classified within a single experiment

according to mitochondrial interconnectedness and complexity. This was achieved

through automated live-cell wide-field fluorescence imaging coupled with image-based

computational high content analysis and the use of a classifier developed using machine

learning to segregate mitochondria into four categories [76]. The method is further extended to observe changes in mitochondrial membrane potential ($\Delta\Psi_m$).The development of a deterministic fully automated algorithm allows for evaluation of entire cellular populations within multiple replicate microscopic fields across repeated experiments, resultantly improves throughput, reduces observer and sampling bias, and advances the field of mitochondrial biology.

3.4 Materials and Methods

3.4.1 Cell culture

661w photoreceptor cells were generously provided by Dr. M. Al-Ubaidi (University of Oklahoma) [18] and maintained under standard conditions using DMEM-HG media (Sigma-Aldrich #D-7777) supplemented with 10% fetal calf serum (FCS, Atlanta Biologicals #S11550) and 1 mM L-alanyl-L-glutamine (GlutaMAX™, Life Technologies #35050-061). Cells of passages 15-25 were cultured to 80% confluency before trypsinization and seeded at a cell density of 8,000 cells per well in 96 well plates (Nunc Edge Plate, Thermo Scientific #167314) supplemented with 5% FCS and edge reservoirs filled with 1x phosphate buffered saline, (PBS, Life Technologies #14080-055). After allowing cells to reach 80% confluency (24 h), cells were washed in PBS, and media was changed to DMEM with 5.5 mM glucose without phenol red (Sigma-Aldrich #D-5030) supplemented with 1% FCS to induce cell cycle arrest. Cells were used for experiments 24 h after this switch to normal glucose and 1% FCS-containing media, with treatments for either 24 h (morphological analysis) or 1 h (membrane potential analysis). All compounds used for treatment were from Sigma-Aldrich (St. Louis, MO) unless otherwise specified, and were prepared at 1000x concentration in DMSO before administration to cells (final [DMSO] = 0.1%).

3.4.2 Live Cell Staining

Cells were stained with Hoechst 33342 (Anaspec #83218), and MitoTracker Deep Red FM (MTDR, Life Technologies #M22426). After determining the lowest dose of dye necessary to acquire high signal to noise ratio (>3) images while maintaining exposure times under 1 sec, cells were stained for 30 min at 37° C with the above dyes in phenol-red free DMEM supplemented with 1% FCS (Hoechst at 10 µM and MTDR at 50 nM), after which the media was replaced for imaging. It is important to note that while membrane potential drives loading of MTDR into mitochondria, once covalently bound to mitochondrial proteins its distribution is relatively insensitive to subsequent changes in polarization or acidification (such as that encountered by mitochondria undergoing autophagy in the lysosome). Mitochondrial retention despite depolarization (see **Supplementary Fig. 1b**) is afforded by a chloromethyl moiety that covalently binds protein sulfhydryls; whereas its insensitivity to acidic changes in pH is based on the fact that MTDR's fluorophore is a delocalized cationic enamine with a pKa comparable to that of an amide (~14).

3.4.3 Image Acquisition and Analysis: Overview

Briefly, 661w photoreceptor cells cultured on 96-well plates were stained with Hoechst 33342 and MTDR, and imaged using wide-field fluorescence microscopy (see **Figure 3-1a** and **Section 3.4.4, Automated Microscopy—Step 1: Image Acquisition**). A z stack of seven images was collected of MTDR-stained mitochondria and 2D deconvolution applied to the stack to output a single in-focus field with out-of-focus information removed (a process that simulates confocal microscopy). Mitochondria were identified from deconvolved and preprocessed images using the "object" segmentation algorithm in GE INCell Developer Toolbox 1.9.1, a variation of the "top hat" approach to segmentation (**Figure 3-1b-c**). Developer Toolbox is available within the GE INCell

Investigator 1.6.1 software package (GE Healthcare Bio-Sciences, Pittsburgh, PA. As

mitochondria display a variety of shapes which indicate interconnectedness and health,

four categories were established: puncta, rod, networked, large & round. Rods are an

intermediate phenotype between puncta and networks. The large & round group likely

represents a combination of pathologically swollen mitochondria as well as normal

mitochondria undergoing fission or fusion (see **3.6, Discussion**). To automate

classification of mitochondria into these bins, 1386 mitochondria were manually

classified, and a subset of 897 with 35 morphometric measures calculated on each then

used to train a classifier using conditional inference recursive partitioning [76]. The

remaining 489 (test data, not used to train classifier) were used to test its performance.

The R code as well as training and test data sets are included in **Section 9: Appendix

B—Computer Programs**. Decision tree output is shown in **Supplementary Figure 2**.
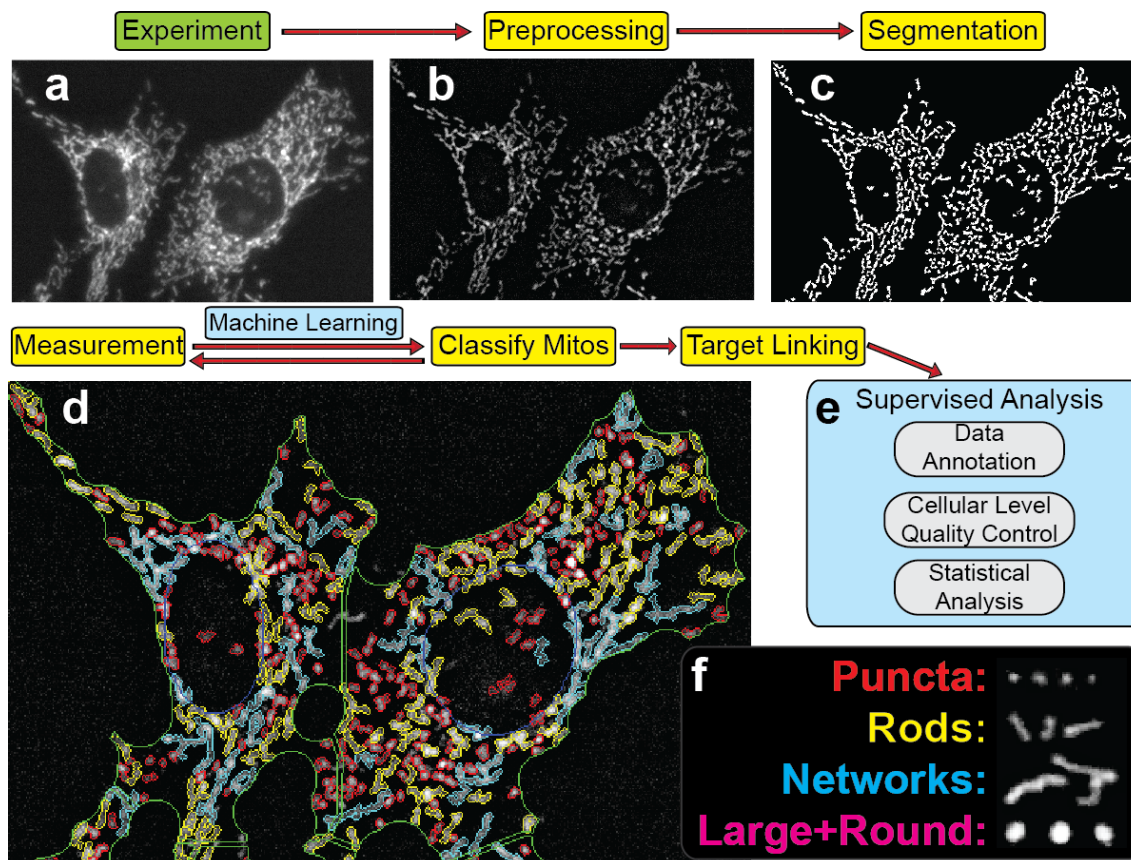
Figure 3-1. Overview of morphological binning-based analysis of mitochondrial morphology.

Automated wide-field fluorescence microscopy (**a**) was followed by preprocessing (2D deconvolution, intensity normalization) (**b**), segmentation (identification of mitochondria) (**c**), and classification of mitochondria into 4 morphological subtypes (puncta, rods, networks, and large & round) (**d,** colors defined in **f**) using a machine learning-based classifier. Morphological measures for each subtype (area, count, length, etc.) were calculated and then aggregated on a per-cell basis (target linking). Per-mitochondrion quality control was achieved by exclusion of small, dim objects (junk category defined in **Supplementary Figure 2**). Data were annotated with experimental meta-data (treatment, concentration, plate, etc.) to achieve unsupervised and supervised exclusion of low-quality cells and microscopic fields (out of focus, poorly stained) to facilitate statistical analysis using new scripts developed in the R platform (**e**). Examples of mitochondrial subtypes – puncta are small and round, rods are elongated, and networks are further elongated. Large and round are distinctly larger than puncta but still round (**f**).

3.4.4 Automated Microscopy—Step 1: Image Acquisition

Wide-field fluorescent imaging of live cells was coupled with off-line deconvolution of MTDR-stained mitochondria to increase acquisition speed but maintain adequate lateral spatial resolution (Rayleigh: 717 nm; Nyquist: 555 nm) (**Figure 3-1a**). Stained cells were imaged using filters corresponding to each dye and polychroic mirror ("X", QUAD1) on the GE INCell 2000 Analyzer automated wide field fluorescence microscope. The objective used was a 40x Nikon ELWD NA 0.6 matched with the large-

format 2048x2048 pixel 12-bit Coolsnap K4 camera (z/sampling height 1.55 µm, xy/lateral pixel dimensions of 0.185 µm). Resolving small objects near resolution limits like mitochondria requires high signal to noise ratio imaging. To achieve this, seven images were acquired in a z-stack, each image 1.55 µm apart on the Cy5 filter set (MTDR-stained mitochondria) to enable 2D deconvolution (See **Section 3.4.5.1, Step 2: Image Pre-processing**) A single z section was obtained for Hoechst-stained nuclei on the DAPI filter set. Two series of images (fields or locations) of each set of wavelengths were acquired in each well of two duplicate wells per condition. Thus, each treatment condition was represented by 4 to 8 fields per plate, leading to 12 to 72 fields overall acquired for each condition. Each plate is treated as an individual experiment, n=3-9 per condition.

3.4.5 Computational Analysis

3.4.5.1 Step 2: Image Pre-processing

Image stacks were opened in the GE INCell Developer Toolbox 1.9.1 program. Using the advanced track and block feature for plate mapping, the software was configured to visualize all z sections and wavelengths acquired at each time point (**Supplementary Figure 3** and **Supplementary Figure 4**), and the image histogram expanded from 12 bit to a 16 bit range (65,536 gray levels) to accommodate for deconvolution (written to process 16 bit images) and to accommodate for images previously registered using the RNiftyReg algorithm (also written to process 16-bit images; see **Section 3.4.6, Detection of Mitochondrial Membrane Potential (ΔΨm)** and **Section 9.4: parallelImageReg.R**). Next, the nearest-neighbor deblur (2D deconvolution) algorithm available in Developer Toolbox was applied to the seven z sections acquired of MTDR to simultaneously remove out of focus pixels and increase signal to noise of the in focus section, followed by flat field correction of the resulting

image. Next, image histogram data was normalized using the Information Equalization

transformation to achieve normalized intensity values from one field to another (**Figure

3-1b**). Normalized intensity values were critical to allow for exclusion of aberrantly

detected mitochondria and for inter-experiment comparisons (see text at **3.4.5.2, Step 3:

Segmentation** and **3.4.5.3, Step 4: Denoise-Free Aberrant Object Exclusion**). See

Figure 3-1b and **Figure 3-2a-b** for examples of preprocessed images.

3.4.5.2 Step 3: Segmentation

To locate mitochondria, the processed images were subjected to Developer

Toolbox's object-based segmentation based on local intensity variations (3 pixel kernel,

75% sensitivity). Bright objects (indicating high membrane potential) were detected

along with dimmer objects (lower membrane potential) as local changes in intensity (not

a global threshold) were used for detection. Nuclei were detected with Developer

Toolbox's nuclear segmentation algorithm (100% sensitivity, 1.90 sensitivity range, and

100 μm^2 minimum target area) in the Hoechst channel. The cellular cytoplasm was

estimated by extending the mitochondrial area in a process known as opening (dilating

objects outward until they touch/overlap followed by eroding the aggregated area).

Opening results in an efficient estimation of the cytoplasmic area based on location of

subcellular objects (mitochondria in this case) without the need for a specific cytosolic or

membrane stain [77]. To separate cells from one another, clump breaking was then

performed on the cytoplasm mask, using the nuclei image as a seed (1 cytoplasm = 1

nucleus). Example segmentation is shown in **Figure 3-1c**.

3.4.5.3 Step 4: Denoise-Free Aberrant Object Exclusion

Following detection of mitochondria during segmentation, the results (**Figure

3-1c**, a 1-bit image, or mask) were further processed to remove aberrantly detected

objects and improve the masks' representation of the experimental data. Post-processing quality control focused on excluding objects detected in background noise. Denoising algorithms can contribute artifacts to microscopic data, including undersegmentation [78]. Undersegmentation in this analysis is a particularly important problem as it can cause aggregation of multiple individual mitochondria, resulting in an inappropriate categorization of simpler phenotypes (puncta, rods) as more complex (networks). To ensure that mitochondria were maximally separated, a watershed clump breaking algorithm, which uses the presence of local intensity minima within an object, was applied to the mask to separate aggregates of adjacent individual objects. Finally, small objects (<0.35 µm^2) were excluded as any object represented by less than 3x3 pixels would violate the Nyquist limit of resolution (sampling frequency) [79]. To simultaneously avoid incorrect categorization of mitochondrial phenotypes and avoid aberrant object detection (mitochondrion-level quality control), measures were calculated on individual objects to exclude objects that were too dim or too small (see "Junk" category in **3.4.5.6, Step 7: Individual Mitochondrial Subtype Classification** and **Supplementary Figure 2**). These efforts reduced background detection of aberrant objects without increasing clumping/undersegmentation (data not shown). Following post-processing, the final mask was stored in cache and used for subsequent measures of cells and mitochondria in the same image.

3.4.5.4 Step 5: Target Linking

To compare mitochondrial morphological and intensity-based parameters across mitochondrial subtypes within individual cells and from cell to cell, from well to well and between experiments/treatment groups, a hierarchical target linking strategy was employed to assign smaller objects (mitochondria of each subtype, nuclei) to larger objects (cells). This was achieved using two levels of hierarchy by first assigning every

23

nucleus or mitochondrial subtype to a specific cytoplasm object (defining the combination of one nucleus and surrounding cytoplasm as a Cell) and then assigning individual mitochondrial subtype-cytoplasm linkages to each Cell. For a graphical representation of this concept, please see **Supplementary Figure 5**.

3.4.5.5 Step 6: Morphometric Measures Calculation

Measures of object morphology and intensity were calculated for every mitochondrion, and grouped on a per-morphological subtype basis for every cell. That is, one row of data describes the total or average value for mitochondria within an individual cell (e.g. Networked Total Area is the area (in μm^2) of the mask representing mitochondria classified as networked and assigned to an individual cell; Average Networked Fiber Length is the average fiber length of individual networked mitochondria within cells – in μm). These measures also included counts of mitochondria, area of mitochondria; and for complex shapes (networks), average length and fiber length. Fiber length is a variant of length that is derived by skeletonizing the mitochondrial network into its individual branches [73], followed by summation of the length of all branches. Length is simply the longest distance between two pixels in an object, and thus part of the complexity is lost in this measure alone. To enable correlation of the individual mitochondrial measures within a cell, results from all target linkages are assigned to cells by enabling the option "Display Measures in Primary Target Set" for each linkage in each target link's options in Developer Toolbox (see **Section 3.4.5.4, Step 5: Target Linking** and **Supplementary Figure 5**).

3.4.5.6 Step 7: Individual Mitochondrial Subtype Classification

The next step of the analysis is to classify mitochondria by morphological subtype to evaluate interconnectedness. In order to classify, an algorithm (decision tree)

was established using machine learning (see **Section 3.4.5.7 Step 7.1: Using Conditional Inference-based Machine Learning to Derive Mitochondrial Morphological Subtype Classification Scheme**). Four mitochondrial subtypes were defined, based on morphology and intensity measures (**Section 3.4.5.6, Step 7: Individual Mitochondrial Subtype Classification**) and previously published literature: puncta, rods, networks, and large & round [74, 80]. The morphological parameters displayed in **Supplementary Figure 2** define the decision tree. Each subtype was defined as a separate "target set" (independent object type), converting the decision tree into a series of complementary logic statements within Developer Toolbox's option for inclusion criteria in each target set. Exclusion of a fifth class, "junk", was useful in improving the classification scheme; this was made necessary by the use of denoise-free preprocessing which increases the segmentation algorithm's likelihood of finding objects comprised of small fluctuations in background intensity (see **3.4.5.3, Step 4: Denoise-Free Aberrant Object Exclusion**).

3.4.5.7 Step 7.1: Using Conditional Inference-based Machine Learning to Derive Mitochondrial Morphological Subtype Classification Scheme

To generate the classifier used in Section 3.4.5.6, Step 7: Individual Mitochondrial Subtype Classification, initial efforts used empirical methods to establish cutoff values for calculated morphometric measures (area, length, etc.) to bin mitochondria into the four categories using a decision tree of 5-7 nodes. However, low accuracy of this manually established tree and lack of generalizability amongst experiments encouraged use of computational methods to determine a more reliable decision tree classification scheme. Machine learning is a statistical and computational technique that may be used to derive a classification scheme from classified training data [76, 81, 82]. In this case, images were processed using the steps outlined in

Sections 3.4.5.1, 3.4.5.2, and 3.4.5.5, reporting instead all calculable measures on every individual mitochondrion (rather than aggregating on a per cell basis). Manual classification was performed on 1386 mitochondria within a variety of microscopic fields representing both cells treated with toxic compounds and compounds treated with vehicle. The ctree method from a published computational toolbox for conditional inference recursive partitioning (CRAN: *party*) was used in R version 3.0.1 (64 bit) to establish a classification scheme [76]. The algorithm grouped mitochondrial subtypes using 26 binary nodes that followed logic (networks had the longest length, puncta are small and have a form factor near 1, etc.). See **Supplementary Figure 2** to view the entire decision tree, **Figure 3-1d**, **Figure 3-2c-d** for examples of the classifier's performance overlaid on microscopic images and **Figure 3-1f** for mitochondrial shapes exemplary of the puncta, rod, network, and large & round subtypes.

3.4.5.8 Step 8: Supervised Analysis, Data Annotation

The result of the above analysis is a matrix, with each row representing an individual cell and each column a measure conducted on that particular cell. These data matrices were annotated to enable rapid interrogation of relevant measures and statistical calculations on a multilevel basis (groups of experiments, per-plate, per-treatment group, per-field, and per-cell). This is conceptually outlined in **Figure 3-1e**. Data between experimental replicates were aggregated into spreadsheets within Microsoft Excel 2010 (Microsoft, Seattle, WA), and replicate experiments tracked by inclusion of metadata columns that described each plate. Text-based metadata extraction formulae were also incorporated to group cells and fields by treatment group (minimum of 4 replicates per condition per plate). Data were aggregated into column format (each row now representing the average or total value of a particular measure per field per experiment) for import into GraphPad Prism 6.02 (GraphPad Software, La Jolla,

CA) using a PivotTable. Subsequent studies of membrane potential (**Section 3.4.6 -
Detection of Mitochondrial Membrane Potential (ΔΨm)**) used a new function
developed in R for fully automated data annotation (see **annotateData.R** in **Section 9.3,
Appendix B—Computer Programs**).

3.4.6   Detection of Mitochondrial Membrane Potential (ΔΨm)

In a second series of experiments, 62.5 nM TMRM (tetramethylrhodamine methyl
ester perchlorate, #T5428 Sigma-Aldrich, St. Louis, MO) was loaded into 661w cells
simultaneously with 50 nM MTDR and 10 µM Hoechst 33342 for 30 min. Cells were
washed with PBS, media changed to 90 µL DMEM with no phenol red (imaging buffer),
then incubated an additional 3 h prior to treatment to allow MTDR's free chloromethyl
group to react with free protein sulfhydryls (a covalent linkage). Treatments were
prepared at 10x final concentrations in imaging buffer, and 10 µL of each dosed to each
well of the imaging plate simultaneously using the VIAFLO 96 (Integra Biosciences,
Hudson, NH) multichannel liquid handling system (0.1 % [DMSO] final). The GE INCell
2000 Analyzer was configured to acquire the nuclear image in channel 1 (DAPI filter
set), the MTDR z series in channels 2-8 (Cy5 filter set), and the TMRM image in channel
9 (Cy3 filter set). Chromatic aberration in the optical setup led to lateral (XY)
misalignment of Cy3 images relative to DAPI and Cy5 images. To correct this aberration,
the misaligned TMRM images were registered after acquisition but prior to other
preprocessing steps (**Section 3.4.5.1, Step 2: Image Pre-processing**) using the
RNiftyReg package in R 3.0.1 64-bit, using the middle (in-focus) section of the MTDR
series as "target", and the TMRM image as "source" [83]. Pearson's correlation R values
were calculated using Coloc2 in FIJI (FIJI version 1.47d, http://fiji.sc). See
parallelImageReg.R in **Section 9, Appendix B—Computer Programs** for the code
used. Once registered, the images were analyzed as before in Developer Toolbox

(**Section 3.4.5**), including additional measures of average TMRM object intensity for nuclear, cytoplasmic, and individual mitochondrial subtypes. Following analysis, data was annotated using newly developed functions in R for interfacing with Developer Toolbox data output (annotateData.R in **Section 9.3, Appendix B—Computer Programs**) and subsetted by treatment group for analysis (**Figure 3-1e**). To correct for background signal, for each cell the average TMRM fluorescence intensity was determined within each mitochondrial subtype per cell followed by subtraction of the average TMRM fluorescence intensity within the nucleus for that cell (a region devoid of mitochondria) to correct for background TMRM fluorescence. Images displayed in **Figure 3-6a-c** were obtained by the multiply function in Image Calculator using FIJI, enabling the 32-bit (float) option and applying the "Fire" look-up table to the result to enhance the contrast of the polarization signal. The input images for multiplication were the mask derived from segmentation in Developer Toolbox (1-bit) and the registered and flat-field corrected TMRM image. The minimum and maximum settings in the Brightness and Contrast were adjusted to be equal amongst all images. **Supplementary Figure 1** was generated using similar techniques (equal contrast settings for each row) whilst leaving the look up table as grayscale and not applying the segmented mask via multiplication (i.e. a raw image). **Figure 3-6d** was generated by the 'density function in R's "stats" package, which is an implementation of kernel density estimation [84]. Density estimation bandwidth was set to defaults for each plot. The Kolmogorov-Smirnov test (ks.test function, CRAN: *stats* package) was used to make pairwise comparisons between treatment group populations (vehicle v. FCCP, vehicle v. oligomycin, FCCP v. oligomycin) (see **dPsi.R** in **Section 9.1, Appendix B—Computer Programs** for code used for generation of **Figure 3-6d**).

3.4.7   Seahorse XF96 Respirometry

661w photoreceptor cells were seeded (6,000 cells/well) into XF96 polystyrene plates (Seahorse Biosciences, Billerica, MA) and incubated for 48 h in DMEM-HG (Sigma-Aldrich) supplemented with 5% FCS. Lower seeding densities were used since XF96 plate well bottom area is significantly smaller (~60%) compared to standard 96 well plates. Following this growth period, media was changed for DMEM supplemented with 5.5 mM glucose and 1% FCS and vehicle or toxicant treatments administered for 24 h. Just prior to time of assay, media was switched to bicarbonate-ion free RS (reduced serum) buffer at pH 7.4 prepared with 130 mM NaCl, 5.33 mM KCl, 1.8 mM $CaCl_2$, 0.6 mM $MgCl_2$, 0.5 mM KH_2PO_4, 0.5 mM $NaPO_4 \cdot (H_2O)_7$, insulin, 5.5 mM glucose, and supplemented with 1% FCS, 1 mM L-alanyl-L-glutamine (GlutaMAX), 2 mM glutamine, 1% MEM Vitamins, 1% MEM Amino Acids, 1% MEM Non-Essential Amino Acids, 1% Penicillin/Streptomycin. All inorganic salts used were obtained from Sigma-Aldrich (St. Louis, MO) and organic supplements obtained from GIBCO/Life Technologies (Grand Island, NY) unless otherwise noted. After recording 3 baseline oxygen consumption rate (OCR) measurements, the response of cells to 1 µM FCCP (carbonyl cyanide-p-trifluoromethoxyphenylhydrazone) was measured. This assay (maximal respiratory capacity) is frequently used as a mitochondrial stress test [85]. Uncoupled OCR's for each condition were recorded and reported as mean +/- standard error of the mean (s.e.m.) across experiments.

3.4.8 Statistical Analysis

Unless otherwise specified, graphing and statistical analyses were performed in GraphPad Prism 6.02 (GraphPad Software, La Jolla, CA). Tests for significance amongst groups were conducted via the non-parametric Kruskal-Wallis test and post-hoc pairwise tests (Dunn's correction for multiple tests) based on normality of underlying data as determined using D'Agostino-Pearson omnibus normality test. Outlying fields (low seeding density, bacterial contamination, poor staining, etc.) were excluded using the R_{out} algorithm (Q = 10%) on every experimental replicate (microscopic field) within each treatment group. The mean value for each parameter (without outliers) was then calculated per experiment. Data shown are mean ± s.e.m. amongst replicate experiments. Multiplicity-adjusted P values were determined; p < 0.05 compared with vehicle denoted with an asterisk. Power analysis was not performed to determine sample sizes in mitochondrial morphological studies (**Figure 3-1** through **Figure 3-5**) as these studies represented the first quantification of mitochondrial subtype areas and the authors had no expectations of standard deviation or expected effect size. For the membrane potentiometric studies, it was defined that a difference of 20% would be of biological interest and the coefficient of variance from all mitochondria area (5.1%) was used to calculate power. The result of this analysis was that n=3 experiments should be the minimum number of replicates needed to achieve 80% power in a one-way ANOVA with three groups and α = 0.05. Russ Lenth's web-based power analysis software was used for this calculation [86].

3.5 Results

3.5.1 Overview of Results

The performance of the classifier is presented in **Section 3.5.2** followed by analysis of the mitochondrial morphological response to known mitochondrial toxicants in **Section 3.5.3**. This is then followed by the analysis of mitochondrial membrane potential in **Section 0**. In the morphological analysis (**Section 3.5.3**), seven measurements are reported: total mitochondrial area (comprised of all phenotypes, representative of total mitochondrial mass), puncta area, rod area, networked area, large and round area, total mitochondrial count, and the average fiber length (length along all branches) of networked mitochondria. To correlate these morphological findings with the effects of toxicants on mitochondrial electron transport chain function, respirometry was conducted in parallel experiments (Method described in **Section 3.4.7**). All treatments were for 24 h unless otherwise noted.

3.5.2 Performance of Mitochondrial Subtype Classifier

In order to enable automated classification of mitochondria, the computational technique of machine learning was employed to establish an optimized classification scheme. Briefly, 1386 mitochondria were manually classified into the four bins (networked, rod-like, punctate, and large & round, followed by separation of these mitochondria into a test set of 489 and a training set of 897. The training set was then used as input to a published computational toolbox for conditional inference recursive partitioning to train a decision tree [76]. **Supplementary Figure 2** describes the measures and breakpoints along those measures that the machine learning algorithm determined most effective in partitioning categories (details in **Section 3.4.5.7**).

To evaluate the performance of the decision tree, several confusion matrices (tables of predicted categories versus manually determined categories) were generated as well as κ statistics to evaluate agreement. The predictions within the training set **(Supplementary Table 1a)** were accurate and errors were somewhat predictable – that is, confusion was highest amongst similar shapes. Excluding misclassification as junk, rods were most often misclassified as networks (23/29 misclassifications) and vice versa (5/6 misclassifications), large and round were most often confused with puncta (6/12 misclassifications) and vice versa (13/14 misclassifications). The accuracies within the consensus test set **(Supplementary Table 1b)** followed the same trends as those in the training set with the following exceptions. Excluding misclassification as junk, rods were most often misclassified as puncta rather than networks (18/26 misclassifications), and large and round mitochondria were tied for confusion with puncta or rods (2/4 misclassifications each). Taken together, performance degraded marginally as expected in moving to a set of mitochondria "never seen" by the classifier (as measured by κ of 0.710 for training set and 0.644 for test set). The small difference between these κ's indicates a tolerable degree of optimism regarding the classifier's generalizability to data naïve to the classifier, quantified as decreases in accuracy in test set as compared to training set [87, 88].

Before reaching consensus, the authors were blinded from one another in their classification of the same 489 mitochondria in **Supplementary Table 1b** (test set) to further characterize the original classification tree and quantify its optimism, as the disagreement between authors can serve as a benchmark for error. Although degradation was observed in comparing the classifier (developed using author AL's training data) against author RC's classifications of the same test data (κ=0.557), (**Supplementary Table 2b**), this amount of decreased agreement was consistent given

the level of disagreement of authors AL and RC: κ=0.641 (**Supplementary Table 2b**).

To provide insight into the generalizability of this classifier, authors AL and RC together

decided on a consensus classification for the full test set: κ=0.601, (**Supplementary**

Table 1b), which is similar to the levels of agreement between the classifier and the

blinded author AL's κ=0.644 **(Supplementary Table 2a)** and classifier v. blinded author

RC's κ=0.577, **(Supplementary Table 2c)**, indicating that the classifier is not

significantly biased to a single individual.

To test whether or not the classifier performs better on easy to classify

(unambiguous) mitochondria, its levels of agreement with two conditions of the test set

were evaluated: 1) when author AL and RC agreed (likely unambiguous) and 2) when

author AL and RC disagreed (likely ambiguous). The classifier demonstrated increased

performance when compared against a subset of the test mitochondria that both authors

blindly agreed upon (κ=0.731, **Supplementary Table 2d**), and decreased performance

when analyzing mitochondria that the authors blindly disagreed upon (κ=0.258,

Supplementary Table 2e), supporting the hypothesis that the classifier's accuracy – just

like that of a human classifier – was better when morphology is unambiguous.

Using this classifier, 95% of aberrantly detected objects (junk) were excluded.

Within the four mitochondrial classes (networks, rods, puncta, and large & round),

accuracies were 95%, 77%, 95%, and 64%, respectively, as judged by agreement with a

test set of 489 consecutively detected mitochondria classified via consensus between

authors AL and RC (**Supplementary Table 1b**). These accuracies correspond with a

kappa statistic (κ) of 0.601, indicating the algorithm agreed well with two human

classifiers (see **Section 3.4.5.7** and **Supplementary Table 1**).

3.5.3 Known Mitochondrial Toxicants Produce Divergent Effects on Individual Mitochondrial Morphological Phenotypes
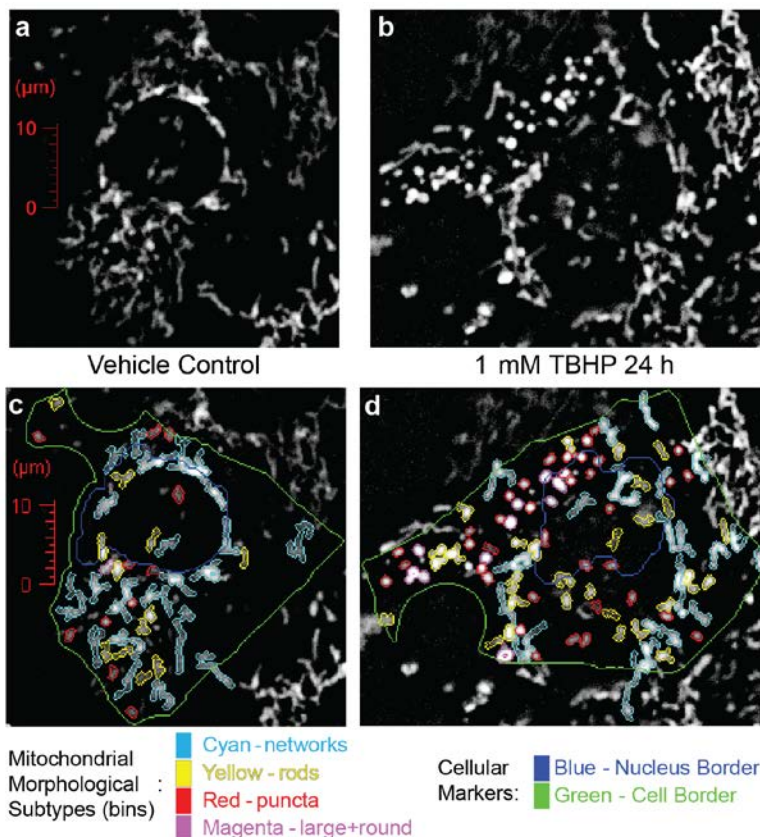
Figure 3-2 Representative images of t-butyl hydroperoxide (TBHP)-induced damage to mitochondria. 661w cells were exposed to 1 mM TBHP (**b**, **d**) or vehicle (**a**, **c**) for 24 h and analyzed using the described morphometric analysis. Pre-processed images of living mitochondria stained with MitoTracker Deep Red (MTDR) (**a**, **b**). Classification results overlaid (**c**, **d**). Nuclear borders were identified from Hoechst staining, and cell borders were defined via "opening" the preprocessed and segmented MTDR image. A cell is defined as an object containing a nucleus and composed of surrounding mitochondria.

3.5.3.1 Oxidative stress – t-butyl hydroperoxide (TBHP)

The model oxidant tert-butyl hydroperoxide (TBHP) causes oxidative stress and mitochondrial damage [89-91]. At 24 h, this functional damage is readily visualized as a loss of filamentous networked mitochondria and induction of swelling (**Figure 3-2**). Respirometry demonstrated an 80% decrease in respiratory capacity at TBHP concentrations of 500 µM and higher, confirming mitochondrial dysfunction (**Figure 3-3a**). At 500 µM, a 25% decrease in total mitochondrial area (**Figure 3-3b**) and a 25% increase in the large & round phenotype were observed (**Figure 3-3g**). At 1 mM, twice as many changes were noted, including a 40% decrease in overall mitochondria counts

and rod area (**Figure 3-3c, e**), a 50% decrease in area of networked mitochondria

(**Figure 3-3f**), and a 10% decrease in networked fiber length (**Figure 3-3h**). Interestingly,

no changes in puncta area were observed at any concentration (**Figure 3-3d**).
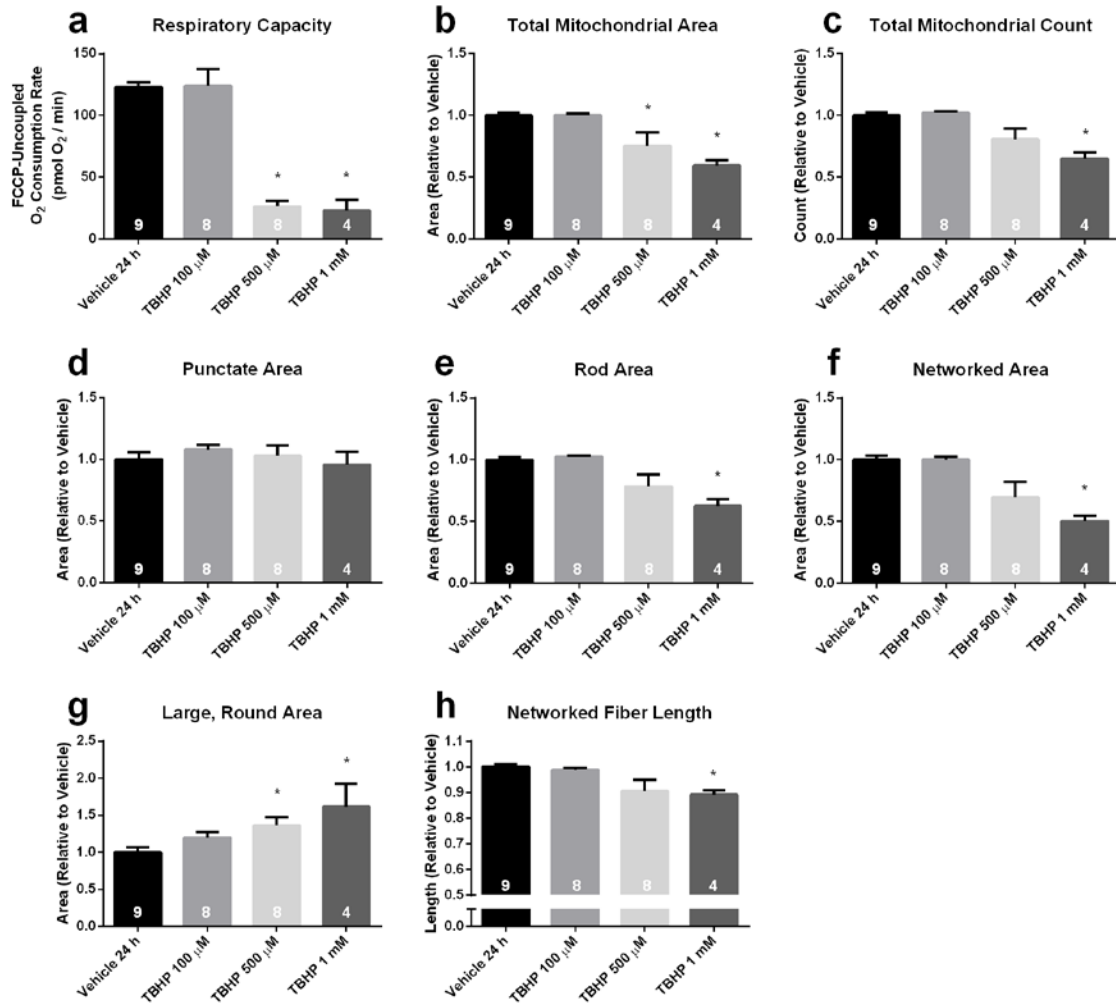
Figure 3-3. Quantitative assessment of oxidant-induced mitochondrial damage.

Carbonyl cyanide-p-trifluoromethoxyphenylhydrazone (FCCP)-uncoupled respiratory capacity, which measures mitochondrial electron transport chain function, was measured via Seahorse XF96 respirometry following 24 h treatment with t-butyl hydroperoxide (TBHP) at the concentrations indicated (a). Results of the corresponding mitochondrial morphological assessment (b-h). n=4-9 experiments (numbers on each bar), representing 30k-300k mitochondria per condition, bars s.e.m. Data analyzed by Kruskal-Wallis test followed by Dunn's post test, all groups versus vehicle only. *multiplicity-adjusted p<0.05 versus vehicle.

3.5.3.2 Mitochondrial Electron Transport Chain Inhibition

Following the studies of general oxidative stress, mitochondrial morphological

remodeling in response to 24 h incubation with toxicants specific to a single

35

mitochondrial target was measured. Rotenone and antimycin A inhibit electron transport chain complexes (ETC) I and III, respectively [92, 93]. Oligomycin inhibits the F_o subunit of ETC complex V, blocking oxygen consumption linked to ATP phosphorylation [94].
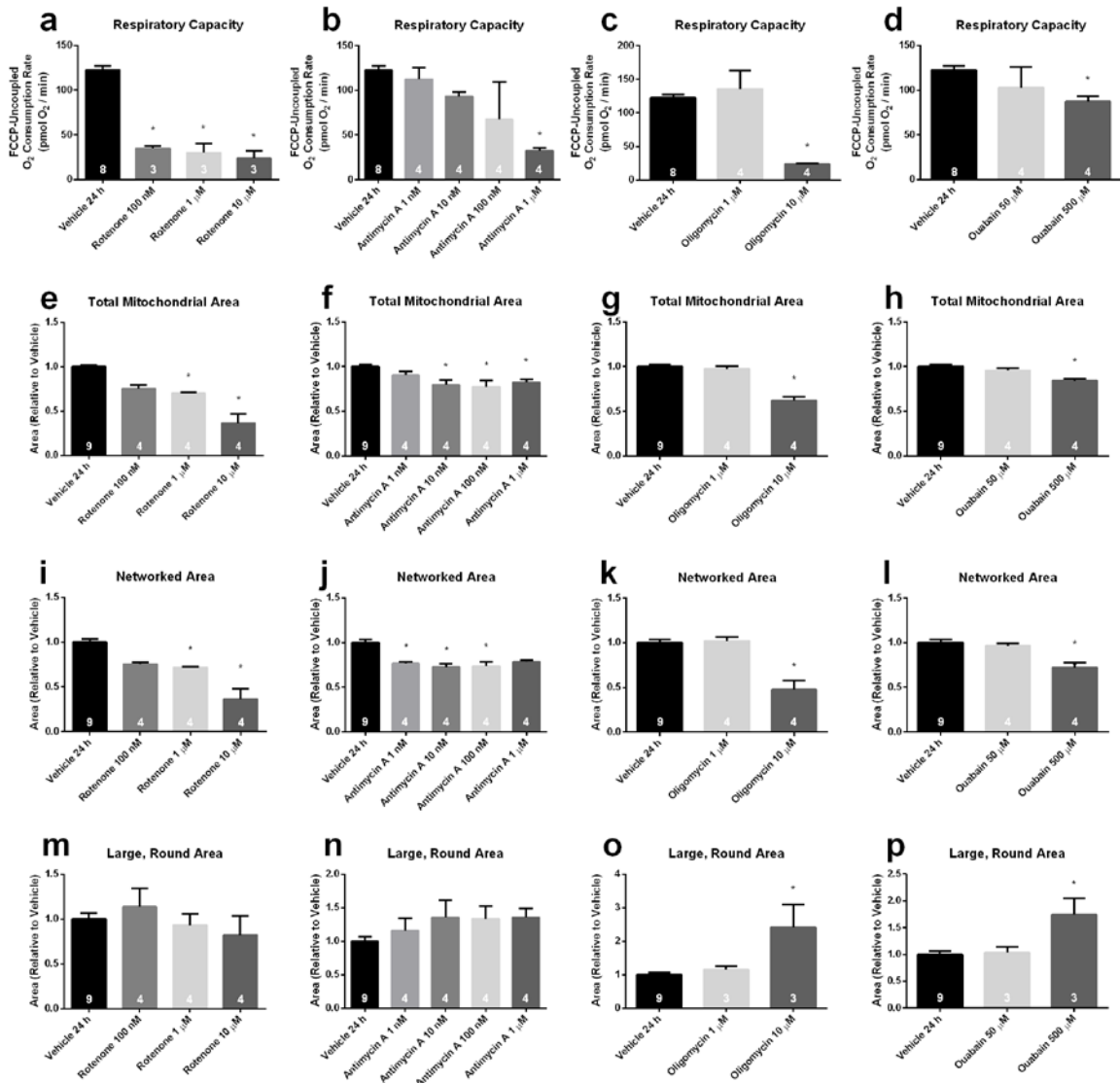
Figure 3-4. Quantitation of changes in morphology elicited by mitochondrial toxicants.

Carbonyl cyanide-p-trifluoromethoxyphenylhydrazone (FCCP)-uncoupled respiratory capacity which measures mitochondrial electron transport chain function, was measured via Seahorse XF96 respirometry following 24 h treatment with toxicant at the concentrations indicated (a-d). Results of the corresponding mitochondrial morphological assessment are shown in Panels e-p. n=3-9 experiments (numbers on each bar), bars s.e.m. Data analyzed by Kruskal-Wallis followed by Dunn's post test, all groups versus vehicle only. *multiplicity-adjusted $p < 0.05$ versus vehicle. Additional measures for each toxicant are quantified in **Supplementary Figs. 6-9**).

Rotenone decreased mitochondrial respiratory capacity by 60% at 100 nM

(**Figure 3-4a**). While no morphological changes were statistically significant at this low

concentration, increasing the dose to 1 µM elicited a 33% decrease in mitochondrial total area (**Figure 3-4e**), count, and areas of rods and networks (**Figure 3-4i**). Increasing the concentration to 10 µM further decreased the aforementioned measures and decreased puncta area by 60%. At no concentration of rotenone were changes noted in either the large & round subtype (**Figure 3-4m**) or of the average fiber length of networks (**Supplementary Figure 6**).

Antimycin A decreased respiratory capacity at 1 µM (80%, **Figure 3-4b**). However, morphological remodeling was observed at lower concentrations. At 1 nM, antimycin A caused a 20% decrease in networks (**Figure 3-4j**), which at higher concentrations was accompanied by 20% decreases in total mitochondrial area (**Figure 3-4f**). None of the other measures were altered at 1 nM or 10 nM (**Supplementary Figure 7**).

Oligomycin decreased respiratory capacity by 85% at 10 µM (**Figure 3-4c**). At this concentration, overall mitochondrial area and count decreased 40 and 25%, respectively, indicating an overall loss of mitochondrial mass (**Figure 3-4g**). Oligomycin also induced decreases in rods and networked areas (**Figure 3-4k**), and the length of networks (30%, 55%, and 15%, respectively), while the large & round population increased 130% (**Figure 3-4o**). No decreases in puncta area were observed with oligomycin treatment (**Supplementary Figure 8**).

3.5.3.3 Na$^+$/K$^+$ ATPase Inhibition at the Plasma Membrane

Ouabain is an inhibitor of the plasma membrane Na$^+$/K$^+$ ATPase, which results in the influx of Na$^+$ and water into the cell, leading to cell and mitochondrial swelling [95]. At 500 µM ouabain, mitochondrial respiratory capacity decreased 30% (**Figure 3-4d**). Total mitochondrial area decreased 20%, comprised mainly of decreases in the networked population (25%, **Figure 3-4h, l**). As expected, since ouabain increases

37

water content, a 75% increase was detected in the large & round subtype (**Figure 3-4p**).

The fiber length of networks also decreased 10% (**Supplementary Figure 9**). No

significant changes were observed in other measures.

3.5.3.4 Relative Abundance of Mitochondrial Phenotypes

One motivation for looking at subtypes individually is that there is an unequal

abundance of mitochondrial phenotypes. Mitochondria in 661w cells treated with vehicle

are comprised of 61%, 28%, 9%, and 2% of networks, rods, puncta, and large & round,

respectively (**Figure 3-5, Supplementary Table 3, Supplementary Table 4**). Treatment

with oligomycin increased the proportion of large & round mitochondria to 5% (**Figure

3-5c**). Treatment with TBHP shifted all proportions, with a 15% loss in networks and

increases in rod, puncta and large & round mitochondria by 6%, 7%, and 2%,

respectively (**Figure 3-5e**). Treatment with antimycin A, ouabain, or rotenone induced no

significant shifts in proportions (**Figure 3-5b, d,** and **f**).
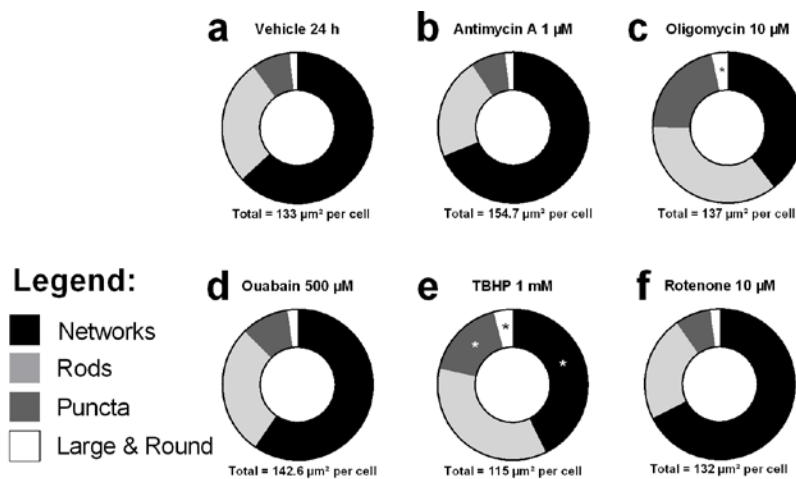
Figure 3-5. Relative abundance of mitochondrial phenotype proportions per cell.

Vehicle control (**a**), antimycin A (**b**) oligomycin (**c**), ouabain (**d**), t-butyl hydroperoxide (**e**), and rotenone (**f**). The size of each shaded area within each panel represents the proportion of each individual phenotype's average area of the total mitochondrial area. Data analyzed by Kruskal-Wallis followed by Dunn's post test, all groups versus vehicle only. *multiplicity-adjusted p<0.05 versus vehicle (proportion of subtype in treatment group versus proportion of same subtype in vehicle control). See **Supplemental Tables 3 and 4** for numerical representations of these data.

3.5.4 Quantification of Mitochondrial Membrane Potential ($\Delta\Psi_m$)

Many studies have used the positively charged dye TMRM to measure $\Delta\Psi_m$, yet none have analyzed its intensity amongst different morphological classes or developed an automated process for separating intramitochondrial fluorescence from other cellular compartments [75, 96-99]. MTDR, previously used in this study to label all cellular mitochondria, is well-retained in depolarized mitochondria (**Supplementary Figure 1**). Thus, this dye was used to reliably locate all mitochondria followed by analysis of TMRM intensity within the MTDR-derived mitochondria-specific mask. The colocalization of these two dyes was nearly identical in control cells as assessed by values of Pearson's correlation > 0.90 following registration (**Section 3.4.5.1**). For imaging, cells were loaded with TMRM and MTDR for 30 min (followed by a wash step and 3 h of incubation with no treatment), incubated for one hour with vehicle, the uncoupler FCCP, or oligomycin, and then imaged. Mitochondria were localized and classified using MTDR images only, and the mean fluorescence intensity of TMRM within each mitochondrion was calculated and averaged per subtype (**Figure 3-6**). Compared to control conditions (**Figure 3-6a**), uncoupling mitochondria with 1 µM FCCP induced depolarization as evidenced by a 90% decrease in mitochondrial TMRM fluorescence intensity in each cell (**Figure 3-6b, d**). Oligomycin (10 Fold) increase in rpolarization as evi mitochondrial TMRM fluorescence intensity compared to vehicle (**Figure 3-6c, d**). FCCP and oligomycin affected mitochondrial membrane potential in all mitochondrial subtypes, although surprisingly, the large and round population was more resistant to FCCP-induced depolarization in comparison to total mitochondria or networks (**Supplementary Figure 10**).
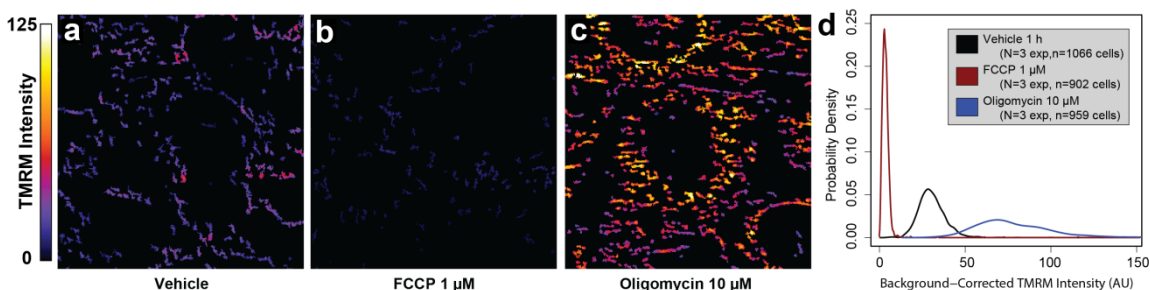
Figure 3-6. Quantification of mitochondrial membrane potential (ΔΨ$_m$) via mitochondria-specific labeling.

Representative images displaying intensity of tetramethylrhodamine methyl ester (TMRM) staining within mitochondria located using MitoTracker Deep Red (**a-c**). Mean intensity of TMRM located within all mitochondria in each cell was calculated and the distribution shown using a density plot (higher TMRM intensity to the right) (**d**). Treatments were as indicated above each panel and were conducted for 1 h for n=3 independent experiments. Distributions in (**d**) were compared using a two-way Kolmogorov-Smirnov test and were adjusted for multiple comparisons; all pairwise combinations returned p<0.05, indicating significant induction of polarization or depolarization. See **Supplementary Fig. 10** for a summary of polarization responses of each morphological bin (puncta, rods, networks, large & round) and **Supplementary Fig. 1** to see individual MitoTracker Deep Red and TMRM staining responses to treatment.

3.6 Discussion

This study reports the development of a high-throughput method for the analysis of mitochondrial dynamics and function via automated fluorescence microscopy and a new software algorithm, and evaluates the response of mitochondrial morphology to known chemical inhibitors of mitochondrial function in 661w photoreceptor cells. Depending on the target and the concentration of these toxicants, qualitatively and quantitatively different effects on mitochondrial morphology were observed, demonstrating concentration-dependent mitochondrial morphological changes for the first time. Using conditional inference-based machine learning, mitochondria were classified into four distinct bins according to their shape (puncta, rod, network, large & round). This classification was crucial to enabling the quantification of toxicant-induced changes in low abundance subtypes (large & round, 2% of mitochondria by area), and also improved the quantification of more common shapes (networks, rods, and puncta are 61%, 21% and 9%, of cellular mitochondria by area, respectively). By segregating subtypes and thus measurements, this strategy improved sensitivity and statistical power to detect toxicant-induced differences. For instance, fiber length of networks had

a much lower coefficient of variation (3%) than all the other measures, which ranged from 6-20% in control cells (derived from measures presented in **Figure 3-3, Figure 3-4,** and **Figure 3-5**). Regarding the reproducibility of previous studies, Koopman et al. described the utility of measures such as Form Factor, Area, and Perimeter for describing interconnectedness [75] and as expected, these measures were utilized in the machine learning-derived classifier (**Supplementary Figure 2**).

One example of this increased sensitivity is apparent in the quantification of concentration-dependent changes in the rare population of large & round mitochondria, which may serve as the first useful indicator of mitochondrial swelling in live cells. For instance, TBHP, oligomycin, and ouabain increased the prevalence of large & round mitochondria by 40-130%, whereas rotenone and antimycin A had no effect. Oxidant TBHP is a known activator of permeability transition pore opening and Ca^{2+}-induced mitochondrial swelling [90, 91, 98]. Ouabain treatment is expected to induce mitochondrial swelling via cellular osmotic dysregulation [100, 101]. These data support that swollen mitochondria form a significant portion of the large and round population. However, two punctuate mitochondria undergoing fusion may exist in a large & round shape temporarily (or vice versa); a rod-puncta intermediate [62]. Since swollen and rod-puncta intermediate phenotypes have a similar appearance, they are not separable by morphological classification alone. TMRM signal intensity of the large and round mitochondrial subpopulation in cells treated with control or other treatments resembles a Gaussian distribution (and not bimodal), indicating mitochondrial polarization does not dichotomize this population. In addition to swelling, exposure to TBHP recapitulated previously published findings including mitochondrial fragmentation [102] (fewer rods and networks, decreased fiber length) and increased mitochondrial turnover/mitophagy [103] (indirectly inferred from decreased total area).Additional studies, including

simultaneous fluorometric measurement of intramitochondrial calcium $[Ca^{2+}]_m$ (expected to rise during swelling [96, 104]), might be helpful in defining or subdividing this population in the future. Recent studies into mitochondrial superoxide "flashes" have highlighted the importance of the mitochondrial permeability transition pore in conducting a transient outward (mitochondria to cytoplasm) Ca^{2+} current through VDAC [105]. In conjunction with respirometry, it will be interesting to use this method to understand the role of mitochondrial morphology as either a determinant or result of superoxide flash frequency.

It would appear that the networked phenotype was the most sensitive to stress, as decreases in both total mitochondrial area and networked area (and in many cases, length of networks) were observed with all mitochondrial toxicants tested. Yet, neither complex I inhibition by rotenone nor complex III inhibition via antimycin A resulted in decreased networked fiber length or increased large & round. These data support the idea that mitochondria display a complex response to damage, and fission of networks into simpler phenotypes is a common feature.

Although the conditional inference decision tree classifier used here to bin mitochondria was capable of quantifying concentration-responsive changes in mitochondrial morphology, a further improvement would be the ability to implement more robust machine learning algorithms to improve accuracy. Future efforts to implement this analysis in an open source platform that supports three spatial dimensions (requiring perhaps 1-2 orders of magnitude more computing power) and advanced machine learning implementations to further improve accuracy would be of great benefit to the research community.

Automation facilitated by use of an off-the shelf microscope and analysis tools provides the throughput necessary for the technique to be useful as a discovery or

diagnostic tool. Compound libraries could be screened for their potential to improve or damage mitochondrial function. Many failures of therapeutics have been attributed to mitochondrial toxicity; early discovery of such liabilities may improve both patient safety and financial success. Through RNAi screening, genetic determinants of MD could be identified. Indeed, image-based RNAi screens have proven their utility in determining genes involved in induction of autophagy and parkin-directed mitophagy in cells [106, 107]. By analyzing colocalization of mitochondrial subtypes with phagosomes/lysosomes, this method could segregate general autophagy and selective mitophagy [108]. Current diagnosis of mitochondrial diseases uses genetic, biochemical and functional analyses, yet none of these methods directly test the regulation of MD [109, 110]. For example, mutations in outer membrane fusion GTPase mitofusin 2 (Mfn2) result in the 2A subtype of peripheral neuropathy Charcot-Marie-Tooth Disease (CMT2A) [111]. While manual analysis of fibroblast mitochondrial morphology from CMT2A patients and controls found no difference between the two [112], computational methods were able to detect pro-fission and pro-fusion changes in mouse fibroblasts with genetic complex I defects [113]. The binning-based computational morphometric method presented here may detect smaller, though very significant to phenotype, differences by enabling subtype-specific analysis of mitochondrial morphology in many replicates. Finally, the morphological binning classifier scheme presented here may be applied to any fluorescently labeled intracellular organelle/target with morphology ranging from filamentous to punctate, or to quantify the localization of uncharacterized proteins to morphological subtypes of organelles in an unbiased fashion.

3.7 Conclusion

A high-content microscopic method for the automated classification of mitochondrial morphology and membrane potential is presented using an automated fluorescence microscope platform (GE INCell Analyzer 2000) and new software built on the R platform. Classification of mitochondria into four shape bins (punctate, rod, networked, and large & round) allowed for the quantification of concentration-responsive mitochondrial swelling, dynamics, and membrane potential in response to a number of mitochondrial toxicants. To our knowledge, this is the first method to discriminate between mitochondrial subtypes and to determine their individual membrane potentials with sufficient throughput for pharmacological or toxicological evaluation to further discovery and diagnostics.

4. Chapter 2—IBMX Administration Results in Mitochondrial Membrane Hyperpolarization, Increased Network Morphology, and Decreased Uncoupled Respiration

4.1 Abstract

IBMX is commonly used as a nonselective inhibitor of cyclic nucleotide phosphodiesterases and adenosine receptors. Previous results have indicated that IBMX administration to retina-derived photoreceptor cell line 661w results in decreased mitochondrial respiration at 24 h followed by decreased cellular viability at 48 h. As this sequence of mitochondrial dysfunction followed by cytotoxicity is also observed in inherited retina degeneration, our lab has used IBMX administration to 661w as a cell-based model of photoreceptor degeneration. However, the early stage events that lead to decreased mitochondrial respiration are not fully understood. Using a novel high content microscopic method for determining mitochondrial membrane potential and interconnectedness, these studies demonstrate concentration- and time-dependent changes in mitochondrial physiology occur following IBMX administration. As early as 1 h, an increase in interconnected morphology is observed (108-120% of control), followed by subsequent increases in mitochondrial membrane potential at 4 h (150-200% of control). Both of these changes are sustained for 24 h, at which time decreases in uncoupled respiration are observed (70-80% of controls). Pharmacological inhibition of GSK-3β reversed IBMX-induced increases in membrane potential and networked morphology. Taken together, these results suggest resistance of the mitochondrial inner

membrane to proton influx increases following IBMX administration, which may be in part due to increased GSK-3β activity and/or decreased opening of the mitochondrial permeability transition pore.

4.2 Introduction

3-isobutyl 1-methylxanthine (IBMX) is a xanthine derivative structurally similar to adenine, caffeine, and theophylline (**Figure 4-1**). IBMX has been characterized to inhibit cyclic nucleotide phosphodiesterases PDE1-PDE7 and adenosine receptors. As many of these targets have been reported to couple to downstream regulators of mitochondrial morphology and function (e.g. increased cAMP activates PKA, reported to phosphorylate Drp1 [60]), it was hypothesized that modulation of one or more of these targets may result in altered mitochondrial physiology.

The following studies will characterize the effects of IBMX on mitochondrial morphology and function using Seahorse XF96 respirometry in combination with a novel high content microscopic method developed in our lab [114] and described in detail in **Section 3, Chapter 1— Quantitative Analysis of Mitochondrial Morphology and Membrane Potential in Living Cells Using High Content Imaging, Machine Learning, and Morphological Binning**.

Figure 4-1. Structure of 3-isobutyl 1-methylxanthine (IBMX).

As mutations in PDE6 result in retina degeneration in mice and humans, our lab has utilized IBMX treatment of photoreceptor-derived cell line 661w to mimic this loss of PDE function [3, 4, 115]. Briefly, in this model, following IBMX administration, recapitulation of the phenotype observed in multiple retina degenerative mouse models [15] is observed, namely, an induction of mitochondrial dysfunction that precedes cell

death. For a more extensive review of 661w cells, PDE biology, and adenosine receptor signaling, please see **Section 2, Review of Literature**.

4.3 Materials and Methods

4.3.1 High Content Determination of Mitochondrial Morphology and Membrane Potential

To evaluate the concentration- and time-dependency of IBMX-induced mitochondrial changes, the method of Leonard et al. [114] was used. Briefly, 661w cells were seeded into Nunc Edge 96-well plates (Fisher) at a density of 8900/well and incubated in DMEM-HG (Invitrogen) for 24 h. Media was changed to DMEM supplemented with 1% fetal calf serum (FCS, Atlanta Biologicals) and incubated overnight before staining. 661w cells were loaded with 50 nM MitoTracker Deep Red, and 10 µM Hoechst 33342 for 30 min and then washed followed by a 3 h incubation at 37 °C in DMEM-HG supplemented with 1% FCS. After 3 h, cells were treated with IBMX at the indicated concentrations and cells imaged. Imaging was performed on a GE INCell Analyzer 2000 automated wide-field fluorescence microscope using a 40x Nikon ELWD objective (NA 0.6) matched with the large-format 2048x2048 pixel 12-bit Coolsnap K4 camera. Images were saved in the TIFF image file format and subjected to the high content mitochondrial morphological analysis as described in **Section 3, Chapter 1**.

4.3.2 Seahorse XF96 Respirometry

661w photoreceptor cells were seeded (6,000 cells/well) into XF96 polystyrene plates (Seahorse Biosciences, Billerica, MA) and incubated for 48 h in DMEM-HG (Sigma-Aldrich) supplemented with 5% FCS. Media was then changed for DMEM supplemented with 5.5 mM glucose and 1% FCS and vehicle or toxicant treatments

administered for 24 h. Just prior to time of assay, media was switched to bicarbonate-ion free RS (reduced serum) buffer at pH 7.4 prepared with 130 mM NaCl, 5.33 mM KCl, 1.8 mM $CaCl_2$, 0.6 mM $MgCl_2$, 0.5 mM KH_2PO_4, 0.5 mM $NaPO_4 \cdot (H_2O)_7$, insulin, 5.5 mM glucose, and supplemented with 1% FCS, 1 mM L-alanyl-L-glutamine (GlutaMAX), 2 mM glutamine, 1% MEM Vitamins, 1% MEM Amino Acids, 1% MEM Non-Essential Amino Acids, 1% Penicillin/Streptomycin. All inorganic salts used were obtained from Sigma-Aldrich (St. Louis, MO) and organic supplements obtained from GIBCO/Life Technologies (Grand Island, NY) unless otherwise noted. All oxygen consumption rate (OCR) measurements used cycle times of 4 minutes per mix (probes moving) and 3 minutes per measure (probes down). After recording 3 baseline OCR measurements, oligomycin (100 nM) was administered and 3 additional OCR measurements obtained. This was followed by administration of FCCP (carbonyl cyanide-p-trifluoromethoxyphenylhydrazone) (1 µM) and two OCR measurements obtained. Finally, a combination of rotenone (5 µM) and antimycin A (100 nM) was administered and two final OCR measurements obtained. Uncoupled OCR's for each condition were recorded and reported as mean +/- standard error of the mean (s.e.m.) across experiments. As the sequence of mitochondrial perturbing agents above includes non-reversible pharmacology, each time point was performed on separate plates.

4.3.3 Cytotoxicity Determination via Propidium Dye Exclusion

For cytotoxicity experiments, 661w cells were seeded at a density of 6,000 cells/well in DMEM-HG supplemented with 5% FCS. 24 h later, this media was withdrawn and changed to DMEM-HG supplemented with 1% FCS. 48 h following seeding, treatments were administered in DMEM-HG supplemented with 1% FCS (final [DMSO] = 0.1%). Cells were incubated with these treatments for 48 h before imaging on the GE INCell Analyzer 2000. Prior to imaging, conditioned media contained treatments

was withdrawn and set aside. Cells were stained for 30 min with 10 µM Hoechst 33342 and 1.5 µg/mL propidium iodide (Sigma). Following staining, cells were washed one time, and then conditioned media was returned to cells and cells incubated at 37 °C until imaged (10-45 minutes). Images were captured using the DAPI filter set for Hoechst and the Cy3 filter set for propidium iodide, with a Nikon 10x ELWD objective, and saved in the TIFF format. Images were analyzed in Developer Toolbox, with Object segmentation used to identify all nuclei in the DAPI-filtered images and a second Object segmentation used to identify PI-stained nuclei in the Cy3-filtered images. The measure of % PI-Positive Cells was obtained by dividing the PI-positive nuclei count by the total nuclei count and then multiplying by 100.

4.3.4 Genome-wide Microarray Expression Profiling

mRNA was isolated from 661w cells grown to confluence in 10 cm dishes and purified using the RNeasy RNA purification kit (Qiagen, Valencia, CA). cDNA was synthesized from high-quality RNA ($A_{260/280} \geq 1.80$) and subjected to microarray analysis using conditions identical to those described previously [116]. Briefly, GeneChip Mouse Genome 430 2.0 oligonucleotide arrays (Affymetrix) were hybridized with equal amounts of labeled cRNA (15 µg/array) and readout were performed by the DNA Microarray Core Facility at the Medical University of South Carolina using the Affymetrix Fluidics Station.

4.3.5 Statistical Analysis

Statistical analysis was conducted using either one-way ANOVA or two-way ANVOA, respectively, for single time-point (>2 concentrations/treatments) or multiple time-point and multiple concentration experiments. Holm-Sidak multiplicity-adjusted post-hoc analyses were conducted in each analysis to compare across treatment groups (not timepoints).

4.4 Results

As previous results indicated that IBMX induces pathophysiological changes (increased ROS, calpain activation) in a timeframe shorter than 24 h [3, 115], the time course of mitochondrial physiological changes was first evaluated. Interestingly, it was observed that concentrations of IBMX ranging from 10 nM to 1 mM failed to induce significant decreases in mitochondrial respiratory capacity at early time points (1, 4, and 12 h) when compared to vehicle control (data not shown). As previously demonstrated, a 20-30% decrease in respiratory capacity at 10-500 µM concentrations at 24 h was observed, followed by increased cell death (200-400% of control) at 48 h (**Figure 4-2**).
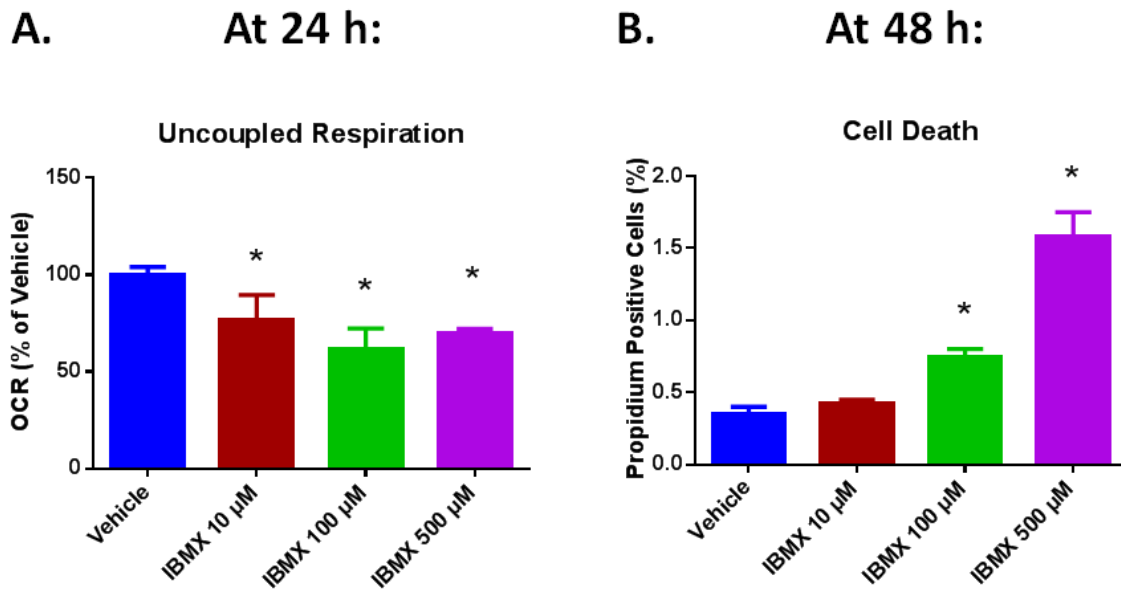
Figure 4-2. IBMX Induces Decreased Mitochondrial Uncoupled Respiration and Cellular Viability.

Data are mean ± s.e.m. of n=3-11. Results of XF96 respirometry following 24 h incubation with IBMX at the indicated concentrations (A). Rates corrected for non-mitochondrial respiration (following rotenone and antimycin A administration). 661w cells were treated for 48 h at the indicated concentrations of IBMX or vehicle (0.1 % DMSO), then stained with Hoechst 33342 and propidium iodide (PI), imaged using the INCell 2000 Analyzer, and PI positive and total nuclei counted with a high content image analysis algorithm (see **Section 0**) (B). Values shown are % of PI-positive cells calculated via (100 * PI-positive nuclei / Hoechst-positive nuclei). *Multiplicity-adjusted p<0.05 via one-way ANOVA and post-hoc tests with Holm-Sidak adjustment for multiple comparisons.

Decreased mitochondrial respiratory capacity may arise from a variety of insults. To determine if the decreases in respiratory capacity observed are preceded by changes

in mitochondrial morphology or membrane potential, a high content microscopic technique developed in our lab was employed to evaluate the interconnectedness of mitochondria in living 661w cells in response to IBMX [114]. Briefly, this method detects fluorescently labeled mitochondria in micrographs of living or fixed cells using automated segmentation and then classifies each mitochondrion found into one of four bins based on its shape: punctate, rod-like, networked, or large & round (swollen). The area represented by each morphological subtype is then aggregated for each individual cell and normalized to the total mitochondrial area within each cell to obtain a proportion for each individual subtype. Using this method, an increase in the proportion of mitochondria that display networked morphology is observed within the first hour of treatment at IBMX concentrations 100 µM and less (**Figure 4-3**).
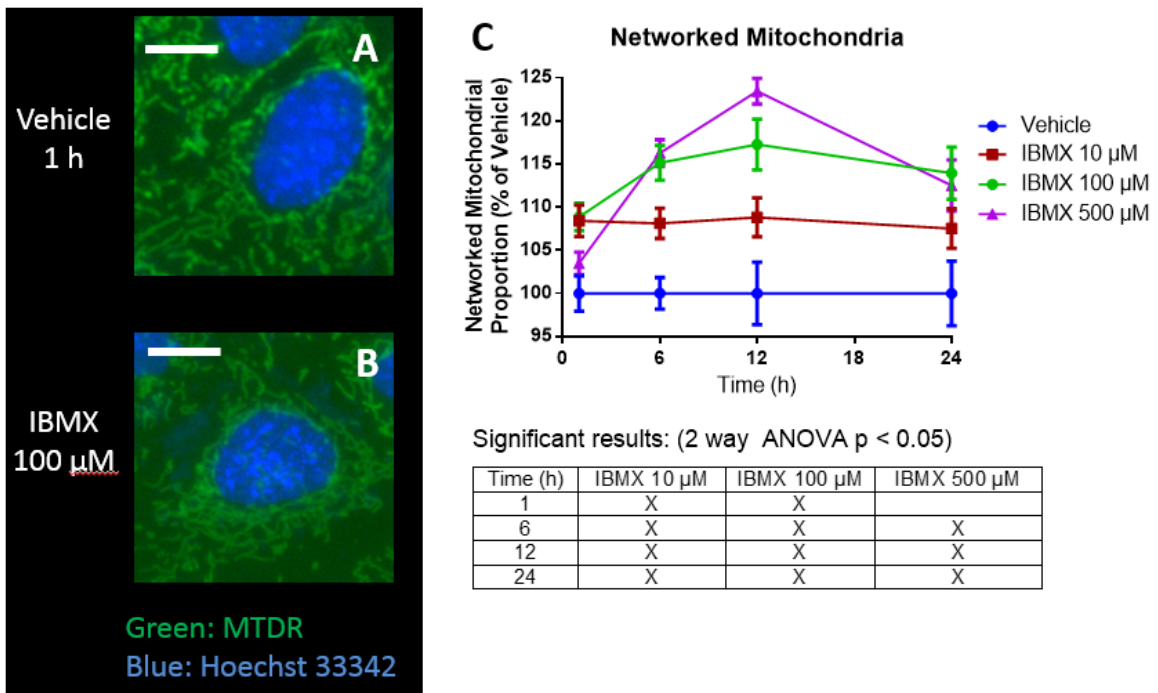
Figure 4-3. IBMX Administration Induces Rapid and Sustained Mitochondrial Fusion.

661w nuclei and mitochondria were stained with Hoechst 33342 (false colored blue) and MitoTracker Deep Red (MTDR, false colored green), treated with IBMX or vehicle (0.1% DMSO) for the indicated periods of time and imaged using the GE INCell Analyzer 2000 (A, B). Mitochondrial morphology was assessed using the method of Leonard et al [114] and proportion of mitochondria with networked morphology displayed in (C). Data shown are mean ± s.e.m. of n=6 experiments. Scale bar is 10 µm. Data were analyzed via 2-way ANOVA (explanatory variables of time and IBMX concentration) and post-tests comparing each concentration v. vehicle at each time point. "X" in table denotes Holm-Sidak multiplicity-adjusted $p<0.05$ v. vehicle.

Next, the effects of IBMX administration on mitochondrial membrane potential

($\Delta\Psi_m$) were determined. Interestingly, 50-100% increases in TMRM fluorescence

intensity v. vehicle were observed as early as 4 h following administration of IBMX at 10-

500 µM, indicating mitochondrial membrane hyperpolarization (**Figure 4-4**).

As electron transport chain complexes (ETC) effectively form an electrical circuit

(protons pumped from matrix to intermembrane space via ETC I, III, and IV; protons flow

from intermembrane space to matrix via ETC V ATP synthase), this circuit can be

described according to Ohm's law, expressed in general and mitochondrial forms in

Equation 4-1 and **Equation 4-2**.

$$V = I * R$$

Equation 4-1. Ohm's Law (general form).

V is electrical potential in volts, I is current in amps, and R is resistance in ohms.

$$\Delta\Psi_m \approx QO_2 * R$$

Equation 4-2. Ohm's Law (mitochondrial symbols).

$\Delta\Psi_m$ is the potential difference between mitochondria and a reference point (nucleus in this report), Ψ_m is absolute mitochondrial membrane potential, QO_2 is oxygen consumption, a surrogate of mitochondrial respiration which approximates to flow of protons across mitochondria inner membrane, and R is resistance. "Approximately equal to" symbols are utilized here to recognize the non-mitochondrial sources of oxygen consumption and the non-linear nature of $\Delta\Psi_m$ measurement via fluorescence microscopy.
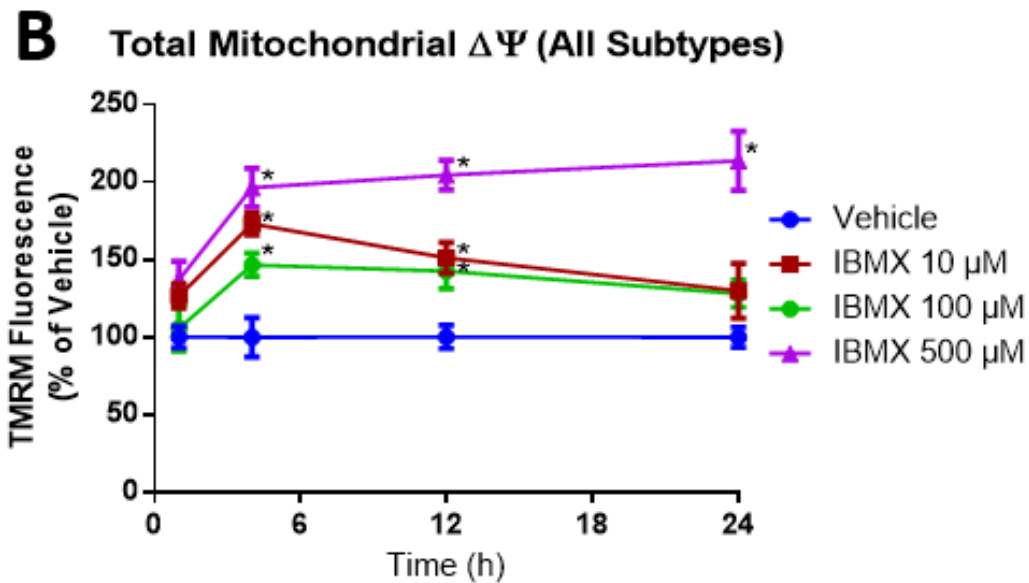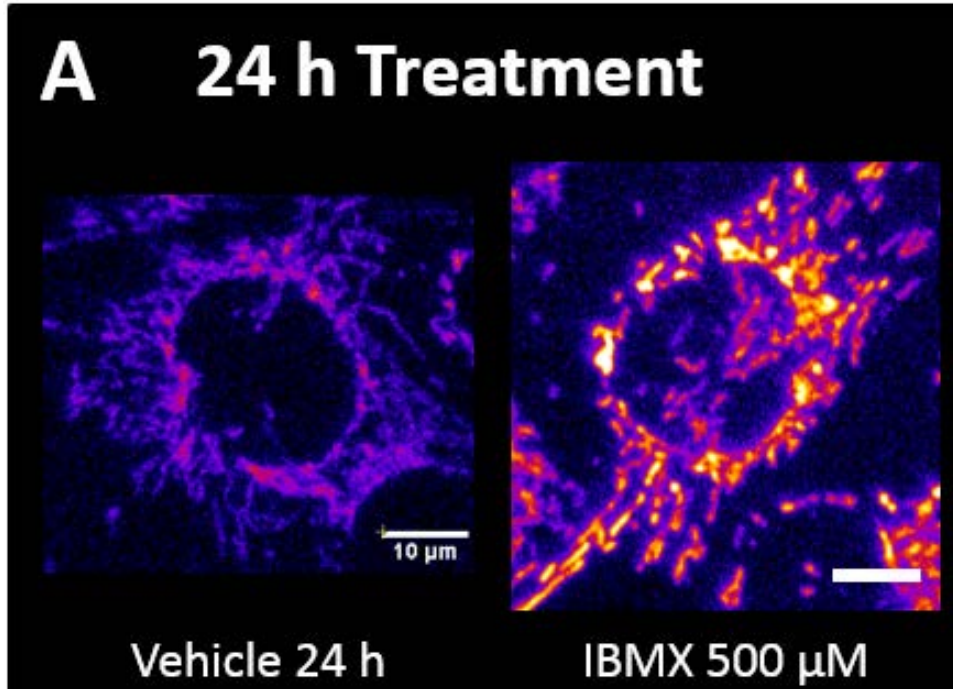
Figure 4-4. IBMX Induces Mitochondrial Membrane Hyperpolarization (↑ΔΨ$_m$).

661w cells were stained with MitoTracker Deep Red and tetramethylrhodamine methyl ester (TMRM) and subjected to membrane potential analysis as previously described [114]. At 1, 6, 12, and 24 h following treatment, cells were visualized and ΔΨ$_m$ measured by subtracting the nuclear fluorescence intensity from the average fluorescence intensity of all mitochondria within each cell. Values are shown as percentage of vehicle control at each time point. Data shown are mean ± s.e.m. of n=6 experiments. *multiplicity-adjusted $p < 0.05$ v. vehicle at each time point by two-way ANOVA.

Using algebraic interpretation of these equations, it may be interpreted that at 24 h, the IBMX-induced increase in electrical potential accompanied by a decrease in current is likely reflective of an increased resistance of the mitochondrial membrane to inward proton flow. Sources of increased resistance along the electron transport chain are diverse and include phosphorylation of ETC complexes, tighter coupling of the mitochondrial inner membrane via loss of uncoupling protein expression, increased high energy electron substrate availability, or decreased availability of ADP and inorganic phosphate for ETC Complex V to use as substrate.

To elucidate a mechanism by which these electrophysiological parameters are perturbed by IBMX, studies began with examination of the mitochondrial permeability transition pore (PTP). PTP opening has been shown to regulate membrane potential and is the only known method by which mitochondria are able to exchange ADP for ATP [117, 118]. To ask the question of whether or not PTP opening plays a role in IBMX-induced membrane potential changes in 661w, the role of PTP stabilizing protein cyclophilin D (CyD) via the inhibitor cyclosporin A was evaluated. Cyclosporin A also inhibits protein phosphatase calcineurin (Ppp3ca). Calcineurin inhibition by FK506 (tacrolimus) and its analogs (rapamycin, cyclosporin A, ascomycin) is dependent upon binding to ubiquitously expressed protein FK506 binding protein FKBP12. The murine ortholog (Fkbp1a) of the human FK506 binding protein (FKBP12) is expressed abundantly in the 661w cell line as assessed using genome-wide expression profiling (see **Section 4.3.4**). Using 1 µM cyclosporin A, which inhibits both PTP regulator cyclophilin D and phosphatase calcineurin, an increase is observed in mitochondrial membrane potential (130-140% of control) but no change in interconnectedness is observed. Increasing the concentration to 10 µM cyclosporin A increases mitochondrial membrane potential further (to 200-220% of control; beyond the 150-175% of control

induced by IBMX), and a small (110% of control) increase in mitochondrial interconnectedness at 24 h is observed (**Supplementary Figure 12**).

To determine if these cyclosporin A-induced phenomena are a result of inhibition of CyD/PTP or calcineurin (Ppp3ca), the calcineurin-selective inhibitor ascomycin was next examined. At 10 nM, ascomycin induced an increase in membrane potential at 24 h, but no change in networked morphology. Increasing the concentration to 100 nM resulted in increased membrane potential at 1, 5, and 24 h similar in magnitude to that induced by 500 µM IBMX with a 60% decrease in networked morphology at 24 h (**Supplementary Figure 13**). Further increasing the dose of ascomycin to 1 µM resulted in a rapid and massive increase in membrane potential (500% of control at 1 h, 300% at 24 h; versus 150-175% of controls for IBMX), accompanied by an increase in network morphology at 24 h (125% of control).

PTP opening is also regulated by glycogen synthase kinase 3-β (GSK-3β). In order to understand its role, the selective GSK-3β inhibitor 3F8 was evaluated (3F8 IC_{50} for GSK-3β: 34-304 nM depending on [ATP]). Following administration of 100 nM or 1 µM 3F8, increased mitochondrial membrane potential was observed (120-140% of control values) within 1 h (**Supplementary Figure 14**). At 24 h, membrane potential at either dose was not significant from controls. 3F8 administration induced no significant effect on mitochondrial networked proportion. At lower concentrations (1-10 nM), 3F8 induced no significant effects when administered alone (data not shown). A similar concentration response was obtained with LiCl administration at 1 h (also inhibits GSK-3β; data not shown). To determine if GSK-3β activation plays a role in transducing altered mitochondrial physiology following administration of IBMX, GSK-3β inhibitor 3F8 was administered 1 h prior to administration of IBMX. Interestingly, pretreating 661w cells at 1 nM, a concentration of 3F8 lower than that necessary to induce altered

physiology when administered alone, resulted in significant prevention of increases in networked morphology and membrane potential (**Figure 4-5**).
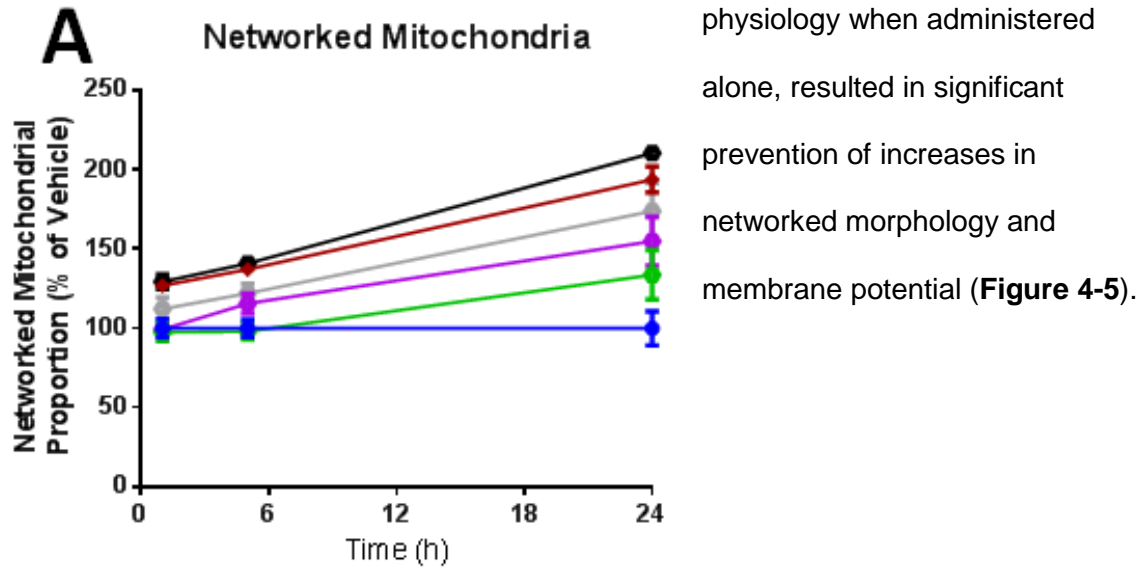
Time (h)	Vehicle	I+3F8 1 nM	10 nM	100 nM	1 µM
1	X	X			
5	X	X			
24	X	X	X		
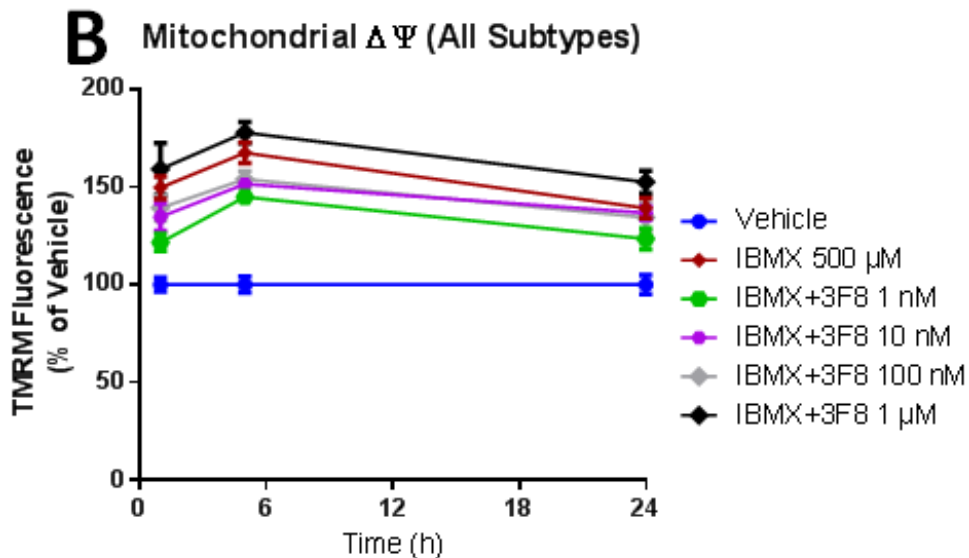
Time (h)	Vehicle	I+3F8 1 nM	10 nM	100 nM	1 µM
1	X	X			
5	X	X			
24	X				

Figure 4-5. GSK3-β (Gsk3b) inhibition partially reverses IBMX-induced alterations in mitochondrial networked morphology and membrane potential.

661w photoreceptor cell line mitochondria were subjected to morphological and membrane potential analysis as previously described [114]. Proportion of networked mitochondria following 24 h treatment is presented in (A), and mitochondrial membrane potential in (B). Data shown are mean ± s.e.m. of n=4 experiments. "X": multiplicity-adjusted $p<0.05$. Analyzed by one-way (A) or two-way ANOVA (B), post-test treatment group versus IBMX at each time point.

4.5 Discussion

In this study, IBMX was observed to induce mitochondrial membrane hyperpolarization and increased networked morphology at 1 h and 4 h (respectively), which were followed by decreased mitochondrial respiratory capacity at 24 h, eventually followed by increased cell death at 48 h. To our knowledge, the combination of these effects has not been previously described for a single agent, although a recently published paper demonstrated 100 µM IBMX pretreatment increased mitochondrial form factor (a measure of interconnectedness) in patient-derived olfactory neurons, and furthermore prevented mitochondrial fragmentation induced by mutations in a putative Zn^{2+} active transport pump, or by exogenous administration of Zn^{2+} [119]. Insights into a mechanism of action that includes membrane hyperpolarization include inhibition of mitochondrial electron transport chain (ETC) Complex V, stimulation of the tricarboxylic acid cycle or other pathways that increase high energy electron carriers NADH or $FADH_2$, or alteration of mitochondrial membrane permeability transition pore (PTP) opening. Previous studies with Complex V inhibitor oligomycin (**Figure 3-4** and **Figure 3-6**) demonstrated increased membrane potential and decreased respiratory capacity were not associated with an increase but instead with loss of networked morphology, suggesting loss of Complex V activity alone may not account for the altered mitochondrial physiology observed with IBMX administration. Inhibition of ATP consumption using ouabain (which should increase high energy electron carrier concentrations) similarly resulted in fragmentation: **Figure 3-4**).

Although the absolute amounts of cell death observed in **Figure 4-2** were lower than expected (increasing from only 0.4% in vehicle treated cells to 1.6% in cells treated with 500 µM IBMX), this likely is due to the majority of dead (propidium-stained) cells lifting off of the plate bottom and not being within the imaging plane at time of assay.

Manual inspection of IBMX-treated wells indeed demonstrated fewer total (Hoechst 33342-stained) cells remaining. Thus, the data are likely more reflective of a death rate assay as only recently dead cells remain on the well bottom.

Taken together, the data in **Supplementary Figure 12** and **Supplementary Figure 13** demonstrated the difficulty in understanding the role PTP opening by cyclosporin A-mediated inhibition of cyclophilin-D (CyD), as pure calcineurin inhibition by ascomycin appeared to regulate 661w mitochondrial membrane potential and morphology independent of CyD. The results highlighted an inability to distinguish between calcineurin-mediated effects and mediated effects in these experiments. Thus, concomitant administration of cyclosporin A with IBMX was not pursued.

A second attempt to understand the role of PTP opening in mediating IBMX-induced alterations in physiology was more fruitful as GSK-3β inhibitor 3F8 (expected to lead to increased closure of PTP) induced a transient (1-5 h) increase in mitochondrial membrane potential at 100 nM and higher (**Supplementary Figure 14**). Very interestingly, concomitant administration of IBMX and 3F8 at concentrations of 3F8 lower than those needed to induce changes by 3F8 alone demonstrated a reversal of IBMX-induced changes, suggesting that IBMX-induced activation of GSK-3β is at least in part responsible for increasing mitochondrial membrane potential and networked morphology in 661w (**Figure 4-5**). Although future studies will be needed to further elucidate the signaling pathways involved, these experiments suggest that either excess inhibition of GSK-3β or IBMX-induced activation of GSK-3β both result in mitochondrial membrane hyperpolarization and dysregulation of mitochondrial morphology prior to loss of mitochondrial respiratory capacity and cell death.

4.6 Conclusion

In this study, the effects of 3-isobutyl 1-methylxanthine (IBMX) on mitochondrial physiology are demonstrated – namely, decreased mitochondrial respiration as measured by decreases in mitochondrial respiratory capacity, which is preceded by increases in networked morphology and increased mitochondrial membrane potential ($\Delta\Psi_m$). As IBMX is commonly used as an inhibitor of cyclic nucleotide phosphodiesterase enzymes, this work highlights the potential confounding effects of IBMX use on cellular bioenergetics and cell signaling in physiological studies. Furthermore, IBMX administration to 661w photoreceptor cells recapitulates the phenomena of mitochondrial functional loss preceding cellular death in inherited retina degeneration, providing additional support to the use of 661w as a cell-based photoreceptor model. Data are shown that demonstrate that GSK-3β inhibition alone and IBMX administration alone hyperpolarize mitochondria; however, the combination of the two leads to mitigation of effects. A plausible explanation for this result is that IBMX administration leads to activation of GSK-3β, raising the question of whether decreased or increased PTP opening is responsible for IBMX-mediated alterations in mitochondrial physiology.

5. Chapter 3—IBMX Inhibition of Cyclic GMP Phosphodiesterases Leads to Mitochondrial Dysfunction

5.1 Abstract

3-isobutyl 1-methylxanthine (IBMX) is a commonly used non-selective inhibitor of cyclic nucleotide phosphodiesterases (PDEs). This report describes the role of selective PDE inhibition in conveying the mitochondrial and cellular toxicities induced by IBMX in the photoreceptor-derived cell line 661w. Following administration of IBMX, a concentration- and time-dependent increase in networked morphology (102-120% of control) was followed by increased membrane potential (tetramethylrhodamine methyl ester fluorescence intensity 125-200% of control) and decreased mitochondrial respiratory capacity (30% of control at 24 h). These changes were recapitulated entirely or partially (respectively) by PDE5-selective inhibitor of sildenafil and PDE3-selective inhibitor cilostamide. IBMX induced cell death (400% of control at 48 h), but this toxicity was not observed with inhibition of either PDE3, PDE5, or both. IBMX led to increased cAMP and cGMP, but PDE3 and PDE5 inhibition selectively increased cGMP. Taken together, these results indicate that cGMP is a strong regulator of mitochondrial physiology and alterations may occur to a large extent without effects on cellular viability. The results also suggest that increased cAMP or another as yet to be determined target of IBMX are responsible for 661w photoreceptor cytotoxicity. As mitochondria are central to regulating cellular bioenergetics and programmed cellular death, these results have implication for researchers in a broad variety of fields ranging from physiology and neuroscience to pharmacology.

5.2   Introduction

3-isobutyl 1-methylxanthine (IBMX) is a well-known and widely used non-selective inhibitor of cyclic nucleotide phosphodiesterase (PDE) enzymes. However, the role of individual phosphodiesterase enzymes in regulating mitochondrial physiology is poorly understood. In **Section 4**, the effects of IBMX on mitochondrial physiology are discussed (**Chapter 2—IBMX Administration Results in Mitochondrial Membrane Hyperpolarization, Increased Network Morphology, and Decreased Respiratory Capacity**). The goal of the present work is to characterize the roles of individual PDE enzymes in conducting IBMX-induced alterations in mitochondrial physiology.

As a non-selective inhibitor of PDE enzymes, IBMX has been characterized to inhibit PDE isoforms PDE1-PDE8. PDE enzymes catalyze the cleavage of the intramolecular 3'-5' phosphodiester bond in cyclic adenosine monophosphate (cAMP) or cyclic guanosine monophosphate (cGMP). Individual PDE isoforms may display selectivity towards cAMP or cGMP or cleave both cyclic nucleotides. **Table 5-1** summarizes the cyclic nucleotide selectivity of PDE isoforms and their expression within 661w as determined by genome-wide expression profiling.

Cyclic Nucleotide	PDE1	PDE2	PDE3	PDE4	PDE5	PDE6	PDE7
cAMP	X	X	X	X	no	no	X
cGMP	X	X	X	no	X	X	no

Table 5-1. IBMX-sensitive Cyclic Nucleotide Phosphodiesterase Enzymes and Their Selectivity

LEGEND: 'X': PDE isoform cleaves the cyclic nucleotide on the same row; 'no': PDE isoform unable to cleave the cyclic nucleotide on the same row; White: expressed in 661w; Gray: no expression. Expression determined using the genome-wide expression profiling method described in **Section 5.3.2**.

5.3 Materials and Methods

5.3.1 Cell Culture

661w photoreceptor cells were generously provided by Dr. M. Al-Ubaidi (University of Oklahoma) [18] and maintained under standard conditions using DMEM-HG media (Sigma-Aldrich #D-7777) supplemented with 10% fetal calf serum (FCS, Atlanta Biologicals #S11550) and 1 mM L-alanyl-L-glutamine (GlutaMAX) (Life Technologies #35050-061). For imaging studies, cells of passages 15-25 were cultured to 80% confluency before trypsinization and seeded at a cell density of 8,900 cells per well in 96 well plates (Nunc Edge Plate, Thermo Scientific #167314) supplemented with 5% FCS and edge reservoirs filled with 1x phosphate buffered saline, (PBS, Life Technologies #14080-055). After allowing cells to reach 80% confluency (24 h), cells were washed in PBS, and media was changed to DMEM with 5.5 mM glucose without phenol red (Sigma-Aldrich #D-5030) supplemented with 1% FCS to induce cell cycle arrest. Cells were used for experiments 24 h after this switch to normal glucose and 1% FCS-containing media, with treatments for either 24 h (morphological analysis) or 1 h (membrane potential analysis). All compounds used for treatment were from Sigma-Aldrich (St. Louis, MO) unless otherwise specified, and were prepared at 1000x concentration in DMSO before administration to cells (final [DMSO] = 0.1%).

5.3.2 Genome-wide Microarray Expression Profiling

mRNA was isolated from 661w cells grown in 10 cm dishes to confluence and purified using the RNeasy RNA purification kit (Qiagen, Valencia, CA). cDNA was synthesized from high-quality RNA ($A_{260/280} \geq 1.80$) and subjected to microarray analysis using conditions identical to those described previously [116]. Briefly, GeneChip Mouse Genome 430 2.0 oligonucleotide arrays (Affymetrix) were hybridized with equal amounts

of labeled cRNA (15 µg/array) and readout were performed by the DNA Microarray Core Facility at the Medical University of South Carolina using the Affymetrix Fluidics Station.

5.3.3 Determination of Cyclic Nucleotide Concentrations

661w cells were seeded at 200k in 10 cm dishes and cultured in DMEM-HG supplemented with 5% FCS and incubated for 72 h to allow cells to reach 80% confluency. Media was then changed to DMEM-HG supplemented with 1% FCS and cells incubated an additional 24 h to allow for synchronization of cell cycle. Cells were at 90-100% confluency at time of treatment. Treatments were made at the indicated concentrations in DMEM-HG supplemented with 1% FCS with a final DMSO concentration of 0.1% (v/v) and equilibrated in 5% CO_2 at 37 °C before being administered for 20 min at 37 °C in 5% CO_2. Following this incubation, media was withdrawn and cells were washed one time with phosphate buffered saline containing no Ca^{2+}/Mg^{2+} (Life Technologies) and 200 µL of 100 mM HCl was immediately added to each plate. Plates were scraped at room temperature and samples immediately placed on ice. Samples were centrifuged at 14,000 x g and pellets discarded. Supernatants were assayed directly for cAMP or cGMP via EIA using manufacturer's protocol (Catalog #581001 or #581021, Cayman Chemical, Ann Arbor, MI, USA). Unless otherwise specified, all chemicals were from Sigma-Aldrich (St. Louis, MO, USA) and were of reagent grade or higher.

5.3.4 High Content Determination of Mitochondrial Morphology and Membrane Potential

To evaluate the concentration- and time-dependency of IBMX-induced mitochondrial changes, we employed the method of Leonard et al. [114]. Briefly, 661w cells were seeded into Nunc Edge 96-well plates (Fisher) at a density of 8900/well and

incubated in DMEM-HG (Invitrogen) for 24 h. Media was changed to DMEM

supplemented with 1% FCS and incubated overnight before staining. 661w cells were

loaded with 50 nM MitoTracker Deep Red, and 10 µM Hoechst 33342 for 30 min and

then washed followed by a 3 h incubation at 37 °C in DMEM-HG supplemented with 1%

FCS. After 3 h, cells were treated with IBMX at the indicated concentrations and cells

imaged. Imaging was performed on a GE INCell Analyzer 2000 automated wide-field

fluorescence microscope using a 40x Nikon ELWD objective (NA 0.6) matched with the

large-format 2048x2048 pixel 12-bit Coolsnap K4 camera. Images were saved in the

TIFF image file format and subjected to the high content mitochondrial morphological

analysis as described in **Section 3**, **Chapter 1—Quantitative Analysis of
Mitochondrial Morphology and Membrane Potential in Living Cells Using High
Content Imaging, Machine Learning, and Morphological Binning**.

5.3.5 Seahorse XF96 Respirometry

661w photoreceptor cells were seeded (6,000 cells/well) into XF96 polystyrene

plates (Seahorse Biosciences, Billerica, MA) and incubated for 48 h in DMEM-HG

(Sigma-Aldrich) supplemented with 5% FCS. Media was then changed for DMEM

supplemented with 5.5 mM glucose and 1% FCS and vehicle or toxicant treatments

administered for 24 h. Just prior to time of assay, media was switched to bicarbonate-ion

free RS (reduced serum) buffer at pH 7.4 prepared with 130 mM NaCl, 5.33 mM KCl, 1.8

mM $CaCl_2$, 0.6 mM $MgCl_2$, 0.5 mM KH_2PO_4, 0.5 mM $NaPO_4 \cdot (H_2O)_7$, insulin, 5.5 mM

glucose, and supplemented with 1% FCS, 1 mM L-alanyl-L-glutamine (GlutaMAX), 2 mM

glutamine, 1% MEM Vitamins, 1% MEM Amino Acids, 1% MEM Non-Essential Amino

Acids, 1% Penicillin/Streptomycin. All inorganic salts used were obtained from Sigma-

Aldrich (St. Louis, MO) and organic supplements obtained from GIBCO/Life

Technologies (Grand Island, NY) unless otherwise noted. All oxygen consumption rate

(OCR) measurements used cycle times of 4 minutes per mix (probes moving) and 3 minutes per measure (probes down). After recording 3 baseline OCR measurements, oligomycin (100 nM) was administered and 3 additional OCR measurements obtained. This was followed by administration of FCCP (carbonyl cyanide-p-trifluoromethoxyphenylhydrazone) (1 µM) and two OCR measurements obtained. Finally, a combination of rotenone (5 µM) and antimycin A (100 nM) was administered and two final OCR measurements obtained. Uncoupled OCR's for each condition were recorded and reported as mean +/- standard error of the mean (s.e.m.) across experiments by subtracting the final rate (non-mitochondrial respiration, determined following rotenone and antimycin A) from the first rate obtained following FCCP administration.

5.3.6 Cytotoxicity Determination via Propidium Dye Exclusion

For cytotoxicity experiments, 661w cells were seeded at a density of 6,000 cells/well in DMEM-HG supplemented with 5% FCS. 24 h later, this media was withdrawn and changed to DMEM-HG supplemented with 1% FCS. 48 h following seeding, treatments were administered in DMEM-HG supplemented with 1% FCS (final [DMSO] = 0.1%). Cells were incubated with these treatments for 48 h before imaging on the GE INCell Analyzer 2000. Prior to imaging, conditioned media containing treatments was withdrawn and incubated at 37 °C in 5% CO_2 balance air. Cells were stained for 30 min with 10 µM Hoechst 33342 and 1.5 µg/mL propidium iodide (PI, Sigma) in serum-free DMEM-HG. Following staining, cells were washed once with PBS containing Ca^{2+}/Mg^{2+} (GIBCO/Life Technologies), and then conditioned media was returned to cells and cells incubated at 37 °C until imaged (10-45 minutes). Images were captured using the DAPI filter set for Hoechst and the Cy3 filter set for PI, with a Nikon 10x ELWD objective, and saved in TIFF format. Images were analyzed in Developer Toolbox, with Object segmentation used to identify all nuclei in the DAPI-filtered images (Hoechst

65

stain) and a second Object segmentation used to identify PI-stained nuclei in the Cy3-filtered images. The measure of % PI-Positive Cells was obtained by dividing the PI-positive nuclei count by the total (Hoechst-stained) nuclei count and then multiplying by 100.

5.3.7 Statistical Analysis

Statistical analysis was conducted using either one-way ANOVA or two-way ANVOA, respectively, for single time-point (>2 concentrations/treatments) or multiple time-point and multiple concentration experiments. Holm-Sidak multiplicity-adjusted post-hoc analyses were conducted in each analysis to compare across treatment groups (not timepoints) and p values < 0.05 were considered significant.

5.4 Results

5.4.1 IBMX Administration Leads to Increased Intracellular [cAMP] and [cGMP]

As a first effort to delineate the PDE isoforms responsible for the mitochondrial physiological effects observed, the concentration of intracellular cyclic nucleotides cAMP and cGMP was measured following administration of IBMX or selective PDE inhibitors. The results indicate a 140% increase in intracellular cAMP and a 3,400% increase in intracellular cGMP following IBMX treatment. cGMP-specific PDE5 inhibitor sildenafil (PDE5 IC_{50}: 4 nM) and PDE3-selective inhibitor cilostamide (PDE3 IC_{50}: 50 nM) were observed to have no effect on cAMP, but induced an increase in [cGMP] 8,000% and 1,600% of control values, respectively (**Figure 5-1**).
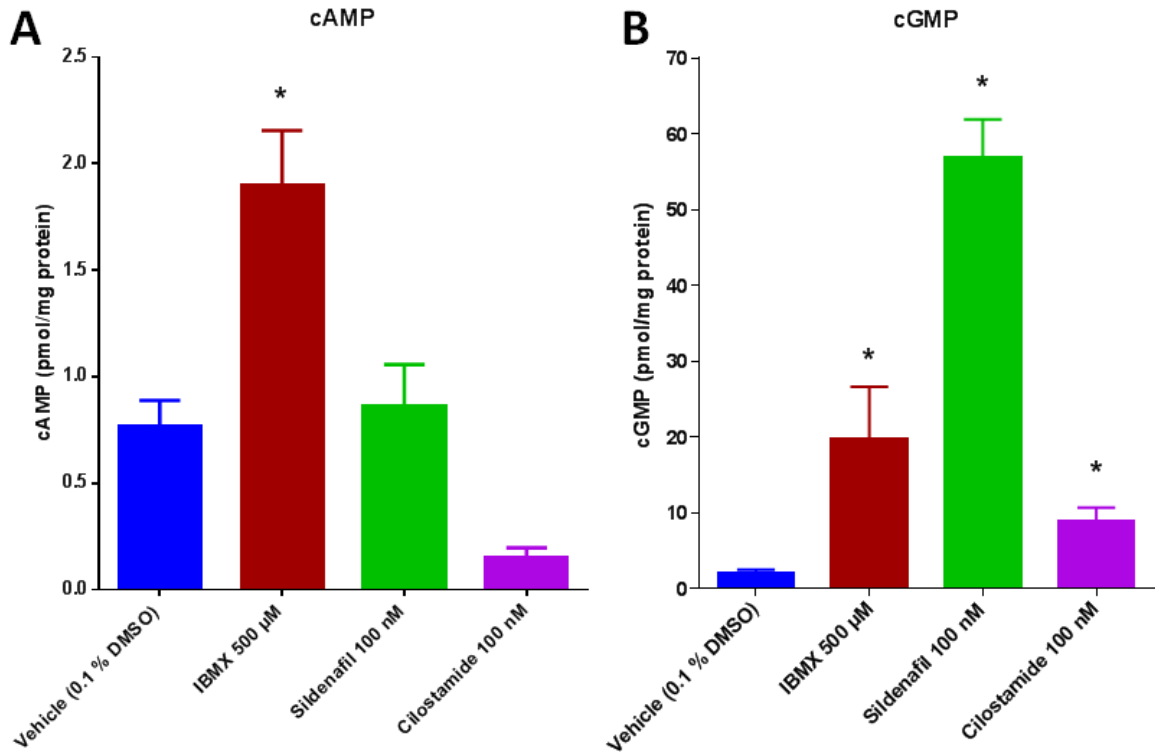
Figure 5-1. IBMX and Selective PDE Treatments Increase cAMP and cGMP

661w cells were washed and lysed following 20 min treatment with compounds at the indicated concentrations and cAMP or cGMP concentration determined via a commercially available enzyme-linked immunosorbance assay (**Section 5.3.2**). Data shown are mean ± s.e.m of n=3 experiments. *multiplicity-adjusted $p < 0.05$ by one-way ANOVA; multiple comparisons made v. vehicle and adjusted via Holm-Sidak.

As IBMX induced increases in both cAMP and cGMP, it was next sought to determine which cyclic nucleotide phosphodiesterase isoform(s) were able to recapitulate the alterations in mitochondrial physiology observed in **Section 4**, **Chapter 2—IBMX Administration Results in Mitochondrial Membrane Hyperpolarization, Increased Network Morphology, and Decreased Respiratory Capacity** using a high content analysis algorithm developed in the lab [114].

5.4.2 The Role of cAMP-selective Phosphodiesterase Inhibition in Regulating Mitochondrial Physiology

As IBMX administration increased both intracellular cAMP and cGMP, the two cAMP-selective phosphodiesterases expressed in 661w were first examined, PDE4 and PDE7. Interestingly, rather than inducing a decrease in uncoupled respiration, selective inhibitors of these enzymes increased uncoupled respiration. At a concentration of 1 μM, the selective inhibitor of PDE4 rolipram (IC$_{50}$ 313 nM [120]), increased uncoupled respiration by ~45%. At concentrations of 10 μM and 100 μM, ~60% increases in uncoupled respiration were observed with BRL 50481 (IC50 2.4 μM [121]) (**Figure 5-2**).
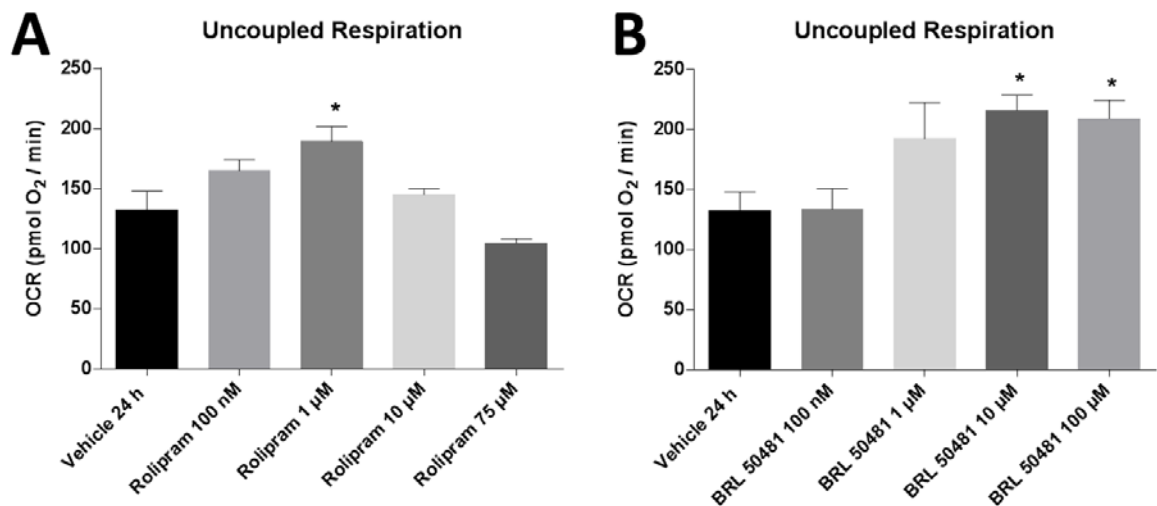
Figure 5-2. PDE4 and PDE7 Inhibition Increase, not Decrease Uncoupled Respiration.

Data are mean ± s.e.m. of n=4 experiments; analyzed by one-way ANOVA with Holm-Sidak correction for multiple comparisons. *p<0.05 v. vehicle.

5.4.3 The Role of PDE5-cGMP in Regulating Mitochondrial Physiology
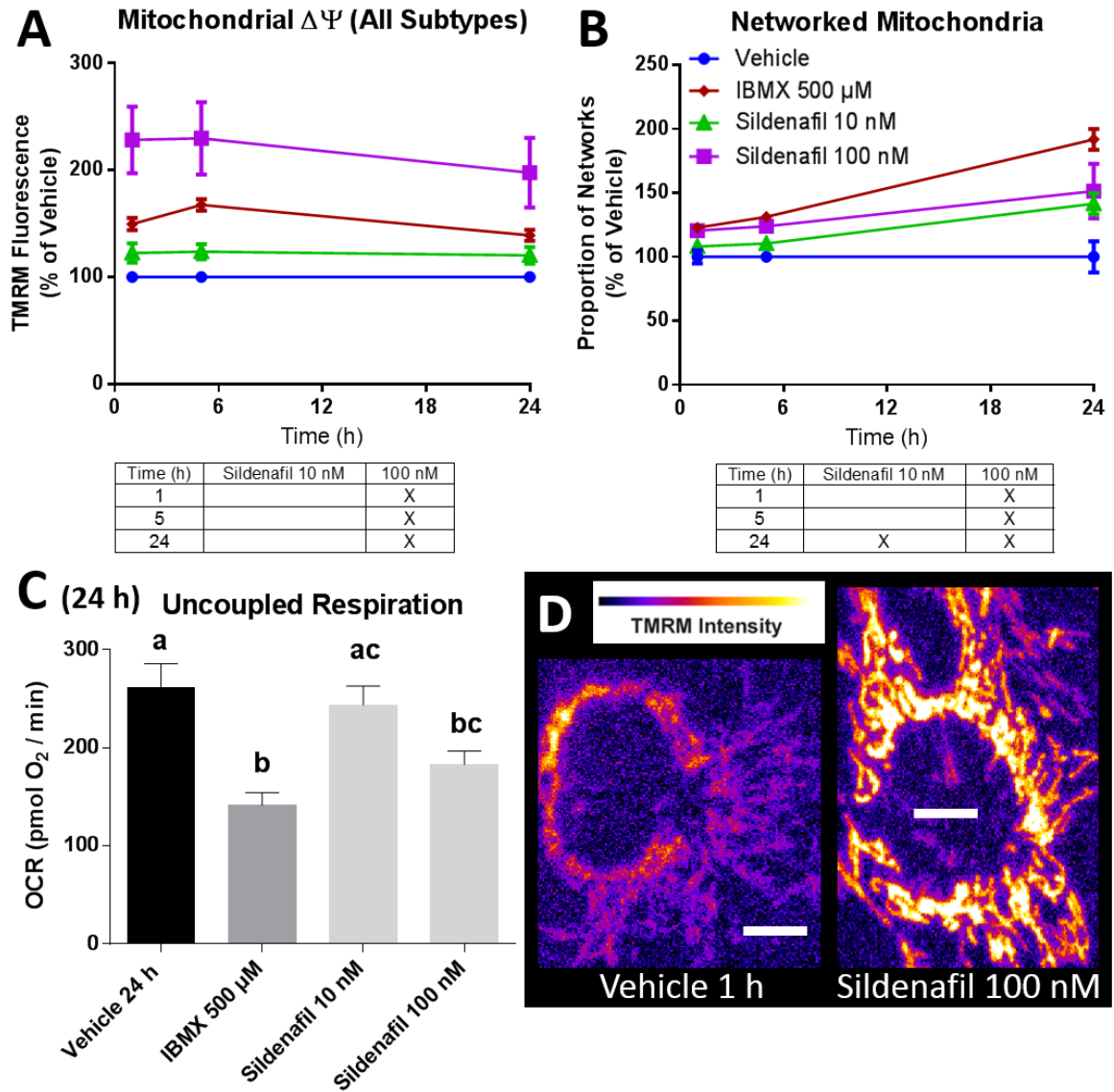
Figure 5-3. Inhibition of PDE5 recapitulates IBMX-induced alterations in mitochondrial physiology.
High-content analysis of mitochondrial membrane potential (A, D) and networked morphology (B, D) of 661w cells were conducted using the method of Leonard et al. [114]. Seahorse XF96 respirometry was conducted at 24 h following treatment with compounds at the indicated concentration (C). Data shown are mean ± s.e.m. of n=4 experiments and were analyzed by one-way (C) or two-way (A, B) ANOVA with Holm-Sidak correction for multiple comparisons. * or X: $p < 0.05$ v. vehicle. Scale bar 10 μm (D).

At 100 nM, sildenafil administration led to a rapid (at 1 h) and sustained (up to 24 h) increase in mitochondrial membrane potential (200-220% of control), networked morphology (120-140% of control) and decreased uncoupled respiration (70% of control) as measured by Seahorse XF96 respirometry (**Figure 5-3**). At the lower dose of 10 nM,

69

only an increase in networked mitochondria (135% of control) was observed at 24 h. In context with the changes induced by IBMX at 500 μM, sildenafil at 100 nM at all times exceeded the amount of hyperpolarization achieved (200% v. 160% of control), and at later time points partially recapitulated the amount of mitochondrial fusion (135% v. 180% of control). However, at earlier time points, the magnitude of increase in mitochondrial networks induced by sildenafil at 100 nM matched that of IBMX (120% of control).

5.4.4   The Role of PDE2 and PDE3 (cAMP and cGMP) in Mitochondrial Physiology

The third category of phosphodiesterase enzymes according to specificity are the non-selective PDEs, which cleave both cAMP and cGMP. In 661w, two such isoforms are expressed as determined by genome-wide expression profiling, PDE2 and PDE3 (**Table 5-1**). A similar approach was taken in which concentration-response profiles for inhibitors selective for PDE2 and PDE3, BAY60-7550 and cilostamide, were determined first using respirometry. PDE2 inhibition by BAY60-7550 (IC_{50}: 4.7 nM [122]) failed to alter uncoupled respiration (**Figure 5-4**).

At 10 and 100 nM, cilostamide (PDE3 IC_{50} 1.3 μM [123]) led to increased mitochondrial membrane potential (120-140% of control) and decreased uncoupled respiration (80% of control), but failed to recapitulate increased network morphology (**Figure 5-4**). In context with IBMX, the magnitude of these changes was smaller for both membrane hyperpolarization and decreased uncoupled respiration.

Uncoupled Respiration
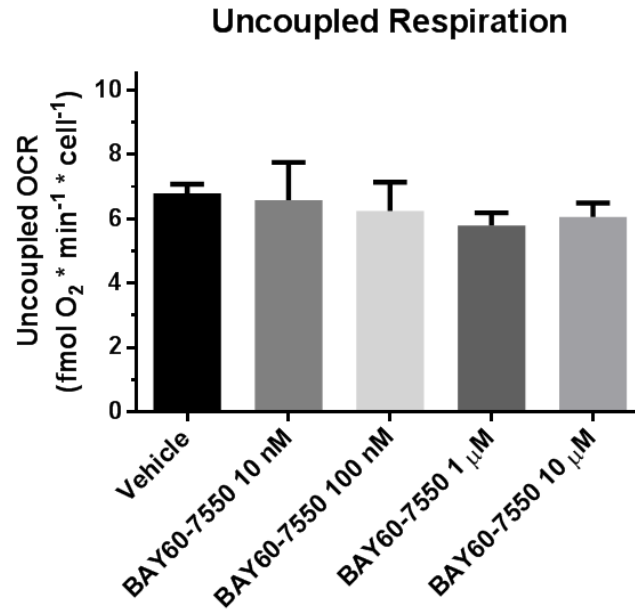
Figure 5-4. PDE2 Inhibition Does Not Alter Mitochondrial Uncoupled Respiration.

24 h treatment. Data are mean ± s.e.m. of n=4 experiments; analyzed by one-way ANOVA with Holm-Sidak correction for multiple comparisons. *p<0.05 v. vehicle.

A Mitochondrial $\Delta\Psi$ (All Subtypes)

Time (h)	Cilostamide 10 nM	100 nM
1	X	
5	X	X
24	X	X

B Networked Mitochondria

Legend:
- Vehicle
- IBMX 500 µM
- Cilostamide 10 nM
- Cilostamide 100 nM

Time (h)	Cilostamide 10 nM	100 nM
1		
5		
24		

C (24 h) Uncoupled Respiration

D TMRM Intensity

Vehicle 1 h   Cilostamide 100 nM
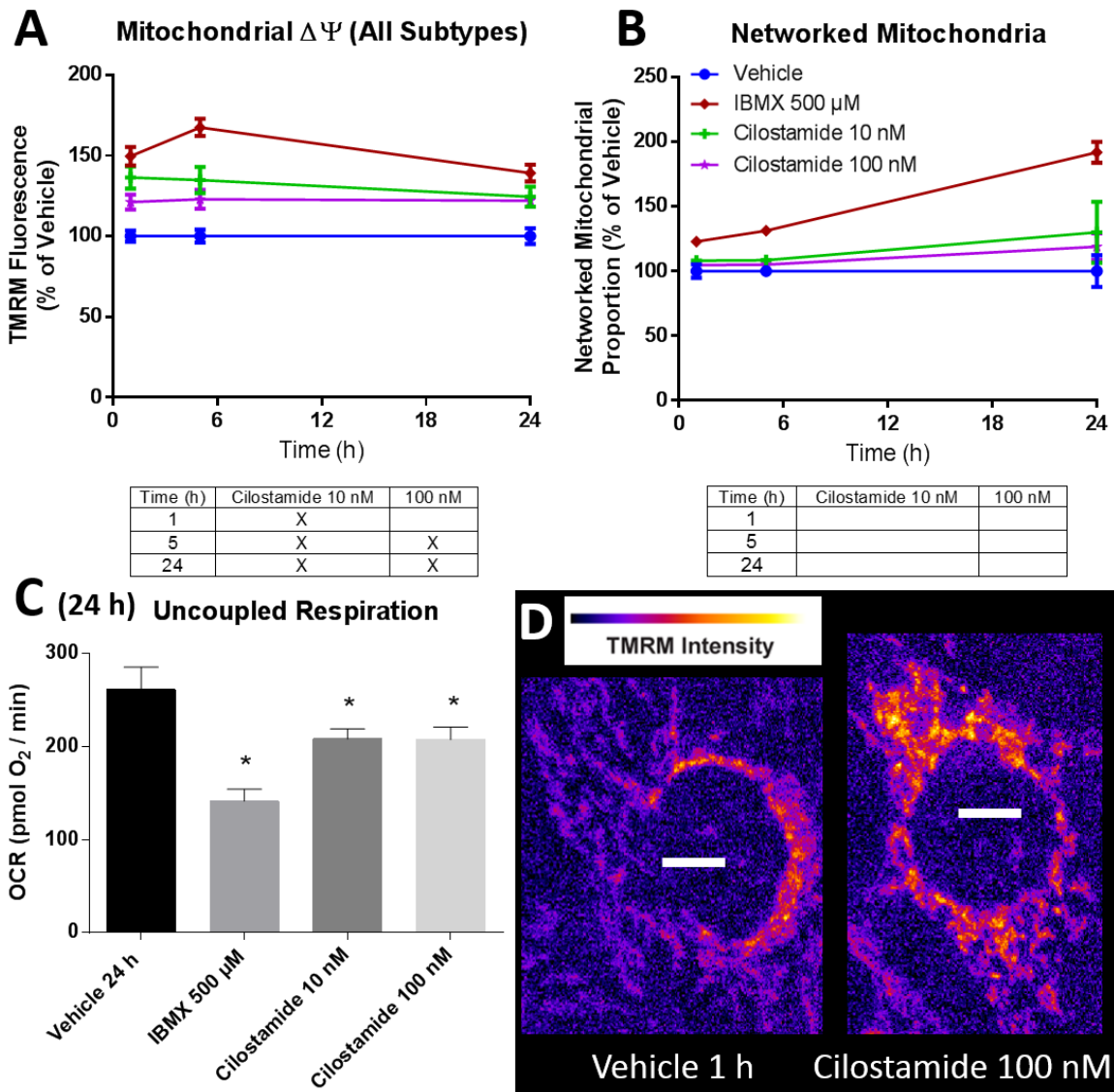
Figure 5-5. PDE3 Inhibition Increases Mitochondrial Membrane Potential and Decreases Uncoupled Respiration but Induces No Changes in Mitochondrial Networks.

High-content analysis of mitochondrial membrane potential (A, D) and networked morphology (B, D) of 661w cells were conducted using the method of Leonard et al. [114]. Seahorse XF96 respirometry was conducted at 24 h following treatment with compounds at the indicated concentration (C). Data shown are mean ± s.e.m. of n=4 experiments and were analyzed by one-way (C) or two-way (A, B) ANOVA with Holm-Sidak correction for multiple comparisons. * or X: $p < 0.05$ v. vehicle. Scale bar 10 µm (D).

5.4.5 Inhibition of PDE3/5 Does Not Increase Cell Death

As IBMX-induced alterations in mitochondrial physiology at 1-24 h were found to be followed by 661w cell death at 48 h, the amount of cell death following PDE3 and PDE5 inhibition was next examined. Neither sildenafil nor cilostamide recapitulated the IBMX-induced increase in number of nuclei staining positive with propidium iodide (400% of control). To determine if concomitant inhibition of PDE3 and PDE5 are required for IBMX-induced cell death, the combination of sildenafil and cilostamide was evaluated. No increase in cell death was observed following the combination, suggesting that IBMX inhibition of PDE3 and PDE5 leads to mitochondrial changes but not cell death (**Figure 5-6**).
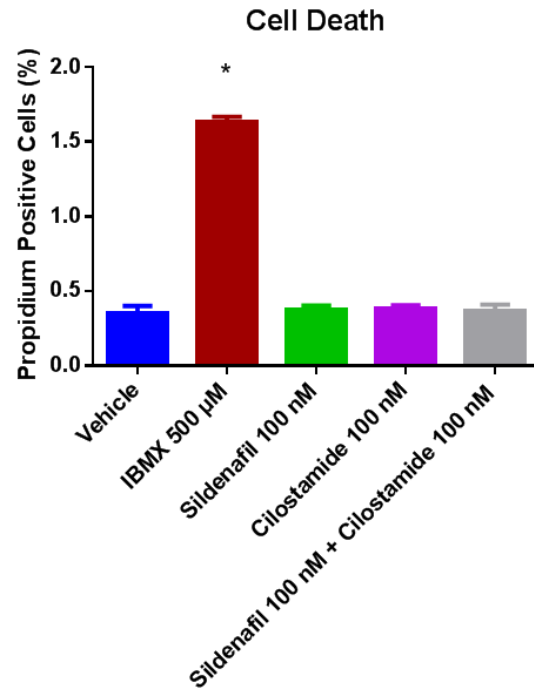
Figure 5-6. Neither PDE5 nor PDE3 inhibition recapitulate IBMX-induced cell death

Data are mean ± s.e.m. of n=11 exps. 661w cells treated for 48 h at the indicated concentrations or with vehicle (0.1% DMSO), then stained with Hoechst 33342 and propidium iodide (PI), imaged using the INCell 2000 Analyzer, and PI positive and total nuclei counted with a high content image analysis algorithm (see **5.3.4**). Values shown are % of PI-positive cells calculated via (100 * PI-positive nuclei / Hoechst-positive nuclei). *Multiplicity-adjusted $p < 0.05$ via one-way ANOVA and post-hoc tests with Holm-Sidak adjustment for multiple comparisons.

5.5 Discussion

As cGMP-selective phosphodiesterase but not cAMP-selective phosphodiesterase inhibition recapitulated IBMX-induced mitochondrial alterations, it would appear that IBMX alters mitochondrial physiology by increasing cGMP in 661w.

As the 661w cells are widely thought to be photoreceptor derived, we were surprised that no PDE6 expression was detected. This isn't the first study showing 661w cells have been shown to be missing a component of the visual transduction pathway, as Fitzgerald et. al. showed CNGA3 is not expressed [22], Tang et. al. showed the absence of RPE65 expression [20], and the original paper from the Al-Ubaidi group characterizing the 661w cells show an absence of several cone photoreceptor proteins, including phosducin, RPE65, peripherin/rds, and ROM1 [19]. Nonetheless, PDE5 and PDE6 share substrate specificity as both cleave only cGMP. Furthermore, following inhibition of PDE5, the 661w cells demonstrate mitochondrial dysfunction, which has been observed in multiple retina degenerative phenotypes [10, 15, 124-127]. Although IBMX recapitulated increased cell death as well, we failed to observe an increase in cell death following isolated inhibition of PDE3, PDE5, or both PDE3 and PDE5. These results suggest a PDE3/PDE5-independent mechanism of action in inducing cell death. Perhaps sustained increased intracellular [cAMP] following IBMX administration is responsible for inducing cell death via an independent pathway. In combination with this lack of cell death induced by cilostamide, this hypothesis is supported by the unexpected result that PDE3 inhibition with cilostamide failed to increase cAMP (**Figure 5-1**). This increase in cAMP may be a result of inhibiting cAMP-specific and cAMP/cGMP PDEs like PDE2, PDE4 or PDE7, or may result by inhibiting targets other than PDEs, such as the cell surface GPCRs like the P_1 class of adenosine receptors [128].

Functional CNG channels, which mediate influx of Ca^{2+} into the cytoplasm, are not expressed in 661w. Ca^{2+} influx normally inactivates guanylate cyclase (GC), a negative feedback mechanism which offsets the cGMP increase induced by inhibition of cGMP-specific PDE's [23]. Administration of PDE inhibitors to purified rod outer segments resulted in only 20-30% increases in intracellular cGMP in the absence of

Ca^{2+} chelator ethylene glycol tetraacetic acid (EGTA) but when EGTA was included, 400% increases were observed, suggesting compensatory GC inactivation was overcome by removing Ca^{2+} stimulus [24]. Indeed, we observe no increased plasma membrane conductance with whole cell electrophysiological recordings obtained following exogenous administration of IBMX or 8-Br cGMP (**Supplementary Figure 11**) and no increase in fluorescence intensity of 661w cells loaded with Ca^{2+} dye Fluo 4-AM was observed following IBMX administration (data not shown). Taken together with the observation that 1,600-8,000% increases in intracellular [cGMP] occur following administration of IBMX, sildenafil, or cilostamide, these observations suggest that IBMX does not require and does not induce increased intracellular Ca^{2+} to alter mitochondrial physiology.

5.6 Conclusion

IBMX administration to 661w cells recapitulates mitochondrial dysfunction and increased cell death observed in several in vivo models of retina degeneration. Alterations in mitochondrial physiology (increased mitochondrial membrane potential and networked morphology with decreased respiratory capacity) appeared to result from increased intracellular [cGMP] following inhibition of PDE3 or PDE5, whereas cell death was not explained by loss of function of these phosphodiesterases. Future studies will elucidate the mechanisms of cell death and examine its dependency on intracellular [cAMP] alterations.

6. Chapter 4—Inverse Agonism of the Adenosine A_{2B} Receptor (Adora2b) Alters Mitochondrial Physiology

6.1 Abstract

The adenosine A_{2B} receptor (A_{2B}) has been increasingly studied as a regulator of mitochondrial susceptibility to ischemia/reperfusion injury, but its role in regulating mitochondrial respiration, morphology, and membrane potential has not been studied. Furthermore, the action of 3-isobutyl 1-methylxanthine (IBMX, a non-selective inhibitor of cyclic nucleotide phosphodiesterase enzymes and adenosine receptors) at A_{2B} has not been studied. Using the 661w retina-derived cell line (expressing only the A_{2B} isoform of adenosine receptor) A_{2B}'s role in regulating mitochondrial physiology, is examined. A_{2B}-selective inverse agonist MRS-1706, but not agonist BAY60-6583 or neutral antagonist PSB-603, recapitulates IBMX-induced alterations. IBMX-induced alterations are reduced by pretreating with BAY60-6583 or PSB-603. Similarly, prior activation of adenylate cyclase (AC) with forskolin partially reduced IBMX-induced alterations whereas protein kinase C (PKC) activation via phorbol myristate acetate (PMA) fully reduced IBMX-induced changes. Only small, but early and sustained, increases in membrane potential were observed following incubation with cell permeable PKA inhibitor myr-PKI 14-22. Taken together, these studies suggest A_{2B} appears to signal through a cAMP-dependent/PKA-independent, and a PKC-dependent pathway to support mitochondrial function in 661w and that IBMX functions as an inverse agonist at the A_{2B} receptor. The results have important implications for those interested in photoreceptor

neurodegeneration and highlight a previously uncharacterized action of IBMX at A_{2B} receptor.

6.2 Introduction

Adenosine signaling is an important regulator of myriad physiological functions, from wakefulness and metabolic regulation in the central nervous system (CNS) and heart, and from photoreceptor coupling (a tradeoff between resolution and sensitivity) in the retina to protecting against mitochondrial damage following ischemia/reperfusion injury in CNS, liver, kidney and heart [41-44, 129-133]. Adenosine and its biological derivatives bind to a number of extracellular G protein-coupled receptors (GPCRs) and ligand-gated ion channels split into three broad classes. The first major class of adenosine-binding GPCRs are deemed the P2X receptors, and are oligomeric ion channels activated by various phosphorylated purines and pyrimidines (e.g. adenosine di- and tri-phosphate [ADP, ATP], and uridine diphosphate [UDP] and UDP-glucose). P2Y receptors are the second major class of purine phosphate-binding receptors, and are GPCRs. The P1, or simply termed adenosine receptor class, is represented currently by four GPCRs, the A_1, A_{2A}, A_{2B}, and A_3 adenosine receptors [134-137]. Each receptor has varying specificity as to which G protein subunit(s) it couples to, and are involved in diverse intracellular signaling mechanisms within the cell (**Table 6-1**). As the xanthine derivative 3-isobutyl 1-methylxanthine (IBMX) has been previously described to inhibit the P1 or adenosine receptor subclass, and this subclass has been linked to the regulation of mitochondrial physiology, this report will focus its efforts on understanding the role of adenosine receptor signaling [138].

Receptor	Gene Symbol (human, mouse)	G Proteins
A_1	ADORA1, Adora1	$G\alpha_i$
A_{2A}	ADORA2A, Adora2a	$G\alpha_s$
A_{2B}	ADORA2B, Adora2b	$G\alpha_s$, $G\alpha_{q/11}$, $G\alpha_i$
A_3	ADORA3, Adora3	$G\alpha_i$

Table 6-1. Adenosine receptor family members and the G proteins to which they couple.

The work of several labs indicates the necessity of adenosine in activating the protective pathways involved in the phenomena of ischemic preconditioning and postconditioning. Briefly, preconditioning is the cytoprotective phenomenon observed following a series of short vascular occlusions made minutes to hours prior to a major occlusion of vascular supply. Postconditioning is a similar phenomenon, with the exception that the short vascular occlusions are made after reperfusion. Activation of the epsilon isoform of protein kinase C (PKCε) and the extracellular release of adenosine, bradykinin, and opioids along with an increase in reactive oxygen species (ROS) have been observed followed preconditioning [43]. PKC and the adenosine A_{2B} receptor have been shown to be necessary in rabbit heart postconditioning as non-selective activation of protein kinase C isoforms with phorbol myristate acetate (PMA) was demonstrated to be sufficient to recapitulate post-conditioning, which was subsequently lost with concomitant inhibition of adenosine receptor A_{2B} [42]. This suggests that the A_{2B} receptor is a downstream target of one or more protein kinase C isoforms. However, the coupling of adenosine A_{2B} receptor to $G\alpha_q$ (resulting in the receptor functioning upstream of PKC isoforms) cannot be excluded, as in the CNS cell line U373 MG (astrocytoma) activation of PKCε and δ isoforms was observed following administration of A_{2B} agonist NECA [139].

6.3 Materials and Methods

6.3.1 Cell Culture

661w photoreceptor cells were generously provided by Dr. M. Al-Ubaidi (University of Oklahoma) [18] and maintained under standard conditions using DMEM-HG media (Sigma-Aldrich #D-7777) supplemented with 10% fetal calf serum (FCS, Atlanta Biologicals #S11550) and GlutaMAX (Life Technologies #35050-061). For imaging studies, cells of passages 15-25 were cultured to 80% confluency before trypsinization and seeded at a cell density of 8,900 cells per well in 96 well plates (Nunc Edge Plate, Thermo Scientific #167314) supplemented with 5% FCS and edge reservoirs filled with 1x phosphate buffered saline, (PBS, Life Technologies #14080-055) and grown for 24 h. For studies involving collection of cellular lysates, 661w cells were seeded at 200k per dish in 10 cm dishes in DMEM-HG supplemented with 5% FCS, and grown for 72 h. 24 h prior to assay, cells were at 80% confluency, and were washed in PBS, followed by change of media to DMEM with 5.5 mM glucose without phenol red (Sigma-Aldrich #D-5030) supplemented with 1% FCS to induce cell cycle arrest. Cells were used for experiments 24 h after this switch to normal glucose and 1% FCS-containing media, with treatments for either 24 h (morphological analysis) or 1 h (membrane potential analysis). All compounds used for treatment were from Sigma-Aldrich (St. Louis, MO) unless otherwise specified, and were prepared at 1000x concentration in DMSO before administration to cells (final [DMSO] = 0.1%).

6.3.2 Genome-wide Microarray Expression Profiling

mRNA was isolated from 661w cells grown in 10 cm dishes to confluence and purified using the RNeasy RNA purification kit (Qiagen, Valencia, CA). cDNA was synthesized from high-quality RNA ($A_{260/280} \geq 1.80$) and subjected to microarray analysis using conditions identical to those described previously [116]. Briefly, GeneChip Mouse Genome 430 2.0 oligonucleotide arrays (Affymetrix) were hybridized with equal amounts

of labeled cRNA (15 μg/array) and readout was performed by the DNA Microarray Core Facility at the Medical University of South Carolina using the Affymetrix Fluidics Station.

6.3.3 Western Blotting

Antibody for the adenosine A_{2B} receptor was obtained from Fisher Scientific (#PIPA518422, goat polyclonal). GAPDH antibody was obtained from Fitzgerald (10R-G109a, mouse monoclonal). 661w cells grown to confluence on 10 cm dishes were lysed in 1% sodium dodecyl sulfate with 6M urea in phosphate buffered saline at pH 7.4. The lysates were loaded as typical using Pierce loading buffer at 25% and beta mercaptoethanol at 10%, with the exception that these samples were kept at room temperature, not boiled, for 30 min. Gels were run at 100V for 25 min, followed by 200V for 1 hr. Proteins were transferred to iBlot nitrocellulose membrane using program 3 for 8 minutes. Membranes were blocked with 2.5% bovine serum albumin (fraction V fatty acid free, Fisher Scientific) in tris-buffered saline/tween 1% (TBS-Tween) at room temperature for 1 h and antibody stocks made in 0.5% bovine serum albumin in TBS-Tween at the manufacturer's suggested concentration of 1000 x. Incubation with primary antibody was for 18 h at 4 deg. C and secondary antibody (horseradish peroxidase (HRP)-conjugated donkey anti-goat (Fitzgerald #43R-ID040hrp) or HRP-conjugated rabbit anti-mouse (Fitzgerald #43R-1418) for 2 h at room temperature with 3x washes in TBS-Tween at each change. Membranes were developed using SuperSignal West Dura development substrate (Fisher PI-34076) and imaged.

6.3.4 High Content Determination of Mitochondrial Morphology and Membrane Potential

To evaluate the concentration- and time-dependence of IBMX-induced mitochondrial changes, the method of Leonard et al. [114] was used. Briefly, 661w cells

were seeded into Nunc Edge 96-well plates (Fisher) at a density of 8900/well and incubated in DMEM-HG (Invitrogen) for 24 h. Media was changed to DMEM supplemented with 1% FCS and incubated overnight before staining. 661w cells were loaded with 50 nM MitoTracker Deep Red, and 10 µM Hoechst 33342 for 30 min and then washed followed by a 3 h incubation at 37 °C in DMEM-HG supplemented with 1% FCS. After 3 h, cells were treated with IBMX at the indicated concentrations and cells imaged. Imaging was performed on a GE INCell Analyzer 2000 automated wide-field fluorescence microscope using a 40x Nikon ELWD objective (NA 0.6) matched with the large-format 2048x2048 pixel 12-bit Coolsnap K4 camera. Images were saved in the TIFF image file format and subjected to the high content mitochondrial morphological analysis as described in Section 3.

6.3.5 Seahorse XF96 Respirometry

661w photoreceptor cells were seeded (6,000 cells/well) into XF96 polystyrene plates (Seahorse Biosciences, Billerica, MA) and incubated for 48 h in DMEM-HG (Sigma-Aldrich) supplemented with 5% FCS. Media was then changed for DMEM supplemented with 5.5 mM glucose and 1% FCS and vehicle or toxicant treatments administered for 24 h. Just prior to time of assay, media was switched to bicarbonate-ion free RS (reduced serum) buffer at pH 7.4 prepared with 130 mM NaCl, 5.33 mM KCl, 1.8 mM $CaCl_2$, 0.6 mM $MgCl_2$, 0.5 mM KH_2PO_4, 0.5 mM $NaPO_4 \cdot (H_2O)_7$, insulin, 5.5 mM glucose, and supplemented with 1% FCS, 1 mM L-alanyl-L-glutamine (GlutaMAX), 2 mM glutamine, 1% MEM Vitamins, 1% MEM Amino Acids, 1% MEM Non-Essential Amino Acids, 1% Penicillin/Streptomycin. All inorganic salts used were obtained from Sigma-Aldrich (St. Louis, MO) and organic supplements obtained from GIBCO/Life Technologies (Grand Island, NY) unless otherwise noted. All oxygen consumption rate (OCR) measurements used cycle times of 4 minutes per mix (probes moving) and 3

minutes per measure (probes down). After recording 3 baseline OCR measurements, oligomycin (100 nM) was administered and 3 additional OCR measurements obtained. This was followed by administration of FCCP (carbonyl cyanide-p-trifluoromethoxyphenylhydrazone) (1 µM) and two OCR measurements obtained. Finally, a combination of rotenone (5 µM) and antimycin A (100 nM) was administered and two final OCR measurements obtained. Uncoupled OCR's for each condition were recorded and reported as mean +/- standard error of the mean (s.e.m.) across experiments. As the sequence of mitochondrial perturbing agents above includes non-reversible pharmacology, each time point was performed on a separate plate.

6.3.6 Statistical Analysis

Statistical analysis was conducted using either one-way ANOVA or two-way ANVOA, respectively, for single time-point (>2 concentrations/treatments) or multiple time-point and multiple concentration experiments. Holm-Sidak multiplicity-adjusted post-hoc analyses were conducted in each analysis to compare across treatment groups (not timepoints) and p values < 0.05 were considered significant.

6.4 Results

6.4.1 Expression of Adenosine Receptor Subtypes in 661w

As the adenosine receptor subtypes display significant heterogeneity with regards to phenotypic regulation and secondary messenger coupling, genome-wide expression profiling, Western blotting, and cyclic nucleotide accumulation determination by enzyme-linked immunosorbance assay were conducted to determine which subtypes are expressed in the 661w photoreceptor cell line. These efforts demonstrated that at the mRNA level, only the adenosine receptor A_{2B} subtype was expressed (**Figure 6-1A**). Expression of A_{2B} was then confirmed at the protein level by Western blotting (**Figure**

6-1B). Functional activity of A_{2B} was confirmed by measuring an ~15-fold increase in

cAMP following 20 min stimulation with A_{2B}-selective agonist BAY60-6583 (**Figure**

6-1C).
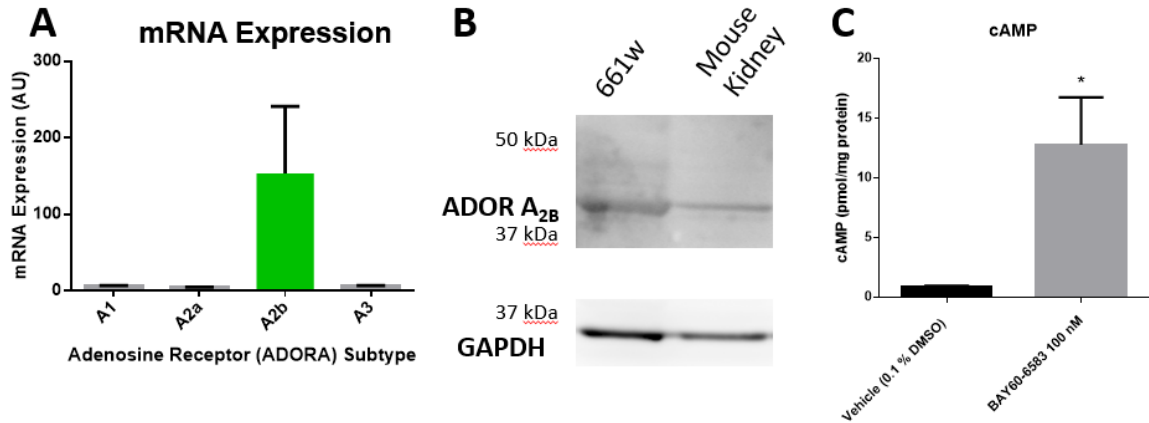
Figure 6-1. Functional Expression of Adenosine A_{2B} Receptor Expression in 661w.

RNA isolated from 661w was reverse transcribed to cDNA and subjected to genome-wide expression profiling by hybridization to Affymetrix GeneChip mouse microarray (A). Data shown are mean ± s.e.m. of n=3 experiments. Expression of A_{2B} receptor by Western blotting (B). cAMP concentrations were determined by EIA following 20 min incubation with A_{2B}-selective agonist BAY60-6583 or vehicle (0.1% DMSO).

6.4.2 Adenosine A_{2B} Receptor Agonism Fails to Recapitulate IBMX-induced Mitochondrial Physiological Changes

Having demonstrated functional expression of the A_{2B} receptor in the 661w

retina-derived cell line, mitochondrial physiological response was next examined

following administration of 3-isobutyl 1-methylxanthine (IBMX) or a selective agonist of

the adenosine A_{2B} receptor, BAY60-6583 (EC_{50} for A_{2B}: 2.8 nM). IBMX increased

mitochondrial membrane potential ($\Delta\Psi_m$) (**Figure 6-2A**), increased mitochondrial fusion

as evidenced by significant increases in the proportion of networks (in comparison to the

less interconnected punctate, rod, and large & round phenotypes) (**Figure 6-2B**), and

decreased mitochondrial respiratory capacity (current) as evidenced by a decrease in

uncoupled respiration (**Figure 6-2C**). In comparison to IBMX, BAY60-6583 failed to

recapitulate any of these changes, instead inducing a small magnitude effect in the

opposite direction by decreasing mitochondrial networks by up to 12% after 12 - 24 h

exposure at 10 and 100 nM (**Figure 6-2B**).
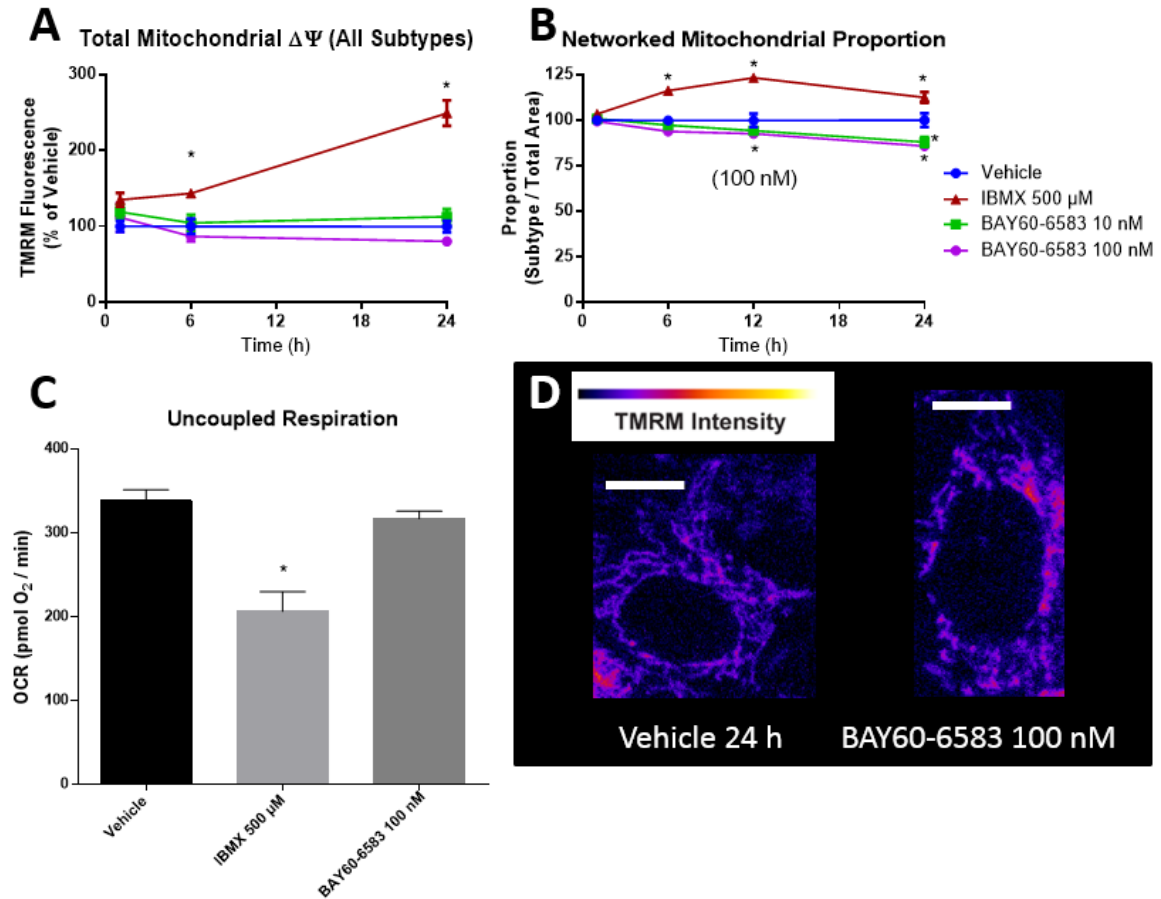
Figure 6-2. A$_{2B}$-selective Agonist BAY60-6583 Fails to Recapitulate IBMX-induced Mitochondrial Physiological Changes.

661w photoreceptor cell line mitochondria were subjected to morphological and membrane potential analysis as previously described [114]. Mitochondrial membrane potential is presented in (A), proportion of networked mitochondria in (B), uncoupled respiration in parallel experiments at 24 h in (C), and representative images in (D). Data shown are mean s.e.m. of n=6 experiments. *multiplicity-adjusted $p<0.05$. Analyzed by one-way (C) or two-way ANOVA (A & B), post-test treatment group versus vehicle at each time point. Scale bar 10 μm (D).

6.4.3 Adenosine A$_{2B}$ Receptor Antagonism Fails to Recapitulate IBMX-induced Mitochondrial Physiological Changes

Following studies with the A$_{2B}$ receptor agonist BAY60-6583, the effect of A$_{2B}$

antagonist PSB-603 (K$_i$ for A$_{2B}$: 0.55 nM) on mitochondrial physiology was next

examined. No significant changes in mitochondrial physiology were observed following

administration of 10-100 nM PSB-603 (**Figure 6-3**).
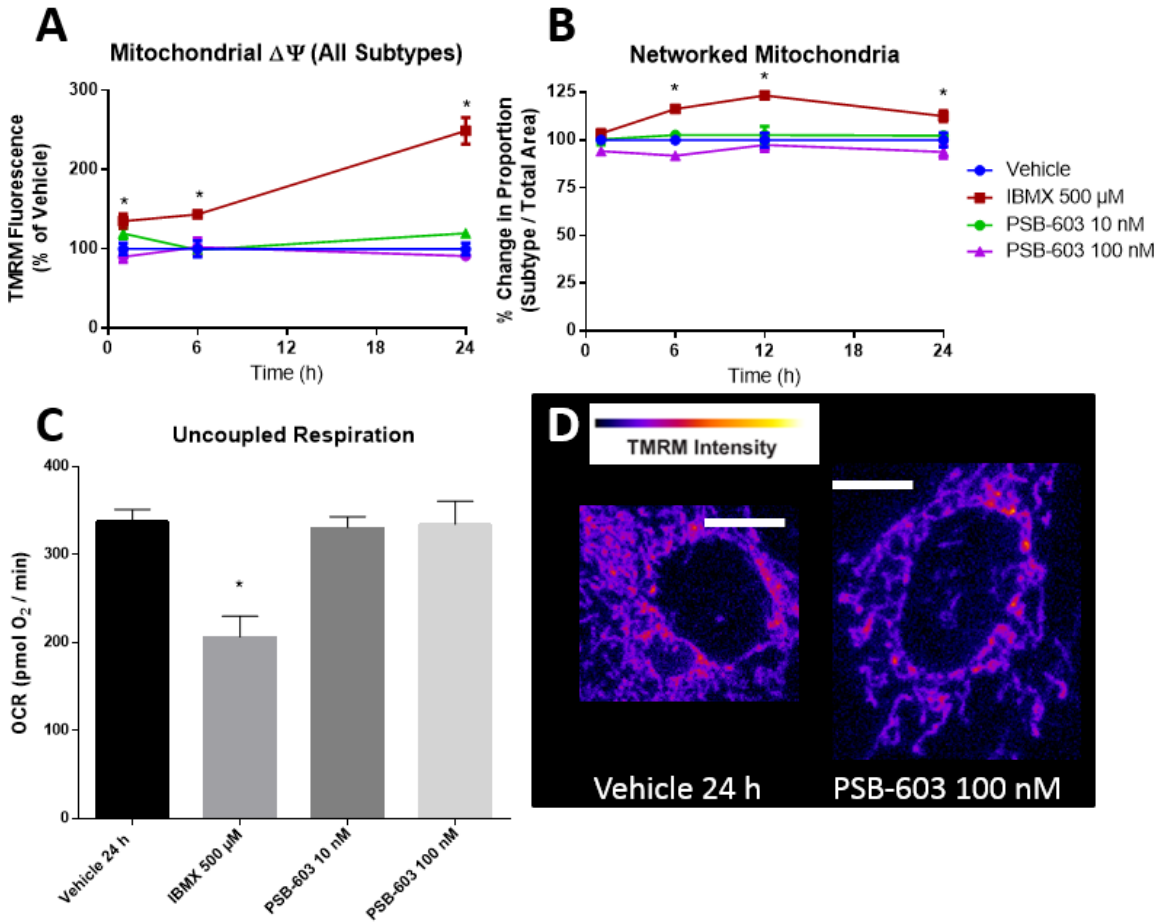
Figure 6-3. A2B-selective Antagonist PSB-603 Fails to Recapitulate IBMX-induced Mitochondrial Physiological Changes

661w photoreceptor cell line mitochondria were subjected to morphological and membrane potential analysis as previously described [114]. Mitochondrial membrane potential is presented in (A), proportion of networked mitochondria in (B), uncoupled respiration in parallel experiments at 24 h in (C), and representative images in (D). Data shown are mean s.e.m. of n=6 experiments. *multiplicity-adjusted $p<0.05$. Analyzed by one-way (C) or two-way ANOVA (A & B), post-test treatment group versus vehicle at each time point. Scale bar 10 µm (D).

6.4.4 Adenosine A_{2B} Receptor Inverse Agonism Induces Increased Mitochondrial Membrane Potential and Decreased Respiration
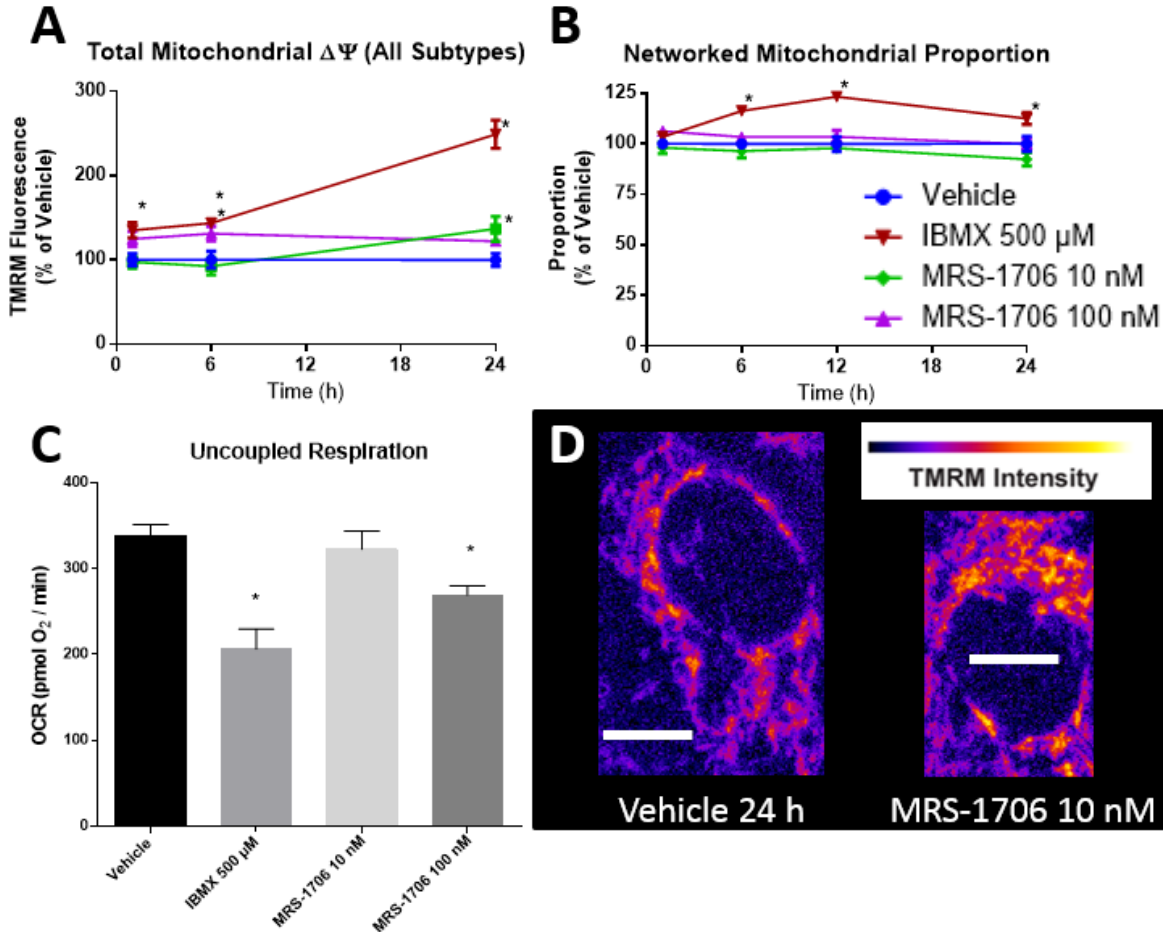
Figure 6-4. A_{2B}-selective Inverse Agonist MRS-1706 Recapitulates IBMX-induced Mitochondrial Membrane Hyperpolarization and Decreased Respiration

661w photoreceptor cell line mitochondria were subjected to morphological and membrane potential analysis as previously described [114]. Mitochondrial membrane potential is presented in (A), proportion of networked mitochondria in (B), uncoupled respiration in parallel experiments at 24 h in (C), and representative images in (D). Data shown are mean s.e.m. of n=6 experiments. *multiplicity-adjusted $p<0.05$. Analyzed by one-way (C) or two-way ANOVA (A & B), post-test treatment group versus vehicle at each time point. Scale bar 10 µm (D).

Following studies with the A_{2B} receptor agonist BAY60-6583, the effect of A_{2B} inverse agonist MRS-1706 (K_i for A_{2B}: 1.39 nM) on mitochondrial physiology was next examined. MRS-1706 recapitulated two out of three physiological effects induced by IBMX. At 10 nM, MRS-1706 recapitulated IBMX-induced hyperpolarization at 6 h (130% v. 140% of control TMRM intensity) but this effect was transient and not observed at 24

86

h (**Figure 6-4A**). No alterations in morphology or uncoupled respiration were observed at any time point. At a 100 nM concentration, no significant changes in morphology were observed (**Figure 6-4B**), but ~50% of the IBMX-induced decrease in respiration was recapitulated (85% v. 62% of control values) and a small amount of hyperpolarization was observed (130% vs. 250%) (**Figure 6-4A,B,C**).

6.4.5   IBMX Functions as an Inverse Agonist at the Adenosine A_{2B} Receptor
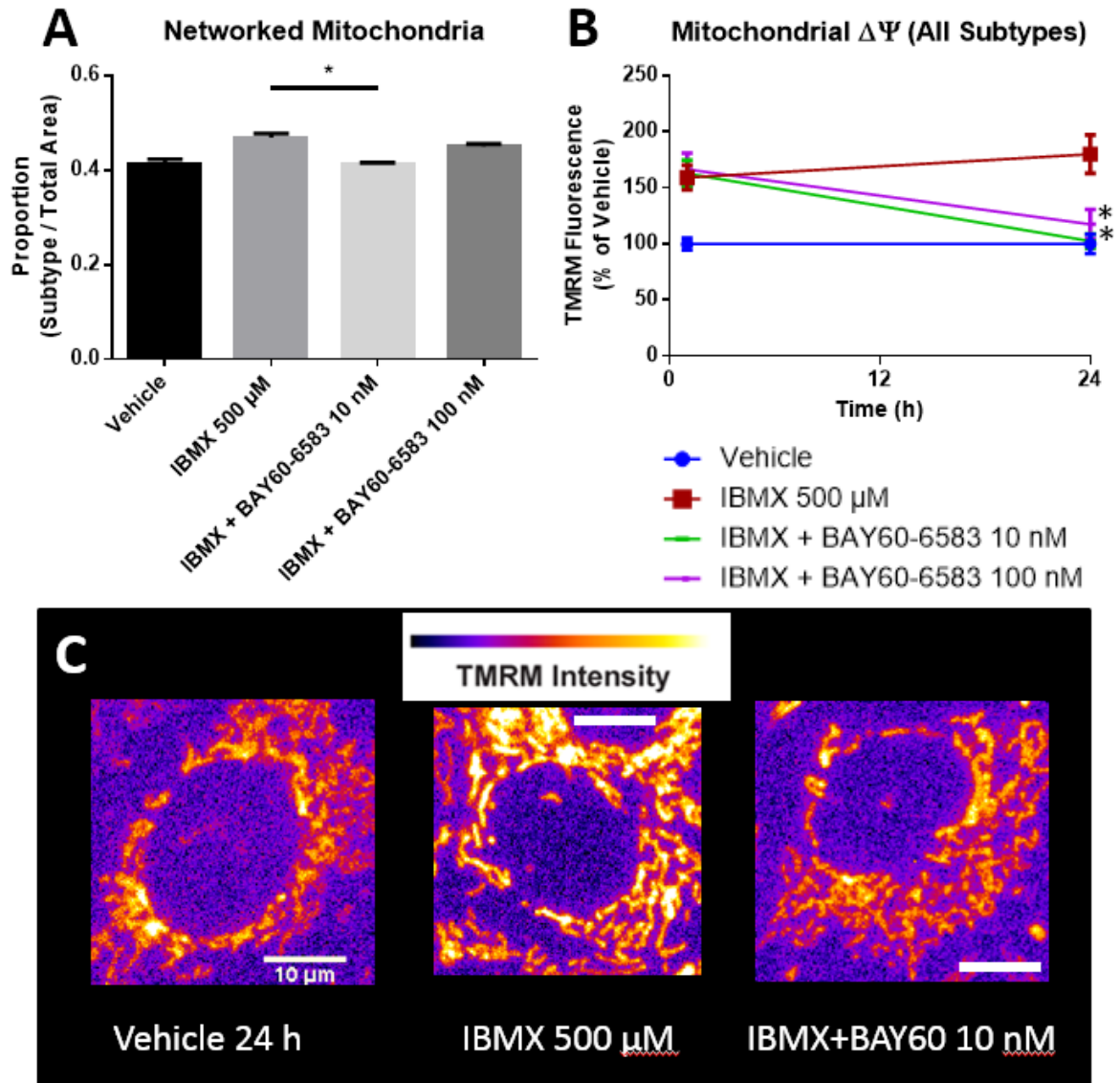
Figure 6-5. A_{2B} agonist BAY60-6583 reduces latent IBMX-induced physiological changes.

661w photoreceptor cell line mitochondria were subjected to morphological and membrane potential analysis as previously described [114]. Proportion of networked mitochondria at 24 h is presented in (A), mitochondrial membrane potential in (B), and representative images in (C). Data shown are mean s.e.m. of n=5 experiments. *multiplicity-adjusted $p < 0.05$. Analyzed by one-way (A) or two-way ANOVA (B), post-test treatment group versus IBMX at each time point. Scale bar 10 μm (C).

As IBMX's pharmacology has not been previously characterized at the adenosine

A_{2B} receptor and the antagonist PSB-603 had no effect, the hypothesis that IBMX may

be functioning as an inverse agonist was next tested using competition. In these

studies, 1 h incubation with adenosine A_{2B} receptor agonist BAY60-6583 or adenosine A_{2B} receptor antagonist PSB-603 was conducted prior to administration with IBMX, and the effects measured at 1 h and 24 h following IBMX administration.

At 1 h, no differences were noted between the IBMX treatment group and the cells given PSB-603 or BAY60-6583. However, the long-term effects of IBMX (at 24 h) on networked morphology and membrane potential were competed away by A_{2B} agonist BAY60-6583 (**Figure 6-5**). The same phenomenon was observed with PSB-603, suggesting that latent, but not immediate changes in mitochondrial physiology may occur through IBMX's action as an inverse agonist (**Figure 6-6**).
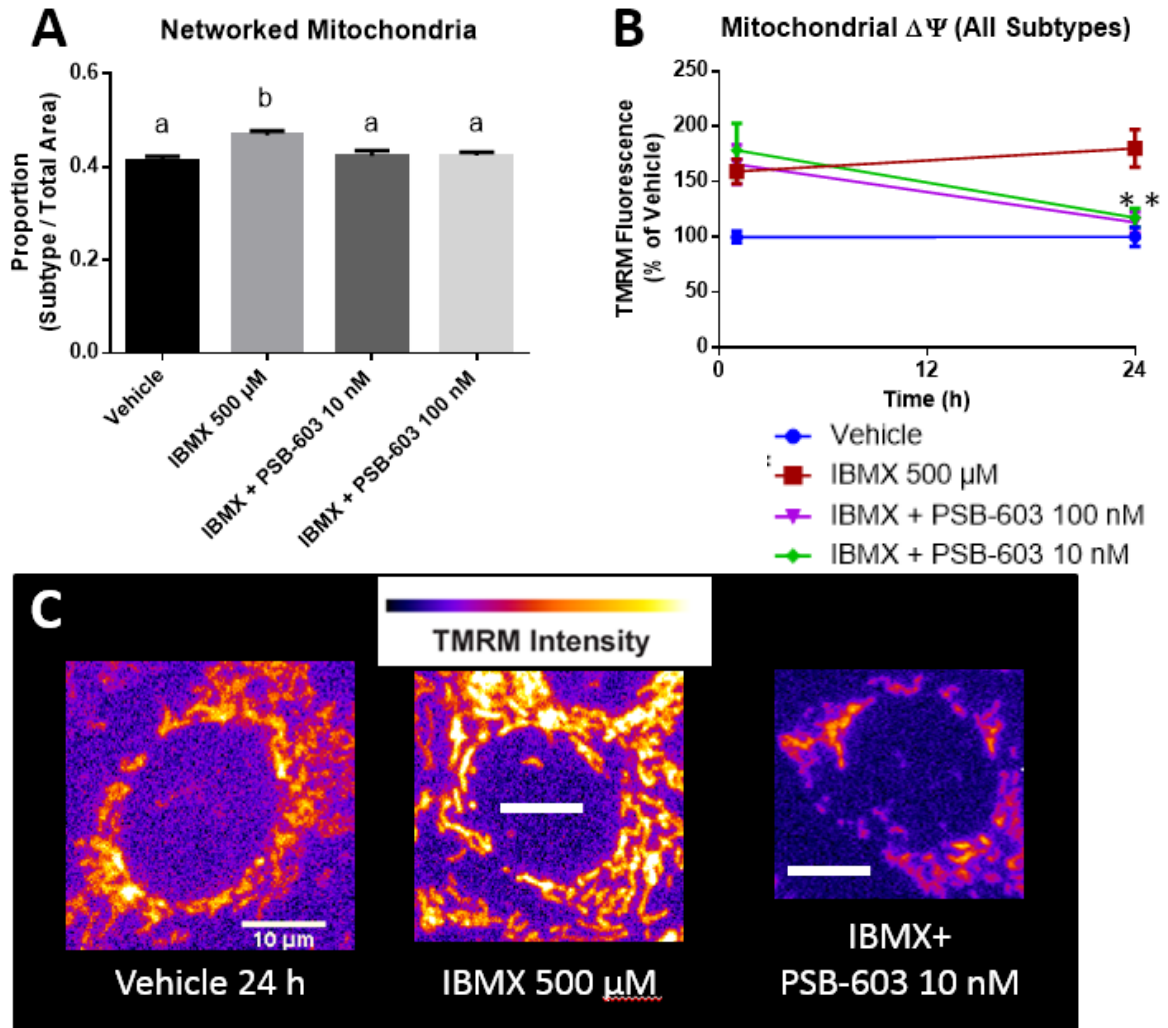
Figure 6-6. A₂ᵦ antagonist PSB-603 reduces latent IBMX-induced physiological changes.

661w photoreceptor cell line mitochondria were subjected to morphological and membrane potential analysis as previously described [114]. Proportion of networked mitochondria at 24 h is presented in (A), mitochondrial membrane potential in (B), and representative images in (C). Data shown are mean s.e.m. of n=5 experiments. *multiplicity-adjusted $p < 0.05$. Analyzed by one-way (A) or two-way ANOVA (B), post-test treatment group versus IBMX at each time point. Scale bar 10 µm (C).

A Networked Mitochondria

B Mitochondrial ΔΨ (All Subtypes)

Time (h)	IBMX+Fsk 100 nM	1 µM	10 µM
1			
24	X	X	X

C Uncoupled Respiration

- Vehicle
- IBMX 500 µM
- IBMX + Forskolin 100 nM
- IBMX + Forskolin 1 µM
- IBMX + Forskolin 10 µM

D TMRM Intensity

Vehicle 24 h | IBMX 500 µM | IBMX 500 µM + Forskolin 100 nM

Figure 6-7. Forskolin abrogates most IBMX-induced mitochondrial physiological changes.

661w photoreceptor cell line mitochondria were subjected to morphological and membrane potential analysis as previously described [114]. Proportion of networked mitochondria at 24 h is presented in (A), mitochondrial membrane potential in (B), uncoupled respiration in parallel experiments at 24 h in (C), and representative images in (D). Data shown are mean s.e.m. of n=3-6 experiments. Different letters (A, C) or X in (B) denote multiplicity-adjusted $p<0.05$ v. IBMX. Analyzed by one-way (C) or two-way ANOVA (A & B). Scale bar 10 µm (D).

6.4.6 Adenosine A_{2B} Receptor Coupling to $G\alpha_s$–Adenylate Cyclase is Responsible for Regulation of Mitochondrial Physiology

As the adenosine A_{2B} receptor has been reported to couple to multiple G protein alpha subunits depending on cell type, the importance of coupling of this receptor to the $G\alpha_s$ subunit in 661w was first examined. Forskolin, an activator of adenylate cyclase, was preincubated with cells 1 h before administration of IBMX and the response of cellular mitochondria recorded. At 1 h, no significant differences between forskolin and forskolin + IBMX were observed, but a small trend towards restoration of mitochondrial membrane potential was observed. However, it was observed that alterations in networked morphology and mitochondrial membrane potential were completely restored at 24 h along with a partial (~50%) reversal of decreases in uncoupled respiration. These data indicate that latent but not immediate IBMX-induced mitochondrial physiological alterations are likely transduced via inactivation of adenylate cyclase.

To further elucidate the mechanism of altered mitochondrial physiology via $G\alpha_s$-adenylate cyclase-coupled signaling, the effects of PKA inactivation via the myristoylated PKI amide inhibitory peptide 14-22 (myr-PKI, PKA K_i=36 nM) were next examined. These studies demonstrate that loss of PKA signaling in 661w has no effect on networked morphology nor uncoupled respiration (**Figure 6-8A,C**); however, a small but rapid and sustained increase in mitochondrial membrane potential is elicited (~120-125% of control values) (**Figure 6-8B**) with 10 µM myr-PKI 14-22 administration. Compared to IBMX, the magnitude of this change was much smaller, indicating that loss of PKA activation by cAMP elicited from adenylate cyclase likely accounts only for a small portion of altered signaling induced by IBMX administration, or that IBMX inactivation of cAMP selective phosphodiesterases balances the inactivation of A_{2B}-adenylate cyclase-PKA signaling.
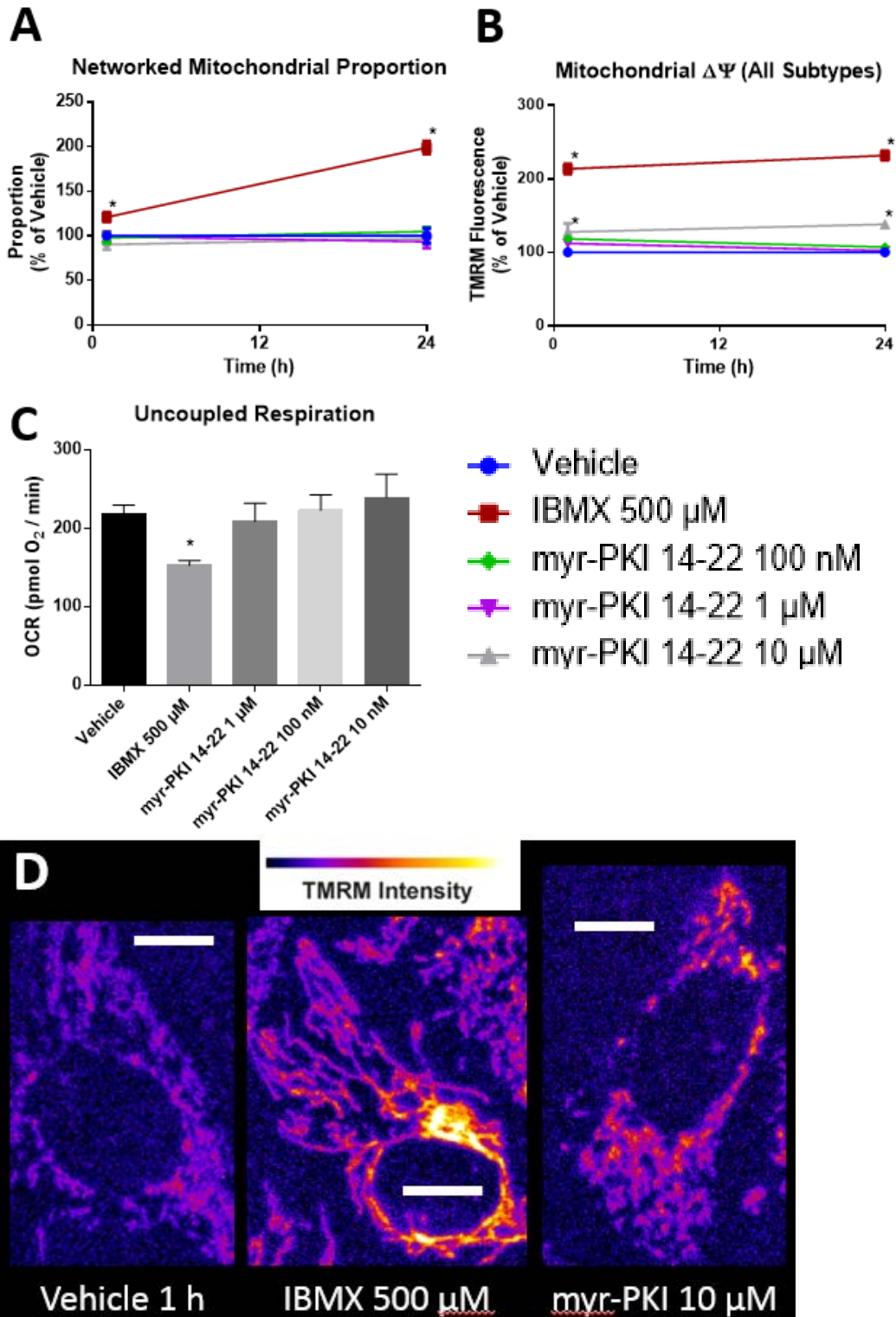
Figure 6-8. PKA inhibition recapitulates IBMX-induced mitochondrial membrane hyperpolarization.

661w photoreceptor cell line mitochondria were subjected to morphological and membrane potential analysis as previously described [114]. Proportion of networked mitochondria at 24 h is presented in (A), mitochondrial membrane potential in (B), uncoupled respiration in parallel experiments at 24 h in (C), and representative images in (D). Data shown are mean s.e.m. of n=5 experiments. *multiplicity-adjusted $p < 0.05$ v. vehicle. Analyzed by one-way (C) or two-way ANOVA (A & B). Scale bar 10 µm (D).

6.4.7 Role of A$_{2B}$-Gα$_{q/11}$-PKC Coupling in Regulation of Mitochondrial Physiology

As alterations in A$_{2B}$-Gα$_s$-coupled signaling explained only a portion of the mitochondrial physiological changes observed, it was hypothesized that a significant portion of alterations induced by inverse agonism at the receptor may be conducted by other G protein coupled pathways. Canonical Gα$_q$ and Gα$_{11}$-coupled signaling occur via activation of a plasma-membrane bound phospholipase C beta (PLC-β), which leads to cleavage of phosphatidylinositol 4,5-bisphosphate (PIP$_2$) into inositol triphosphate (IP$_3$) and diacylglycerol (DAG) [140]. Soluble IP$_3$ may travel to the endoplasmic reticulum and activate store-operated Ca^{2+} release, increasing cytoplasmic concentrations of Ca^{2+}. Together with DAG, Ca^{2+} leads to the activation of one or more isoforms of protein kinase C (PKC). However, intracellular Ca^{2+} does not change following IBMX administration, nor is a plasma membrane current induced by IBMX administration (**Supplementary Figure 11**). Additionally, cyclic nucleotide-gated cation channels (CNGs) are not expressed in 661w (genome-wide expression profiling in these studies and [22]). Studies have demonstrated that several isoforms of PKC signal in a Ca^{2+}-independent manner [141, 142], demonstrating that even in the absence of increases in the rise of cytoplasmic Ca^{2+}, PKC signaling may be invoked.

Using genome-wide expression profiling, the presence of Gα$_q$, Gα$_{11}$, but neither Gα$_{14}$ nor Gα$_{15}$ transcripts were found to be expressed. Additionally, phospholipase C beta (PLC-β) isoforms 1 and 3, but not 2 were expressed (**Section 6.3.2**). As either PLC- β1 or 3 isoforms are capable of coupling to Gα$_q$/Gα$_{11}$ and cleaving PIP$_2$ into IP$_3$ and DAG ultimately leading to PKC activation [140], the expression levels of PKC isoforms in 661w cell line were next examined (**Table 6-2**).

Isozyme	Requires Ca^{2+}	Requires DAG	Expression	EC_{50} PMA (nM)
alpha	X	X	Present	112±18 [142]
delta		X	Present	574±37 [142]
epsilon		X	Present	15-37 [143]
eta		X	Marginal	0.1±.01 [142]
iota			Present	ND
PKN1			Present	ND
PKN2			Present	ND
PKN3			Present	ND

Table 6-2. Protein Kinase C Isoforms Expressed in 661w.

Expression as determined by genome-wide profiling. See **Section 6.3.2** for experimental details.

Having established the expression of all members of the pathway necessary for PKC activation, the role of all PKC isoforms was next examined by incubating 661w cells with classical and novel-PKC isoform activator phorbol 12-myristate 13-acetate (PMA) prior to IBMX administration (**Figure 6-9**). Although only a trend for reversal of membrane hyperpolarization is displayed with 10 nM PMA pretreatment, followed by 1 h incubation with IBMX, at 24 h, complete reversal of IBMX-induced changes in networked morphology, respiratory capacity, and membrane potential were observed. Unexpectedly, concentrations of PMA greater than 10 nM resulted in a partial loss of this effect in respirometric studies (**Figure 6-9C**). These studies suggest A_{2B} receptor coupling to $G\alpha_{q/11}$ upstream of PKC is responsible for latent, but not early alterations in mitochondrial physiology, or that one or more isoforms of PKC modulate downstream effects of A_{2B}-$G\alpha_s$ signaling.

Time (h)	IBMX+PMA 10 nM	100 nM
1		
24	X	X

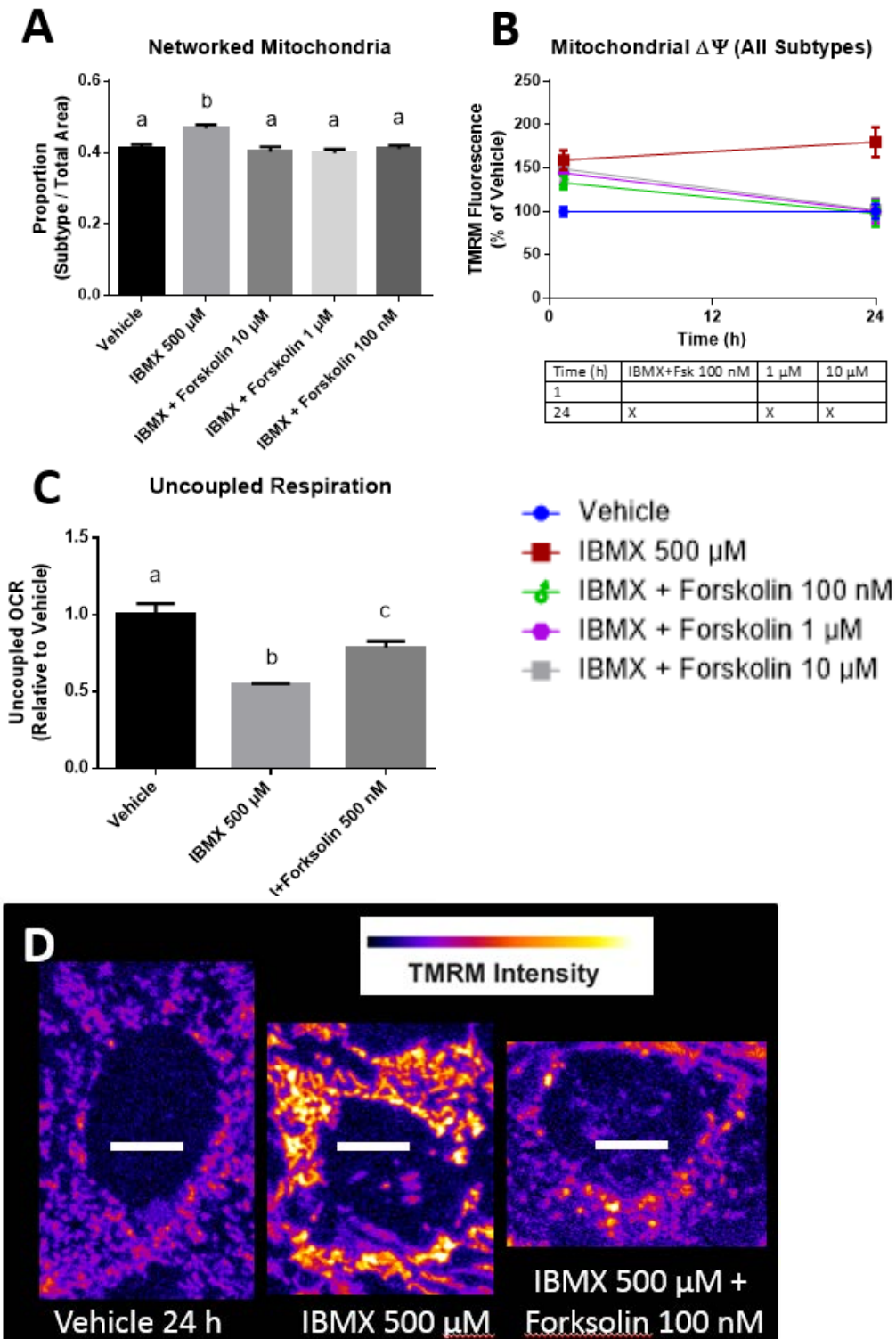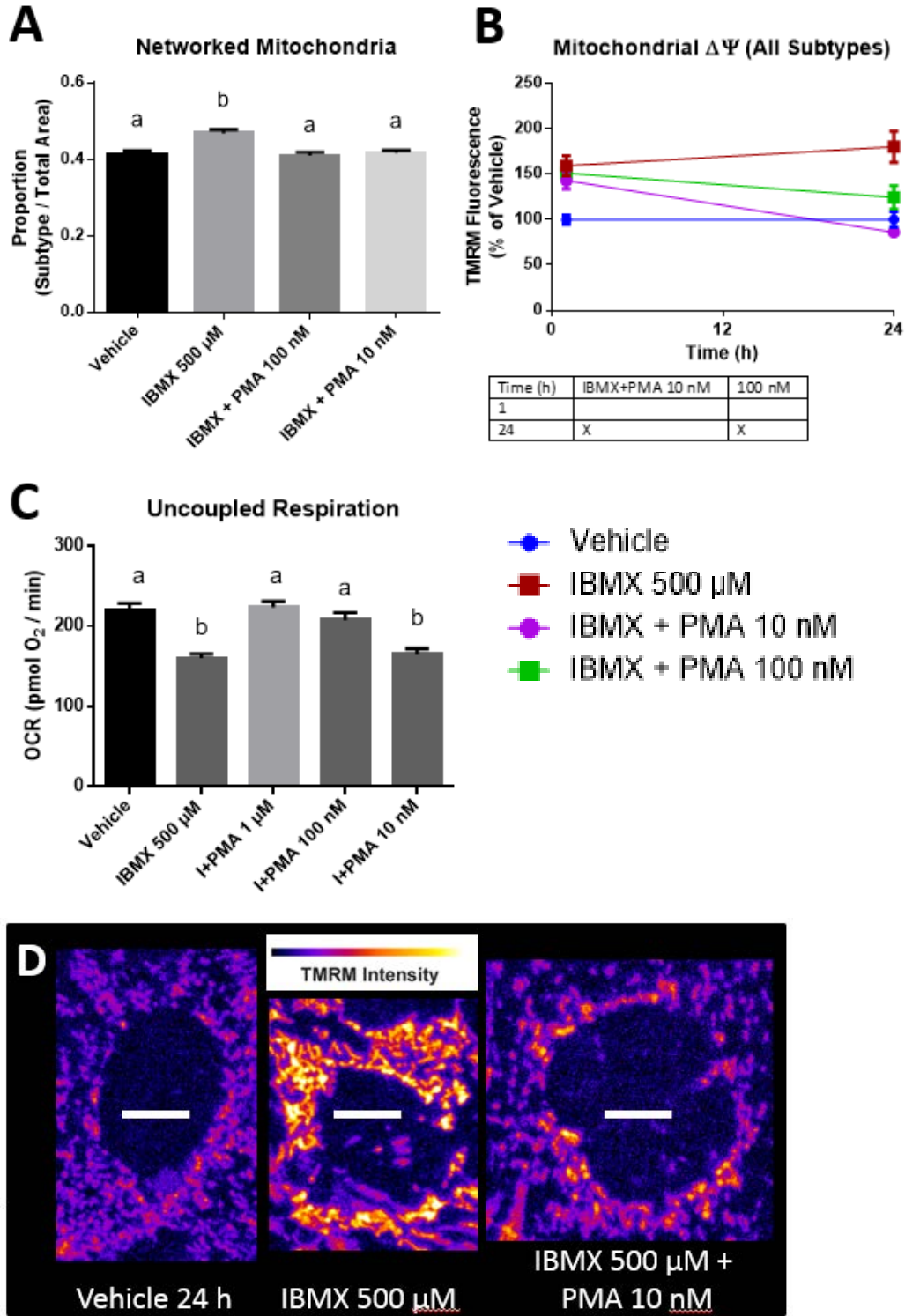**Figure 6-9. Activation of PKC reverses latent IBMX-induced mitochondrial physiological changes.**

661w photoreceptor cell line mitochondria were subjected to morphological and membrane potential analysis as previously described [114]. Proportion of mitochondria displaying networked morphology is presented in (A), mitochondrial membrane potential in (B), uncoupled respiration in parallel experiments at 24 h in (C), and representative images in (D). Data shown are mean s.e.m. of n=6-9 experiments. Different letters (A, C) or X (B) denote $p < 0.05$ v. IBMX. Analyzed by one-way (A, C) or two-way ANOVA (B). Scale bar 10 µm (D).

6.5 Discussion

These studies demonstrate for the first time that IBMX functions as an inverse agonist at the adenosine A_{2B} receptor, and that stimulation of both $G\alpha_s$– and $G\alpha_{q/11}$–mediated pathways in 661w cells reverse IBMX-alterations in mitochondrial physiology. As inverse agonism but neither antagonism nor agonism led to these changes, it is likely that constitutive activity of the A_{2B} receptor is necessary for maintenance of mitochondrial physiology in 661w. Interestingly, in combination studies, IBMX's effect on mitochondrial physiology were abrogated only at 24 h but not at 1 h, suggesting that loss of A_{2B} receptor signaling requires a slower mechanism than protein-protein interaction or post-translational modifications to induce a hyperpolarized and fused state. Examples of such a mechanism include transcriptional regulation, protein turnover, mitochondrial turnover, or another pathway with slower kinetics. Previous work in the lab has shown that inhibition of cyclic guanosine monophosphate (cGMP)-selective phosphodiesterase enzymes play a role in the immediate (1 h) effects (**Section 4**). Thus, the primary focus of the remaining discussion centers on these longer-term effects.

Loss of PKA signaling appears to play a limited role in this latent regulation of mitochondrial physiology, regulating only membrane potential (**Figure 6-8B**). However, A_{2B} coupling to $G\alpha_s$-adenylate cyclase appears to regulate latent alterations in morphology and membrane potential to a larger degree, with a partial (50%) regulation of decreases in mitochondrial uncoupled respiration (**Figure 6-7**). These results suggest a cAMP-dependent but PKA-independent pathway of regulation, perhaps through PI3K or MAPK and subsequent regulation of transcription [144]. However, these results are unexpected given IBMX has also been shown to increase cAMP (**Figure 5-1** in **Section 5**). This highlights the possibility that although total intracellular cAMP concentrations rise due to IBMX's dual nature as a cyclic nucleotide phosphodiesterase inhibitor

97

(**Section 5.4.1**), local cAMP concentrations near A_{2B}-$G\alpha_s$ may decrease following administration of IBMX, or the initial increase in cAMP is followed by global decreases. Further experiments using a FRET-based cAMP biosensor would be informative in understanding the role of subcellular cAMP localization in IBMX-induced mitochondrial changes [145].

While other known mechanisms of GPCR signaling remain possible, such as internalization, arrestin-dependent signaling, or $G\alpha_i$ and $G_{\beta/\gamma}$ signaling, any unevaluated pathways are likely to converge on PKC to induce effects on mitochondrial physiology as restoration of PKC signaling during IBMX treatment completely rescued normal mitochondrial physiology at 24 h (**Figure 6-9**). However, the question remains of which PKC isoform is responsible for these altered changes. This Ca^{2+} independence suggests that a "novel" or "atypical"[1] isoform of PKC is responsible for the alterations observed in mitochondrial physiology, seven of which are expressed in 661w (**Table 6-2**). By virtue of each isoform's differential affinity for PMA and in the context of no calcium mobilization with IBMX administration (**Supplementary Figure 11**), it is tempting to suggest that at higher concentrations of PMA (100 nM to 1 μM), activation of the lower affinity delta isoform (PKCδ) is responsible for the abrogation of protective effect on respiration modulated by activation of the higher affinity epsilon (PKCε) or eta (PKCη) isoforms by PMA (**Figure 6-9C**).

Taken together with previous results from this lab demonstrating that inhibition of cGMP-specific cyclic nucleotide phosphodiesterases (PDEs) recapitulates some of the altered mitochondrial physiological changes, namely increased mitochondrial membrane potential and network morphology, with partial decreases in respiratory capacity

---

[1] "Novel" PKC isoforms require DAG but not Ca^{2+}, whereas "atypical" isoforms require neither DAG nor Ca^{2+}

(**Section 5**), it is reasonable to suggest that cGMP PDE inhibition ultimately results in altered PKC/adenosine A_{2B} receptor signaling. One explanation for an interplay between PDE and adenosine signaling is activation of cGMP-dependent protein kinases (PKG). PKG Type I and PKG Type II are expressed in 661w cells as determined by genome-wide expression profiling. PKG activation has been reported to be followed by opening of the mitochondrial K_{ATP} channel, ultimately resulting in the activation of PKC [146, 147]. A hypothesis that would explain the necessity for inverse agonism and rescue of mitochondrial physiological alterations by restoration of $G\alpha_{q/11}$ or $G\alpha_s$ is difficult, especially considering that in many non-retina model systems cGMP signaling is protective of mitochondria [36, 147]. However, cGMP-mediated switching of a positive feedback mechanism between A_{2B} and one or more isoforms of PKC is attractive—as the delta and epsilon isoforms of PKC have been shown to have opposing effects on mitochondrial physiology, with delta promoting and epsilon inhibiting pyruvate dehydrogenase [148]. Evidence in support of PKC signaling upstream of A_{2B} is manifest in that the cardioprotection against ischemia observed by mimicking ischemic post-conditioning with administration of PKC agonist phorbol myristate acetate was abrogated upon prior administration of A_{2B} antagonist MRS-1754 [146]. The precise mechanism of this sensitization of A_{2B} by PKC, although reproducible, remains unknown.

An important question remaining is characterization of the remaining members in the pathway by which IBMX-induced loss of A_{2B}-PKC or A_{2B}-cAMP mediated signaling alters mitochondrial physiology. Previous results indicated that GSK-3β, a constitutively active kinase inactivated by phosphorylation, was activated following IBMX administration (**Section 4.4**). As GSK-3β is reported to be downstream of PKA, PKC, and PKG, it may serve as the ultimate regulator of mitochondrial physiology following IBMX administration. Quite interestingly, A_{2B} has been reported to localize to

mitochondria in rat cardiomyocytes [149]. The subcellular localization of A_{2B} would be expected to be important for signaling, as recent evidence suggests cytosolic and mitochondrial pools of cAMP remain functionally distinct, with mitochondrial cAMP generation mediated by soluble adenylate cyclase (sAC) and turnover mediated by a mitochondria-targeted splice variant of PDE2, PDE2A2 [150, 151]. As genome-wide expression profiling reveals expression of PDE2A in 661w, a plausible hypothesis is that PKC-mediated sensitization of A_{2B} results via selective interaction of PKC with A_{2B} dependent on A_{2B} location. This is expected as the adenosine-binding N-terminal domain (normally located on the extracellular leaf of the plasma membrane) of A_{2B} located on mitochondria would be expected to face the cytoplasm. The roles of mitochondria- and plasma membrane-bound A_{2B} are just beginning to be defined, and will be important future studies to place in context of these results.

6.6 Conclusion

These studies demonstrate for the first time that IBMX functions as an inverse agonist of the endogenously expressed adenosine A_{2B} receptor in 661w cells, and that its action as an inverse agonist is responsible not for immediate, but for sustained alterations in mitochondrial physiology. These alterations were comprised of an increase in membrane potential, increased fusion as evidenced by increases in mitochondrial networks, and decreased respiration. Additional studies highlighted that altered mitochondrial physiology induced by inverse agonism of this receptor by IBMX may be conducted through loss of A_{2B} receptor signaling via coupling to $G\alpha_s$ and $G\alpha_{q/11}$. While more work is needed to understand the precise intracellular signaling networks perturbed by IBMX and how these alterations lead to changes in mitochondrial physiology, the studies outlined demonstrate the importance of adenosine receptor signaling in supporting mitochondrial function in 661w photoreceptor cells.

7. General Summary

7.1 Abbreviated Results and Discussion

Taken together, this work has shown that mitochondrial physiology in 661w is regulated in a time-dependent manner and via multiple mechanisms in the context of 3-isobutyl 1-methylxanthine (IBMX) administration. Central to the facilitation of this work was the development of a high content microscopic method for the high throughput measurement of mitochondrial morphology and membrane potential ([114] and **Section 3**), which complemented existing methodologies for high throughput measurement of mitochondrial respiration (Seahorse Biosciences' XF96 instrument). A brief written summary of results follows a tabular summary in **Table 7-1** and a graphical summary in **Figure 7-1**.

Mechanism (compound)	Compare to	Networked Morphology		Mitochondria Polarization		Uncoupled Respiration		Other Effects
Time (h):		*1*	*24*	*1*	*24*	*1*	*24*	
Investigatory (IBMX)	Vehicle	↑	↑	↑	↑	NC	↓	↑ cAMP+cGMP at 20 min, ↑ cell death at 48 h
PDE2 (cAMP+cGMP) inhib. (BAY60-7550)	Vehicle	/	/	/	/		NC	
PDE3 (cAMP+cGMP) inhib. (cilostamide)	Vehicle	NC	NC	↑	↑	/	↓	↑ cGMP
PDE4 (cAMP) inhib. (rolipram)	Vehicle	/	/	/	/		↑	
PDE5 (cGMP) inhib. (sildenafil)	Vehicle	↑	↑	↑	↑	/	↓	↑ cGMP
PDE7 (cAMP) inhib. (BRL 50481)	Vehicle	/	/	/	/		↑	
Adenosine A$_{2B}$ Receptor:								
A$_{2B}$ Agonist (BAY60-6583)	Vehicle	NC	↓	NC	NC	/	NC	↑ cAMP
A$_{2B}$ Antagonist (PSB-603)	Vehicle	NC	NC	NC	NC		NC	
A$_{2B}$ Inverse Agonist (MRS-1706)	Vehicle	NC	NC	NC	↑		↓	
PKA inhibitor (myr PKI 14-22)	Vehicle	NC	NC	↑	↑		NC	
Calcineurin + mPTP inhib. (cyclosporin A)	Vehicle	/	↑	↑	↑	/	/	
Calcineurin inhib. only (ascomycin)	Vehicle	NC	↑ ↓	↑	↑	/	/	
GSK-3β inhib. (3F8)	Vehicle	NC	NC	↑	NC	/	/	
COMBINATION STUDIES (IBMX + …)								
Sham (Vehicle only, no IBMX)	IBMX	↓	↓	↓	↓	NC	↑	
+ A$_{2B}$ agonist (BAY60-6583)	IBMX	/	↓	NC	↓	/	/	
+ A$_{2B}$ antagonist (PSB-603)	IBMX	/	↓	NC	↓	/	/	
+ AC activator (forskolin)	IBMX	/	↓	NC	↓	/	↑	(50% of respiration)
+ PKC agonist (PMA)	IBMX	/	↓	NC	↓	/	↑	(100% of respiration)
+ GSK-3b antagonist (3F8)	IBMX	↓	↓	↓	NC	/	/	

Table 7-1. Summary of Findings.

Statistically significant findings are listed as compared to the appropriate controls (vehicle for rows above combination studies, and as compared to IBMX for rows for combination studies (beneath the double line). Key: Light blue upwards arrow: increase compared to control. Red downwards arrow: decrease compared to controls. NC: No change compared to control. Diagonal line: not tested.
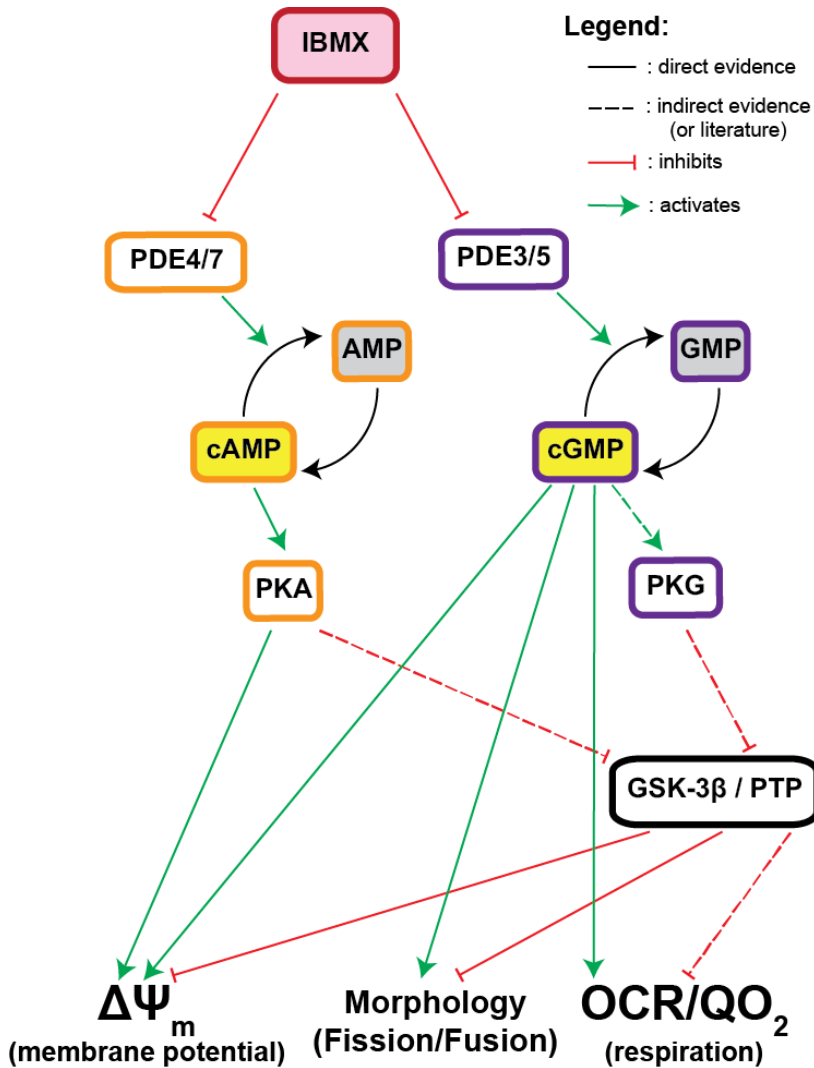
Figure 7-1. Working Model of IBMX-induced Pathways That Alter 661w Mitochondrial Physiology at 1 h, Panel A.

Integration of experimental results suggests IBMX treatment leads to altered mitochondrial physiology by multiple mechanisms in a temporally compartmentalized fashion. First, at 1 h (**Panel A**, this page), IBMX action at PDE enzymes predominates. This is followed at 24 h (**Panel B**, following page) by action as an inverse agonist at the adenosine A2B receptor. Common pathway mediators at both time points are likely to exist, and by the results these appear to include loss of function glycogen synthase kinase 3b (GSK-3β). Via this mechanism, alterations are triggered in all three parameters of mitochondrial physiology measured (mitochondrial membrane potential, Ψ_m), mitochondrial morphology (fission/fusion), and mitochondrial respiration (as measured by oxygen consumption, QO_2). mRNA expression of each protein member of the pathway printed above is confirmed in 661w by genome-wide expression profiling. A key to abbreviations is found in **Section v.: Key to Symbols, Abbreviations** on **Page xii**.

LEGEND: Solid lines represent direct evidence from studies in this dissertation. Dashed lines indicate expected relationships based on literature. Green lines with an arrowhead denote stimulation (between pathway members) or promotion of homeostasis (member to parameter), red lines with a blunt end indicate inhibition or inverse agonism (between members) or dysregulation of homeostasis (pathway member to parameter). Pathway members (in rectangles) are colored by their canonically-associated secondary messenger pathway, i.e. cAMP in orange, cGMP in purple, and PKC in cyan.

‡For sake of clarity, the results (solid arrows) indicating that selective PDE3/5 inhibition leads to alteration of all three mitochondrial physiological parameters are omitted (**Section 5.4**). Furthermore, PKG has been shown to activate an unidentified isoform of PKC following activation of mitochondrial K_{ATP} channels [147].
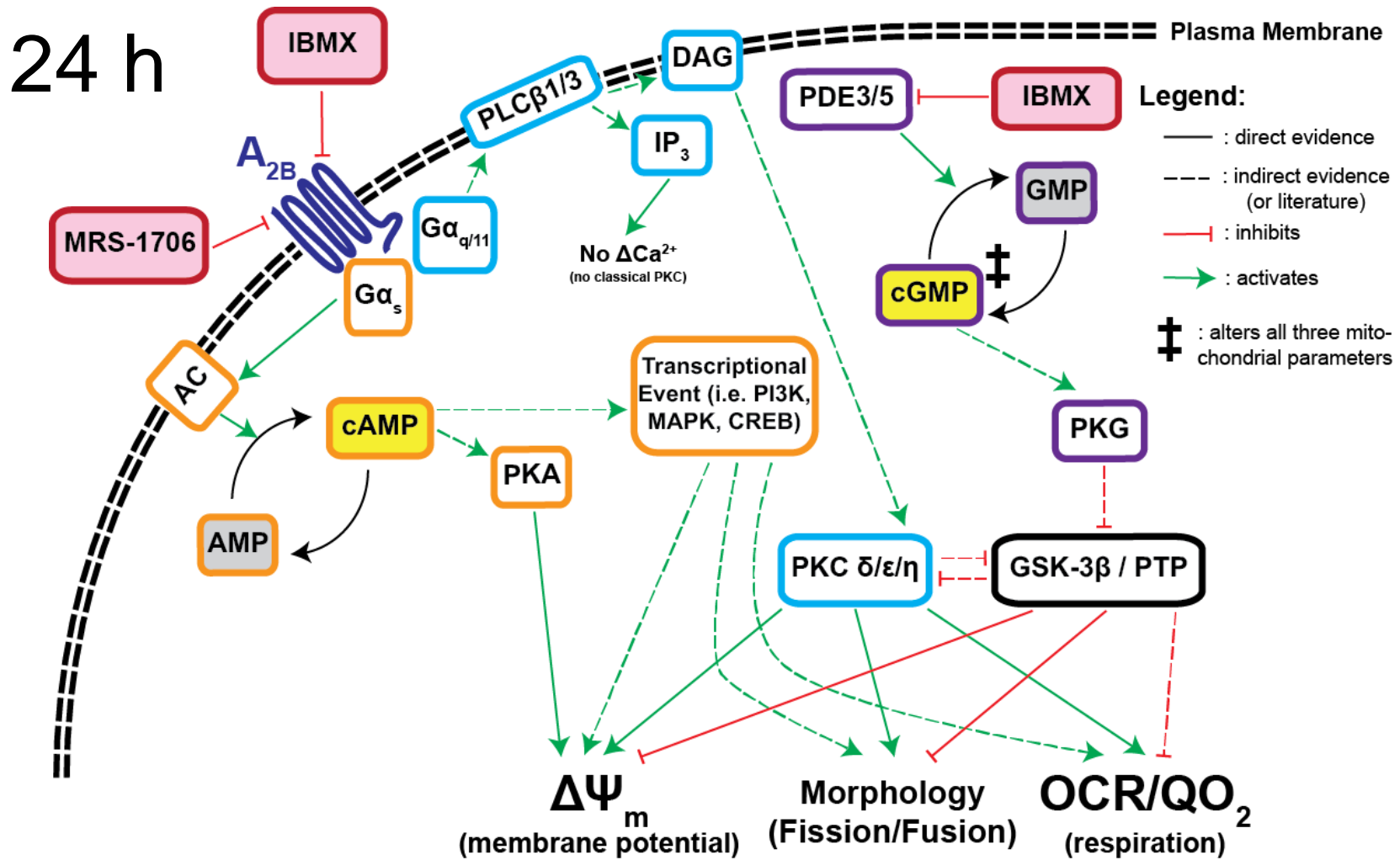
Figure 7-1 (continued). Working Model of IBMX-induced Pathways That Alter 661w Mitochondrial Physiology at 24 h, Panel B.

See legend on previous page.

The effects of IBMX on mitochondrial function are first characterized in **Section 4**, specifically that IBMX administration to 661w leads to both a rapid (at 1 h) and sustained (at 24 h) increase in microscopically measured mitochondrial membrane potential and interconnectedness (**Figure 4-3** and **Figure 4-4**). At 24 h, decreases in mitochondrial respiration, and at 48 h, a decrease in cell viability are observed (**Figure 4-2**).

Next, the role of IBMX's known function as a cyclic nucleotide phosphodiesterase (PDE) inhibitor in effecting these changes was explored in **Section 5**. Using genome-wide expression profiling, potential PDE candidate isoforms expressed in 661w were identified and selective inhibitors of these isoforms then administered to determine if a particular isoform or a particular cyclic nucleotide (cyclic adenosine monophosphate [cAMP] or cyclic guanosine monophosphate [cGMP]) were responsible for the effects induced by IBMX. IBMX administration was noted to increase both cAMP and cGMP following administration (**Figure 5-1**), but only inhibition of PDE isoforms that cleave cGMP (PDE5 and to a lesser degree PDE3) recapitulated the effects of IBMX (**Figure 5-3** and **Figure 5-5**).

The authors next sought to characterize IBMX's role in altering adenosine receptor signaling in modulating mitochondrial physiology. In these experiments, it was demonstrated that only the A_{2B} isoform was expressed (**Figure 6-1**), and that selective inverse agonist MRS-1706 – but not an agonist or antagonist – of this isoform recapitulated IBMX-induced hyperpolarization and decreased respiration at 24 h but not at 1 h (**Figure 6-2**, **Figure 6-3**, and **Figure 6-4**). Furthermore, pretreatments with agonist BAY60-6583 or antagonist PSB-603 resulted in abrogation of IBMX-induced effects at 24 h but not 1 h (**Figure 6-5** and **Figure 6-6**), leading to the conclusion that IBMX is an

inverse agonist of the A_{2B} receptor and that inverse agonism of the A_{2B} receptor facilitates sustained, but not immediate, mitochondrial dysfunction in 661w.

However, the question remained of which downstream pathways are engaged following inactivation of cGMP PDEs or A_{2B} receptor. A_{2B} has been reported to couple to (functionally signal through) multiple G protein alpha subunits, including $G\alpha_s$, $G\alpha_q$, and $G\alpha_{i/o}$ [152-156]. Hence, the next experiments elucidated the role of members of pathways that could be plausibly invoked, including adenylate cyclase, PKA, ion channels, and PKC.

As inhibition of A_{2B} coupled to $G\alpha_s$ would decrease adenylate cyclase (AC) activity (generation of secondary messenger cyclic adenosine monophosphate (cAMP) from adenosine triphosphate (ATP)), AC activator forskolin was administered prior to IBMX and determined to abrogate 100% of morphological and membrane potential changes, and approximately 50% of decreases in respiration at 24 h but not at 1 h (**Figure 6-7**). These data indicated that despite the overall increases in intracellular cAMP following IBMX exposure, long-term loss of AC activity nonetheless alters mitochondrial function.

Loss of cAMP could lead to alterations in a number of pathways, including decreased signaling through protein kinase A (PKA). At the highest concentration tested (10 µM, 277-fold above its K_i of 36 nM), PKA inhibition with a small peptide inhibitor (PKI_{14-22}) recapitulated increased membrane potential at 1 h and 24 h (**Figure 6-8**). However, no other effects were observed, leading to the conclusion that loss of PKA, if involved, is involved only tangentially. Following these results, previously described remaining possibilities of $G\alpha_s$-based signaling include PI3K, and MAPK. Combined with recent studies that demonstrate the mitochondrial localization of A_{2B} in some cell types,

there is additionally the possibility that an as yet undescribed intramitochondrial GPCR signaling cascade regulates mitochondrial physiology.

Next, the role of PKC was examined. Loss of A_{2B} signaling would be expected to decrease $G\alpha_q$-mediated signaling, in turn decreasing the activity of one or more isoforms of PKC. **Table 6-2** shows the isoforms of PKC expressed in 661w as determined using genome-wide expression profiling. By pretreating with PKC activator phorbol myristate acetate (PMA), losses in PKC signaling could be mitigated. Interestingly, 100% of changes in all three mitochondrial physiological parameters were reversed with PMA pretreatment at 24 h, but not 1 h, suggesting an active role for PKC in the maintenance of mitochondrial homeostasis (**Figure 6-9**). To determine which of the PKA subtypes were involved, single cell electrophysiological recordings were obtained following administration of IBMX, and showed no current, effectively ruling out the role of Ca^{2+}-dependent PKC isoform alpha (**Supplementary Figure 11**). Taken together, these data suggest that loss of signaling in "novel" or "atypical" isoforms of PKC, such as PKC delta or PKC epsilon may follow decreased A_{2B} signaling.

As the results thus far demonstrated a diversity of mechanisms by which mitochondrial function may be regulated, two questions were next raised: first, whether or not a common downstream mediator is involved in coordinating these messages and second, whether feedback/crosstalk occurs between these pathways.

A potential common downstream signal coordinator is glycogen synthase kinase 3 beta (GSK-3β). As it functions to regulate multiple cellular functions, including opening of the voltage-dependent anion channel (VDAC) found on mitochondria, is described as a substrate of PKA, PKC, and PKG (all three of which have been implicated in these results), GSK-3β was next examined. Inhibition of GSK-3β with selective small molecule inhibitor 3F8 (IC_{50} 34-304 nM) at 100 nM or 1 μM led to hyperpolarization at 1 h, but not

24 h (**Supplementary Figure 14**). Interestingly, preincubation with even lower

concentrations of 3F8 (1-10 nM) abrogated hyperpolarization induced by IBMX (**Figure

4-5**). Together, these data suggest that either inhibition or activation of GSK-3β results in

mitochondrial hyperpolarization, perhaps by regulation of VDAC.

As VDAC is a constitutive member of the mitochondrial membrane permeability

transition pore (mPTP), integral for ADP/ATP exchange (bioenergetics) as well as

release of cytochrome c (effector of apoptosis), efforts were undertaken to understand

its role. Unfortunately, these efforts were unsuccessful owing to the presence of

functional calcineurin in 661w. Cyclosporin A is a well-characterized inhibitor of

cyclophilin D but also is a potent calcineurin inhibitor. Experiments using a pure

calcineurin inhibitor (ascomycin) demonstrated alterations in mitochondrial membrane

potential and morphology similar to cyclosporin A, making the interpretation of mPTP's

role in early v. latent mitochondrial physiological changes induced by IBMX difficult

(**Supplementary Figure 12** and **Supplementary Figure 13**)[2].

The second question, of whether cross talk occurs between the pathways

discussed, has already been partially discussed. The most obvious level of crosstalk is

at the level of cAMP. cAMP would be expected to decrease following inverse agonism at

the A_{2B} receptor, whereas it is expected to increase following inhibition of cyclic

nucleotide phosphodiesterase enzymes. At 20 min, cAMP was found to be significantly

elevated following administration of IBMX (**Figure 5-1**). At 1 h, IBMX-induced

morphological and membrane potential effects can be observed (**Figure 4-3** and **Figure

4-4**). However, these effects were recapitulated with cGMP- but not cAMP-selective PDE

---

[2] NIM-811 is a direct, selective small molecule inhibitor of CyD/mPTP. However, it is no
longer commercially available (personal communication, John Lemasters 2014). Genetic
manipulation has its strengths, but a major weakness in these studies is the lack of kinetic control
regarding timing of knockdown (as these methods rely on protein turnover).

inhibitors (**Figure 5-3** and **Figure 5-5**), implicating cGMP as important for the immediate changes. Further arguments that implicate cGMP over cAMP in the changes observed at 1 h include the results that cAMP-selective inhibitors appeared to increase mitochondrial respiration at 24 h as compared to IBMX's decrease in respiration (**Figure 4-2** and **Figure 5-2**). Without further studies, one might be tempted to conclude that increased [cGMP] is permissive for increased [cAMP] to mediate the effects. However, activation of adenylate cyclase prior to IBMX administration resulted in no changes at 1 h, but at 24 h complete abrogation of mitochondrial hyperpolarization and networked morphological increases with partial abrogation of decreases in mitochondrial respiration was observed (**Figure 6-7**). As mentioned before, this abrogating effect was mimicked by other constituents of adenosine A_{2B} receptor signaling, including A_{2B} agonist BAY60-6583, A_{2B} antagonist PSB-603, PKC activation with PMA, (**Figure 6-5**, **Figure 6-6**, and **Figure 6-9**), while inverse agonism of the A_{2B} receptor alone recapitulated physiological changes only at 6-24 h (**Figure 6-4**).

This leads to two possible explanations for rapid yet sustained IBMX-induced alterations without taking A_{2B}-PKC signaling into context. First, an initial increase in intracellular [cAMP] is exhausted at some time between 1 h and 24 h, followed by continued inverse agonism at A_{2B}, decreasing [cAMP] at some time. Second, microdomains of [cAMP] drive A_{2B}-dependent effects on signaling. While the first option is an attractive explanation, it is not plausible to explain the effects that an inverse agonist in and of itself can cause changes as observed in **Figure 6-4**. Literature from multiple laboratories is emerging that describes the mitochondrial localization of the adenosine A_{2B} receptor and the necessary components for GPCR signaling, including an isoform of the PDE2 cAMP phosphodiesterase and localization of soluble adenylate cyclase (sAC)[149, 151, 157]. Therefore, at this time, the data best fit a mitochondrial

localization hypothesis in that some or all of A_{2B} is located on the mitochondrial membrane of 661w cells and drives latent changes in mitochondrial physiology in response to inverse agonism by IBMX. Further experiments to evaluate this hypothesis are outlined in **Section 7.2**.

7.2 Future Directions

This work highlights several avenues for future research. First, further elucidating the participation of kinases would be informative. Considering the potential for >5 downstream pathways to be involved, a medium-throughput, parallelized "kinase screen" approach measuring phosphorylation levels of downstream substrates following IBMX, MRS-1706, or sildenafil administration would be most straightforward. This approach has the added benefit of being confirmatory in cases where the downstream substrates are relatively specific. Of particular note, this experiment would be of great utility in confirming results with GSK-3β inhibitor 3F8 and PKA inhibitor myr-PKI 14-22. These results should be followed by immunoprecipitation to confirm binding of putative interacting partners. At this point, elucidation of any transcriptional activating or repressing members of the pathway should be conducted as appropriate. Chromatin immunoprecipitation for <5 targets is recommended, whereas genome-wide expression microarray followed by bioinformatic determination may be required if transcription factors remain elusive or too many targets are identified in the kinase screen.

In coordination with examining alterations in kinase activity, further exploring the role of downstream mediators to be common between the two pathways would be straightforward. Teasing apart whether GSK-3β activation follows PDE inhibition, A_{2B} inverse agonism, or both could be examined by pretreating with 3F8 prior to sildenafil administration (and repeated with cilostamide and MRS-1706) and following the same mitochondrial physiological parameters as before.

Establishing the physiological relevance of these studies is of paramount importance. The most straightforward approach to establish relevancy of PDE5 inhibition (and subsequent cGMP increase) in the retina was recently conducted by Nivison-Smith et al. ([33] and reviewed in **Section 2.4**). In short, sildenafil demonstrated limited retinal toxicity (2 days) when administered to wild-type mice but even greater and prolonged toxicity (2 weeks) to otherwise phenotypically normal $PDE6B^{wt/rd1}$ rodents as measured by electroretinogram (ERG). To further implicate PDE5 in retinal mitochondrial function, retinas from wild-type and mice homozygous or heterozygous for the rd1 mice could be isolated and measured with respirometry before and after administration of sildenafil. To measure mitochondrial membrane potential in situ, tail vein injections of TMRM prior to sildenafil or vehicle treatment could be followed by live retinal imaging to measure mitochondrial polarization prior to excision for use in respirometry or other imaging studies.

Determination of whole cell cAMP levels at 1-24 h (beyond the 20 min time period currently evaluated) would aid in determining whether inverse agonism results in global cAMP decreases outlined in the discussion above (**Section 7.1**). Immunocytochemical determination of A_{2B}'s subcellular location with concomitant labeling of mitochondria with MitoTracker Deep Red and fluorescence microscopy could determine whether or not A_{2B} is expressed on mitochondria. In conjunction with potentiometric dyes such as TMRM, the role of membrane potential in driving this localization could be subsequently determined. As previously mentioned, fluorescent cAMP biosensors would provide the ability to evaluate a mitochondrial localization hypothesis [145]. Alternative approaches include subcellular fractionation of mitochondria and Western blotting, but these approaches would result in the complete loss of spatial resolution and limit close examination of temporal information. However,

even if initial imaging studies were promising, subcellular fractionation of mitochondria in conjunction with radiolabeled ligand studies would be necessary to quantify the affinity of IBMX and adenosine for A_{2B} localized to mitochondria, as well as immunoprecipitation to determine interactions between the proposed intramitochondrial GPCR signaling complex (A_{2B}/Gα_s, Gαs/sAC). Perturbation of G protein alpha subunit signaling via agents such as cholera toxin, pertussis toxin, melittin, and suramin could provide additional support regarding the coupling of A_{2B} to Gα_s or another. The aforementioned agents would be expected to mitigate, mitigate, intensify, and mitigate (respectively) the long-term effects of IBMX if inverse agonism at A_{2B} results in decreased Gα_s signaling, and would effectively rule out the role of Gα_i coupling. Gα_q could be further implicated via usage of newly reported Gα_q inhibitor BIM-46187, which would be expected to recapitulate the effects of A_{2B} inverse agonist MRS-1706 [158].

7.3 Conclusion

These results have several implications for retinal and mitochondrial research, as well as for researchers outside of these fields. Firstly, the generation of a high throughput high content image analysis tool to simultaneously quantify mitochondrial interconnectedness and polarization should boost efforts of the mitochondrial research community to identify small molecules, proteins, and genes that influence mitochondrial physiology, from bioenergetics to biogenesis and mitochondrial turnover. Secondly, the result that retina-derived 661w mitochondrial respiration is responsive to alterations in phosphodiesterase function provides evidence of a complex bioenergetic regulatory system that may serve to limit mitochondrial function in sustained photoreceptor neuron stimulation, while providing a mechanism by which sildenafil side effects and toxicity may manifest. Furthermore, this research describes IBMX's activity as an inverse agonism at the adenosine A_{2B} receptor for the first time, and elucidates the intracellular

pathways engaged both by A_{2B} and known targets of IBMX, the cyclic nucleotide PDE's. Researchers using IBMX as a tool are cautioned that its effects on mitochondrial function may confound their results.

8. Glossary

- **Agonist** – a small molecule or protein that upon binding to a receptor, stimulates one or more downstream signaling pathways (positive efficacy). Agonists stimulate signaling beyond constitutive activity levels.

- **Antagonist** – a small molecule or protein that upon binding to a receptor, competitively (same site) or noncompetitively (alternate site) inhibits agonist binding or agonist-induced conformational changes and thus reduces agonist-stimulated signaling (zero efficacy, equivalent to unstimulated receptor). Antagonists do not reduce constitutive activity of receptor signaling (that level of signaling achieved in absence of agonist).

- **Chelator** – chemical substance that binds another to reduce the free concentration of the latter, typically, metal ions such as Ca^{2+}, Mg^{2+}, or Fe^{2+}. May also be referred to as a "buffer".

- **Ionophore** – substance which increases membrane permeability to an ion, e.g. FCCP increases membrane permeability to H^+, uncoupling respiration from ATP production.

- **Inverse agonist** – a small molecule or protein that upon binding to a receptor, induces decreased signaling beyond that observed with unstimulated receptor (negative efficacy, termination of constitutive activity). Inverse agonists do reduce constitutive activity of receptor signaling.

- **Kappa statistic (κ)** – a measure of interobserver agreement. Values range from 0 (complete disagreement) to 1 (perfect agreement).

- **Ligand** – a small molecule or protein capable of binding to a receptor (may be an agonist, antagonist, or inverse agonist; typical usage is to describe the endogenous or natural agonist).

- **Machine Learning** – Statistical method for establishing/optimizing a classification paradigm using known measurements.

- **Matthew's Correlation Coefficient (Φ, or Phi Coefficient)** – Measure of quality of a machine learning binary classification. Values range from -1 (total disagreement) to 0 (no better than random agreement) to +1 (perfect agreement).

- **Registration** – Alignment of multidimensional data (spatial and or spatiotemporal). In this manuscript, alignment of two dimensional microscopic images. Algorithms define "source" image as misaligned image; "target" image is image to which alignment is made.

- **Segmentation** – the identification of objects in an image's foreground from its background.

9. Appendix A—Supplementary Figures and Images
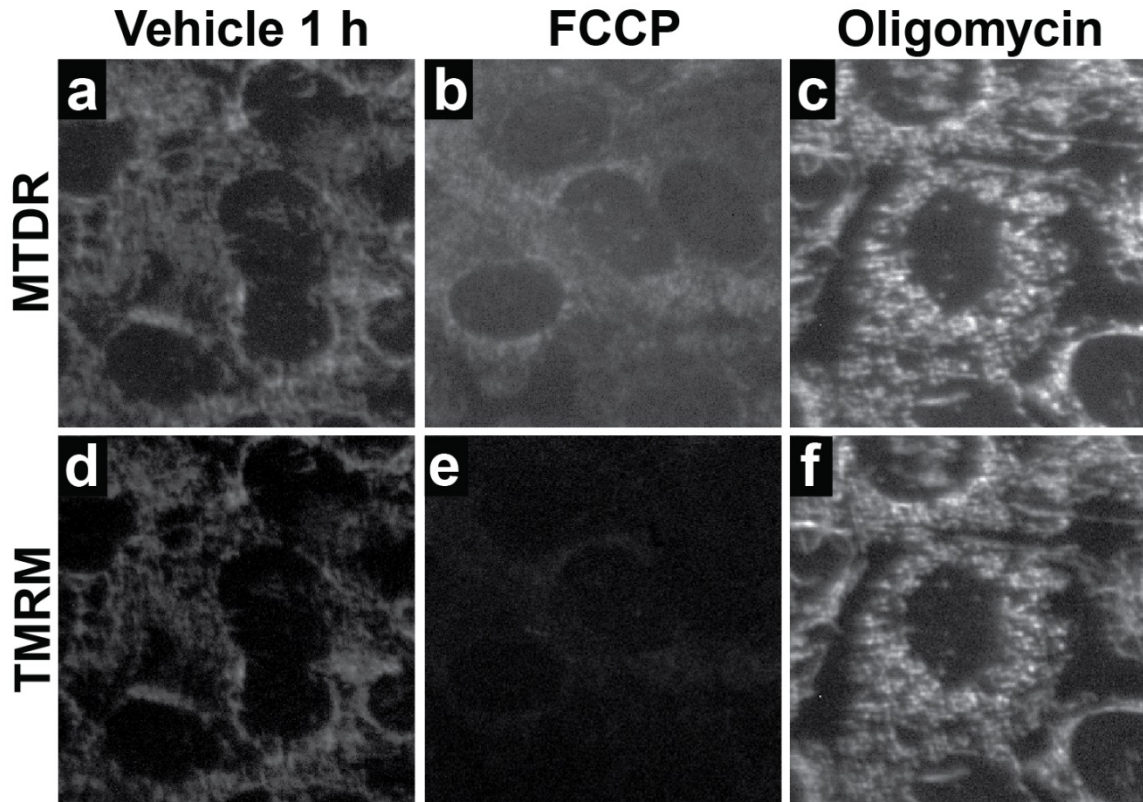
Supplementary Figure 1. MitoTracker Deep Red (MTDR) is retained in depolarized mitochondria.

Cells were dually stained with MTDR and tetramethylrhodamine methyl ester (TMRM). A representative field was chosen by selecting a cell with TMRM fluorescence intensity near the median of each condition – and the raw, unprocessed image containing that cell displayed (MTDR in a-c, TMRM in d-f). Vehicle (a, d), FCCP (b, e), oligomycin (c, f). Brightness and contrast settings were set to be equal for all panels within each row to facilitate comparison. Colocalization of the two dyes was calculated using Pearson's correlation in images; typically reaching values >0.90 (data not shown).
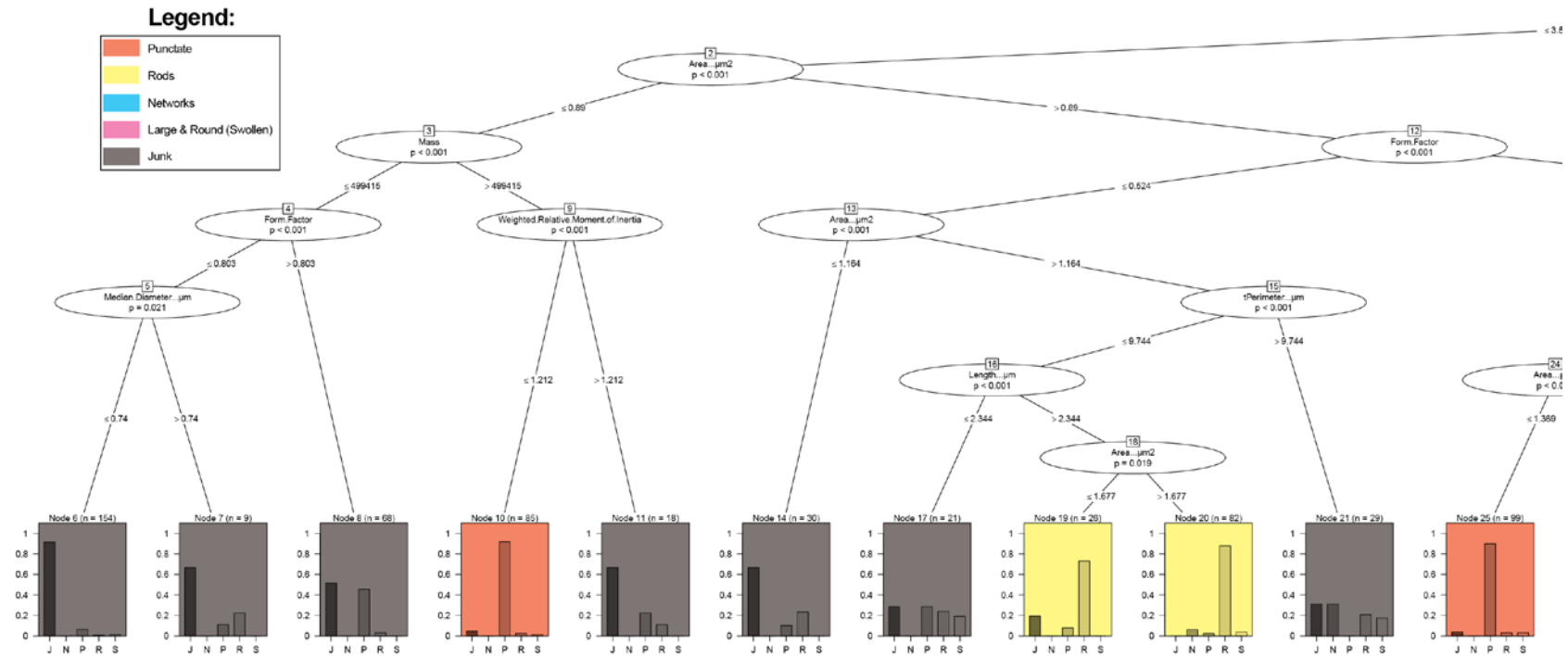
Supplementary Figure 2. Conditional Inference Recursive Partitioning Decision Tree (Mitochondrial Classification Scheme).

In a separate protocol, Developer Toolbox analysis was configured to output all calculable morphological measures on the total (unclassified) mitochondrial population. 897 mitochondria (training set) spanning four different experimental conditions and multiple microscopic fields were manually classified into one of five categories (Networks (N), Rods (R), Puncta (P), Large and Round (LR – "S" in the diagram above), or Junk (J). This training set was then used as input to the conditional inference algorithm found in the ctree method within R package "party". See Supplementary File 2 for a copy of the R code used to generate the above tree. The final branches of this tree were assigned to a single category (as shown by unique colors in the legend) based on accuracy, converted into logic statements, input into Developer Toolbox's inclusion criteria for each mitochondrial target (subtype), and then used to classify mitochondria into the four morphological bins. The fifth class was included in the classifier to remove aberrantly detected objects, characteristic of background noise, Junk (J). As expected, similar morphologies clustered near each other with regards to morphological parameters. One example of this clustering can be observed as the cyan networks are found exclusively on the right branch of the first node, sharing a length greater than 3.525 μm. The importance of any individual measure in segregation can be measured by the number of the nodes/branches preceding it (e.g. Length is most important as it is the first node) and the number of times it appears (e.g. Area and Form Factor appear 5 and 3 times, respectively).

117
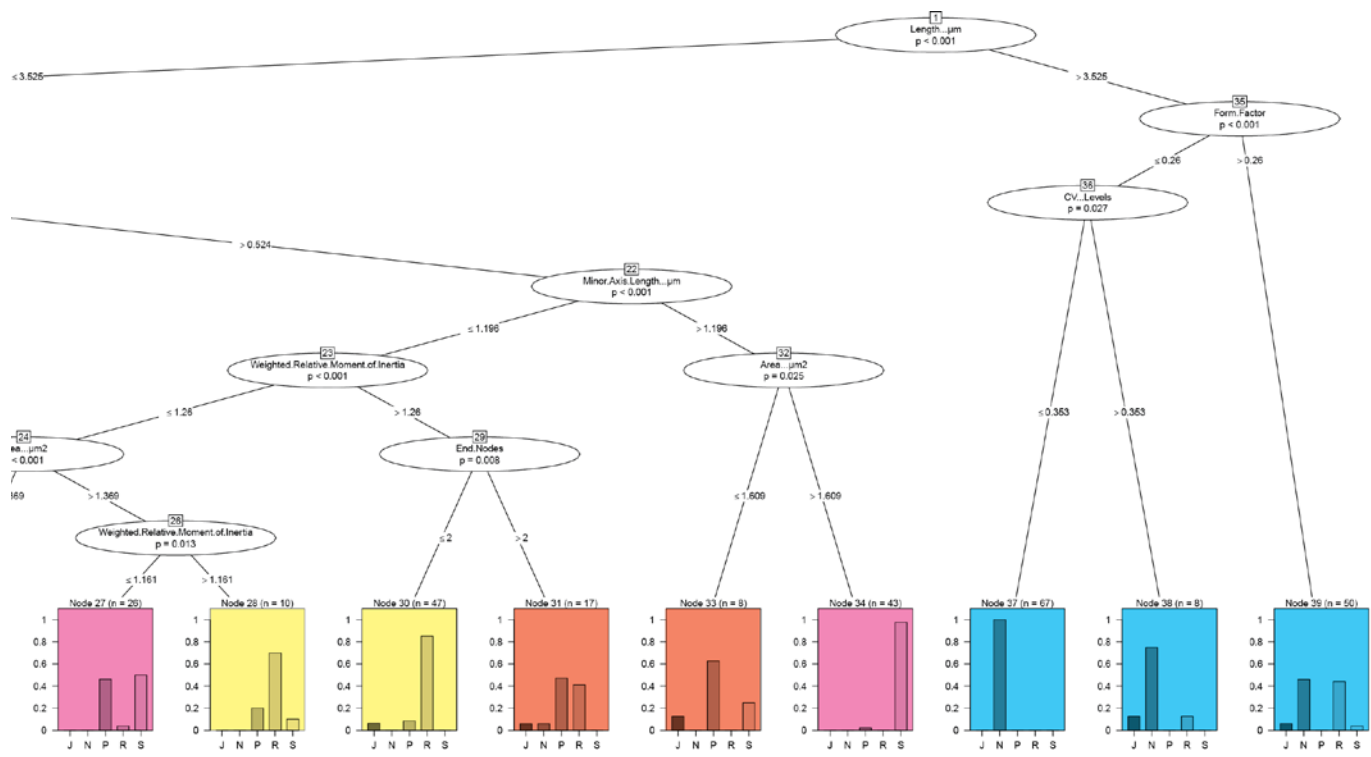
Supplementary Figure 2 (continued). Conditional Inference Recursive Partitioning Decision Tree (Mitochondrial Classification Scheme).
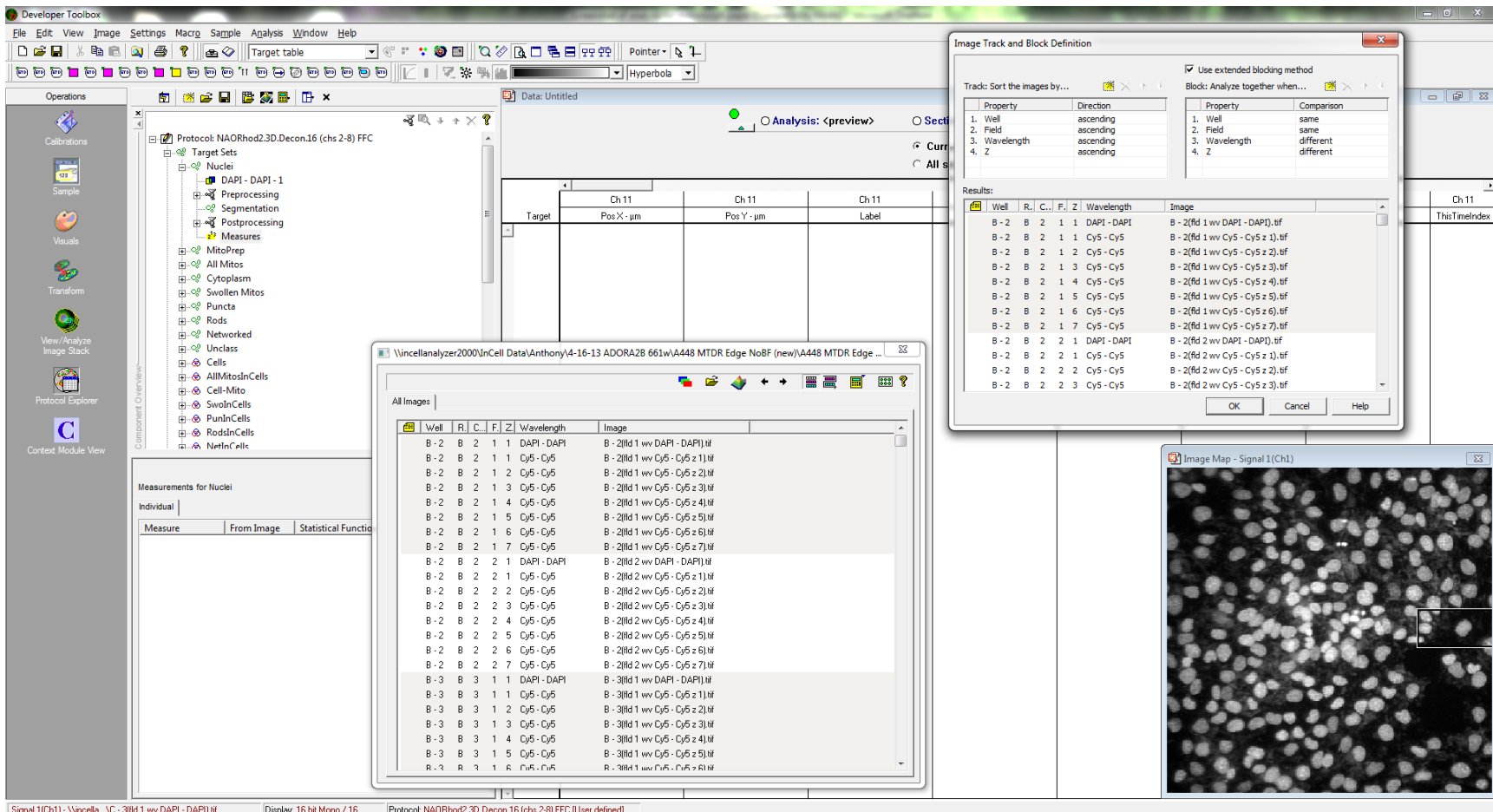
Supplementary Figure 3. Developer Toolbox screenshot 1 – Program Control.

Tracking and blocking definition settings necessary for 2D deconvolution preprocessing shown in the two popup windows. These settings are 1) use extended blocking method, 2) sort by wavelength before Z position, and 3) analyze together when wavelength and z are different.
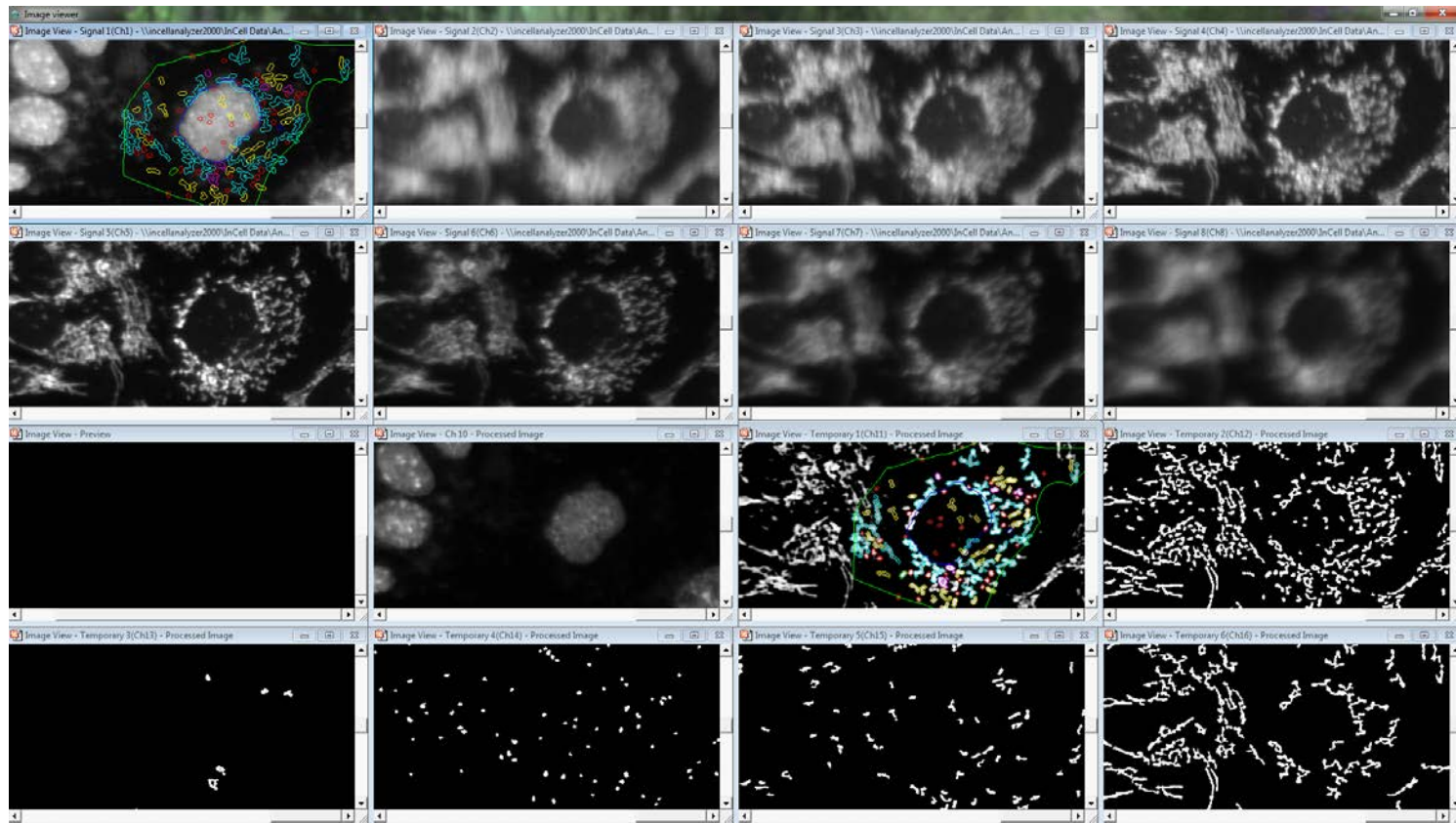
Supplementary Figure 4. Image Analysis Screenshot. Overlay colors correspond to those in Figure 2 of main paper. Channel definitions from top left:

Ch 1: Hoechst 33342-stained nuclei (with morphological results overlaid)
Chs 2-8: z stack of MitoTracker Deep Red (Ch 5 is in-focus channel)
Ch 9: unused, reserved for future use
Ch 10: preprocessed nuclei
Ch 11: preprocessed MitoTracker Deep Red (2D deconvolution/nearest neighbor deblur, followed by histogram equalization)

Ch 12: binary/segmented image of Ch 11 (all mitochondria)
Ch 13: binary image of Swollen mitochondria (Large & Round)
Ch 14: binary image of Punctate mitochondria
Ch 15: binary image of Rod mitochondria
Ch 16: binary image of Networked mitochondria
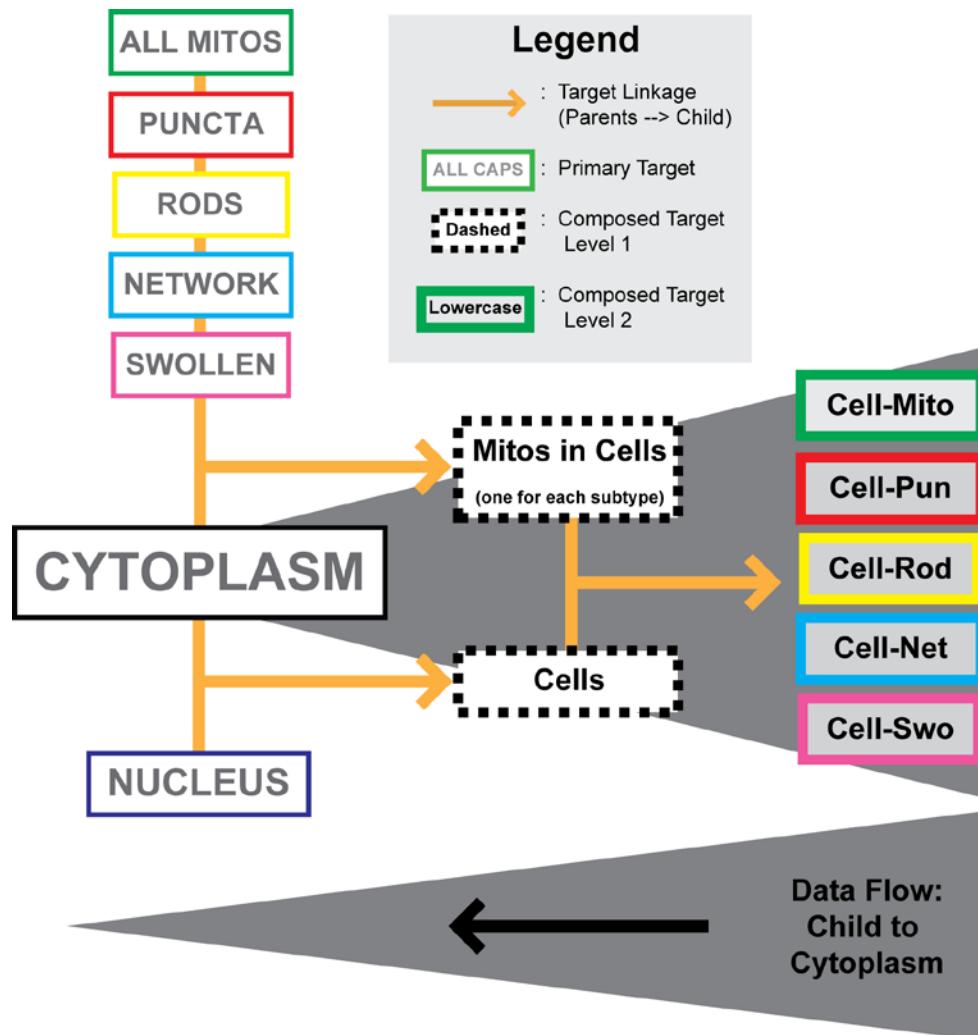
Supplementary Figure 5. Target Linking Summary.

Programmatic diagram summarizing the overall relationship of segmented (identified) objects to one another. One-to-one and one-to-many linkages were made to assign child object(s) to a single parent (left column, thin color border). Then, these linkages were linked to one another in composed one-to-one linkages (level 1, center column, dashed borders). Finally, these composed linkages were linked to Cells to tie every mitochondrion of each subtype to a Cell in the center column (right column, bold borders). The overall goal of this hierarchical relationship was multifold: 1. To ensure all measures arising from multiple object types could be correlated to one another in the final analysis on a cell-by-cell basis (e.g. size of a cell with size/shape of a nucleus can be examined simultaneously with abundance of punctate mitochondria). 2. To remove from the analysis aberrantly detected objects too distant from a cell (any objects not assigned to a cell were not quantified). 3. By correlating multiple measures, quality control on a per-cell basis can be achieved (e.g. out of focus or dead). Nota bene: programmatically, large and round mitochondria are referred to as "swollen" or "swo" in code and in the chart above. However, "large & round" is used to describe this population because swollen is a physiological, not morphological definition.

Author AL	a -Training Set	Predicted						Φ (Matthew's Correlation)	Kappa (κ)
		J	N	P	R	LR	Total		
	Junk (J)	229	4	10	8	0	251	0.706	
	Networks (N)	9	96	1	5	0	111	0.787	
	Puncta (P)	55	0	180	10	13	258	0.698	
	Rods (R)	25	23	12	138	1	199	0.702	
	Large & Round (LR)	11	2	6	4	55	78	0.728	
TOTAL		329	125	209	165	69	897		κ=0.710

AL+RC Classify Together	b - Test Set	Predicted						Φ (Matthew's Correlation)	Kappa (κ)
		J	N	P	R	LR	Total		
	Junk (J)	154	0	2	9	0	165	0.608	
	Networks (N)	9	39	0	2	0	50	0.793	
	Puncta (P)	57	0	61	0	3	121	0.511	
	Rods (R)	28	7	18	88	1	142	0.653	
	Large & Round (LR)	0	0	2	2	7	11	0.628	
TOTAL		248	46	83	101	11	489		κ=0.601

Supplementary Table 1. Confusion matrices to evaluate decision tree performance.

Contingency tables for each category (true positive, true negative, false positive, false negative) were assembled from the confusion matrix, and Φ (Matthew's Correlation) calculated to evaluate the classifier's performance for each category. The κ-statistic was used to assess agreement across all categories as well. Performance of classifier against data used to train (generated by author AL) (a) and versus the consensus decision of authors AL & RC on the full test set (b).

a - Test Set	J	N	P	R	LR	Total	Φ (Matthew's Correlation)	Kappa (κ)
Junk (J)	183	0	8	10	0	201	0.674	
Networks (N)	7	33	0	1	0	41	0.737	
Puncta (P)	35	0	57	0	3	95	0.563	
Rods (R)	23	13	17	89	1	143	0.660	
Large & Round (R)	0	0	1	1	7	9	0.697	
TOTAL	248	46	83	101	11	489		κ=0.644

(Author AL / Author RC)

b - Test Set	J	N	P	R	LR	Total	Φ (Matthew's Correlation)	Kappa (κ)
Junk (J)	132	1	56	12	0	201	0.649	
Networks (N)	0	37	0	4	0	41	0.781	
Puncta (P)	6	0	83	6	0	95	0.588	
Rods (R)	9	14	12	105	3	143	0.691	
Large & Round (LR)	0	0	4	1	4	9	0.496	
TOTAL	147	52	155	128	7	489		κ=0.641

(Author AL)

c - Test Set	J	N	P	R	LR	Total	Φ (Matthew's Correlation)	Kappa (κ)
Junk (J)	136	0	1	10	0	147	0.548	
Networks (N)	10	37	0	5	0	52	0.730	
Puncta (P)	74	0	72	2	7	155	0.535	
Rods (R)	28	9	9	82	0	128	0.638	
Large & Round (LR)	0	0	1	2	4	7	0.446	
TOTAL	248	46	83	101	11	489		κ=0.557

(Author RC)

d - Test Set (subset)	J	N	P	R	LR	Total	Φ (Matthew's Correlation)	Kappa (κ)
Junk (J)	125	0	0	7	0	132	0.724	
Networks (N)	6	31	0	0	0	37	0.807	
Puncta (P)	25	0	55	0	3	83	0.711	
Rods (R)	14	7	7	77	0	105	0.759	
Large & Round (LR)	0	0	0	0	4	4	0.753	
TOTAL	170	38	62	84	7	361		κ=0.731

(AL+RC Agreements Only)

e - Test Set (subset)	J	N	P	R	LR	Total	Φ (Matthew's Correlation)	Kappa (κ)
Junk (J)	29	0	2	2	0	33	0.325	
Networks (N)	3	8	0	2	0	13	0.726	
Puncta (P)	32	0	6	0	0	38	-0.011	
Rods (R)	14	0	11	11	1	37	0.309	
Large & Round (LR)	0	0	2	2	3	7	0.549	
TOTAL	78	8	21	17	4	128		κ=0.258

(AL+RC Disagreements Only)

Supplementary Table 2. Confusion matrices to evaluate decision tree performance (Part 2).

Additional confusion matrices were generated: first, against the same test set of data used in Supplementary Table 1Supplementary Table 1. Confusion matrices to evaluate decision tree performance.

Contingency tables for each category (true positive, true negative, false positive, false negative) were assembled from the confusion matrix, and Φ (Matthew's Correlation) calculated to evaluate the classifier's performance for each category. The κ-statistic was used to assess agreement across all categories as well. Performance of classifier against data used to train (generated by author AL) (a) and versus the consensus decision of authors AL & RC on the full test set (b).b using author AL's blinded classifications (a), amongst authors AL and RC (b), and amongst author RC (blinded) and the classifier (c). The classifier is also compared to the subset of 361 mitochondria in the test set upon which both authors agreed (d), and the

subset of 128 mitochondria the authors disagreed (e). In all panels of this table, the authors were blinded from one another, whereas the authors worked together to reach consensus agreement for test set in Supplementary Table 1b.
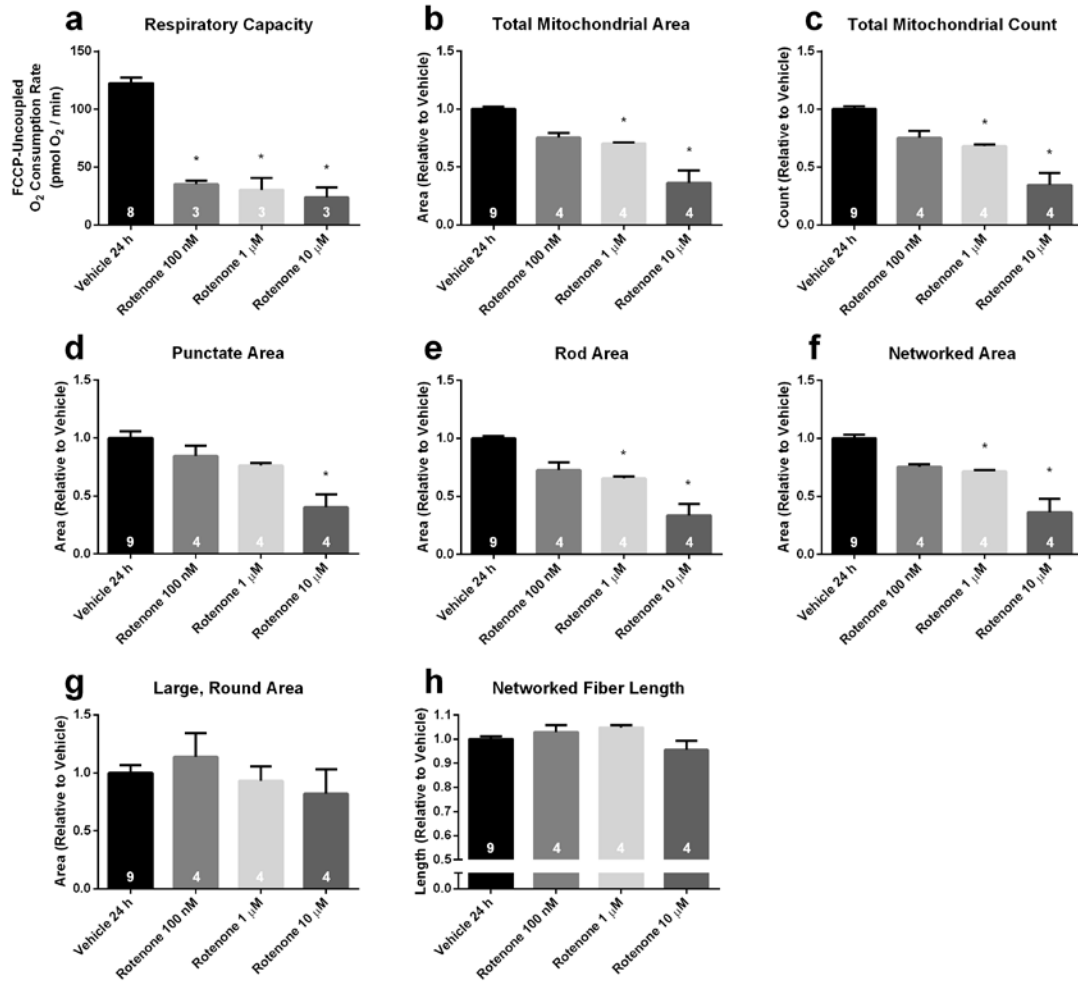
Supplementary Figure 6. Quantitative assessment of mitochondrial morphology after mitochondrial electron transport chain Complex I inhibition via rotenone.

Carbonyl cyanide-p-trifluoromethoxyphenylhydrazone (FCCP)-uncoupled respiratory capacity (mitochondrial respiration) was measured via Seahorse XF96 respirometry following 24 h treatment with rotenone at the concentrations indicated (a). Results of the corresponding mitochondrial morphological assessment (b-h). n=4-9 experiments (numbers on each bar), bars s.e.m. Data analyzed by Kruskal-Wallis followed by Dunn's post test, all groups versus vehicle only. *p<0.05 versus vehicle.
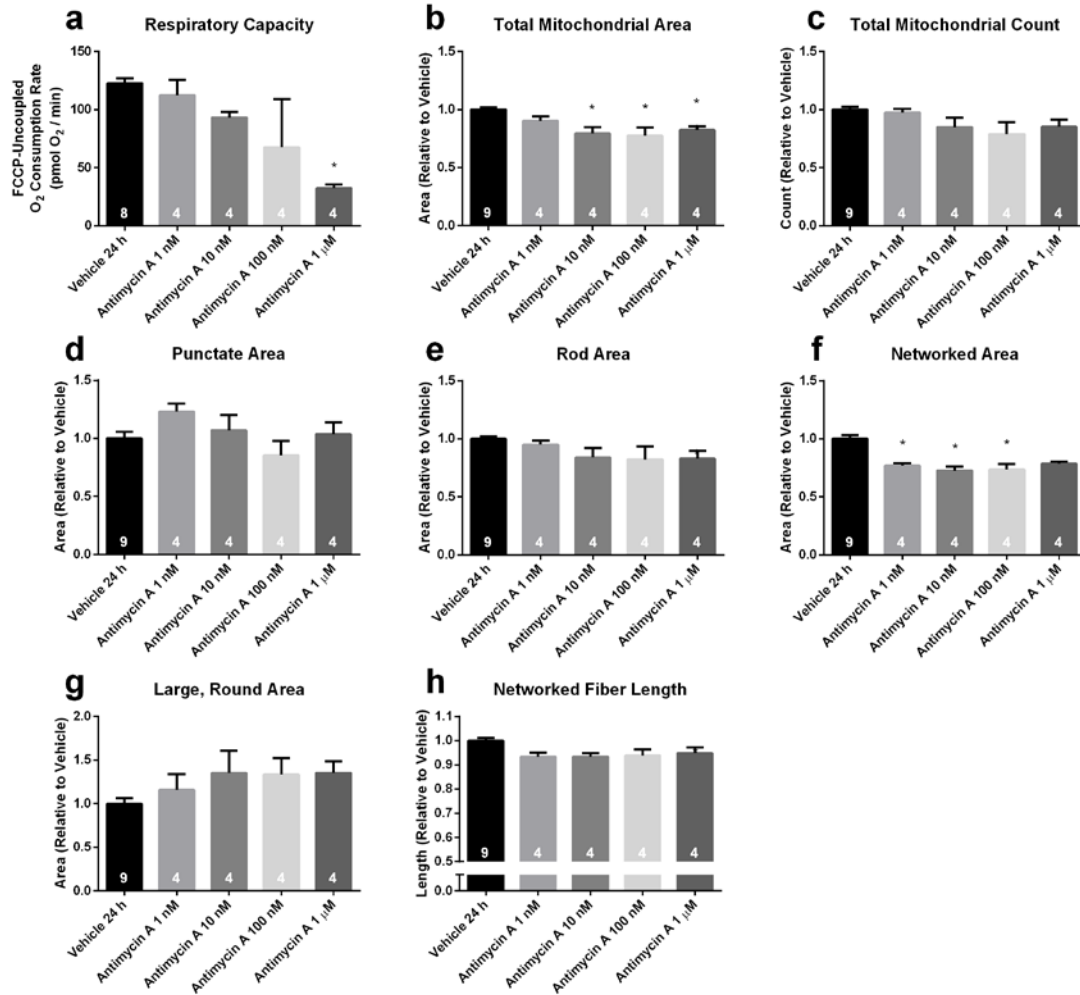
Supplementary Figure 7. Quantitative assessment of mitochondrial morphology after mitochondrial electron transport chain Complex III inhibition via antimycin A.

Carbonyl cyanide-p-trifluoromethoxyphenylhydrazone (FCCP)-uncoupled respiratory capacity (mitochondrial respiration) was measured via Seahorse XF96 respirometry following 24 h treatment with antimycin A at the concentrations indicated (a). Results of the corresponding mitochondrial morphological assessment (b-h). n=4-9 experiments (numbers on each bar), bars s.e.m. Data analyzed by Kruskal-Wallis followed by Dunn's post test, all groups versus vehicle only. *$p < 0.05$ v. vehicle.
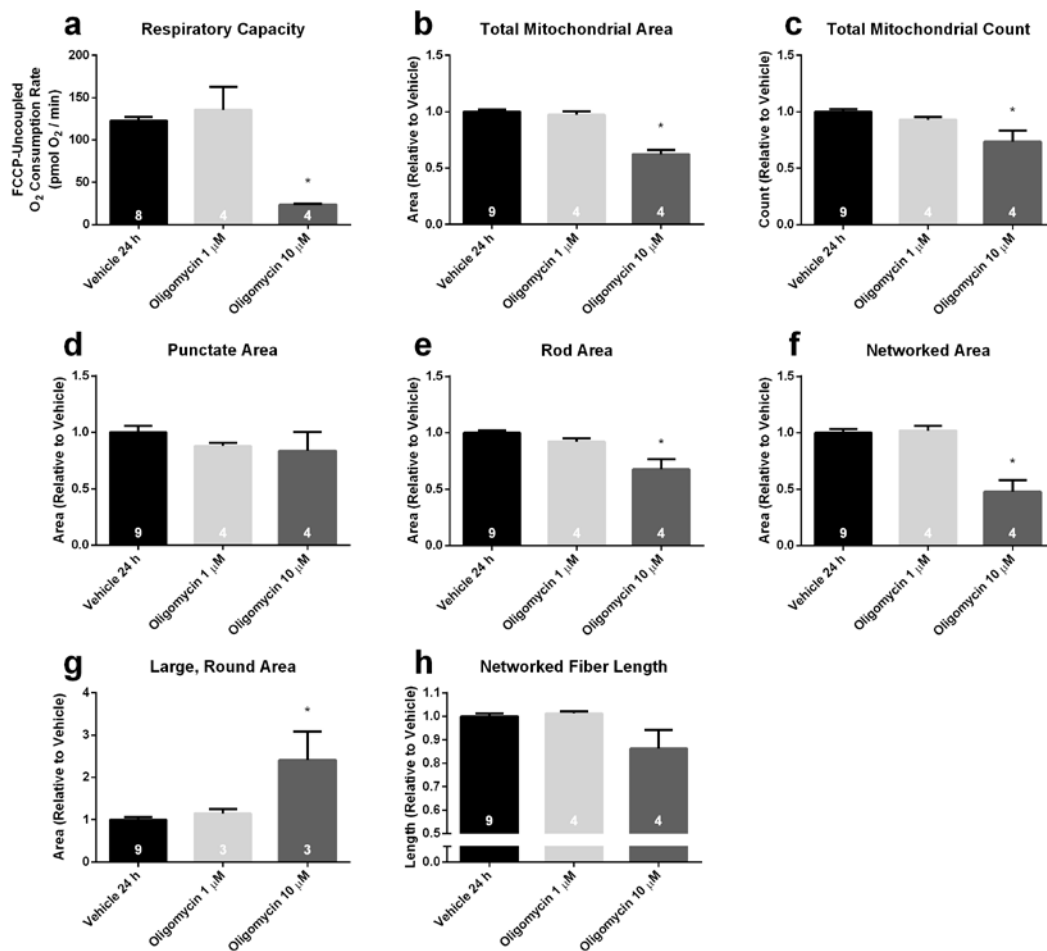
Supplementary Figure 8. Quantitative assessment of mitochondrial morphology after mitochondrial electron transport chain complex V inhibition via oligomycin.

Carbonyl cyanide-p-trifluoromethoxyphenylhydrazone (FCCP)-uncoupled respiratory capacity (mitochondrial respiration) was measured via Seahorse XF96 respirometry following 24 h treatment with oligomycin at the concentrations indicated (a). Results of the corresponding mitochondrial morphological assessment (b-h). n=4-9 experiments (numbers on each bar), bars s.e.m. Data analyzed by Kruskal-Wallis followed by Dunn's post test, all groups versus vehicle only. *p<0.05 v. vehicle.
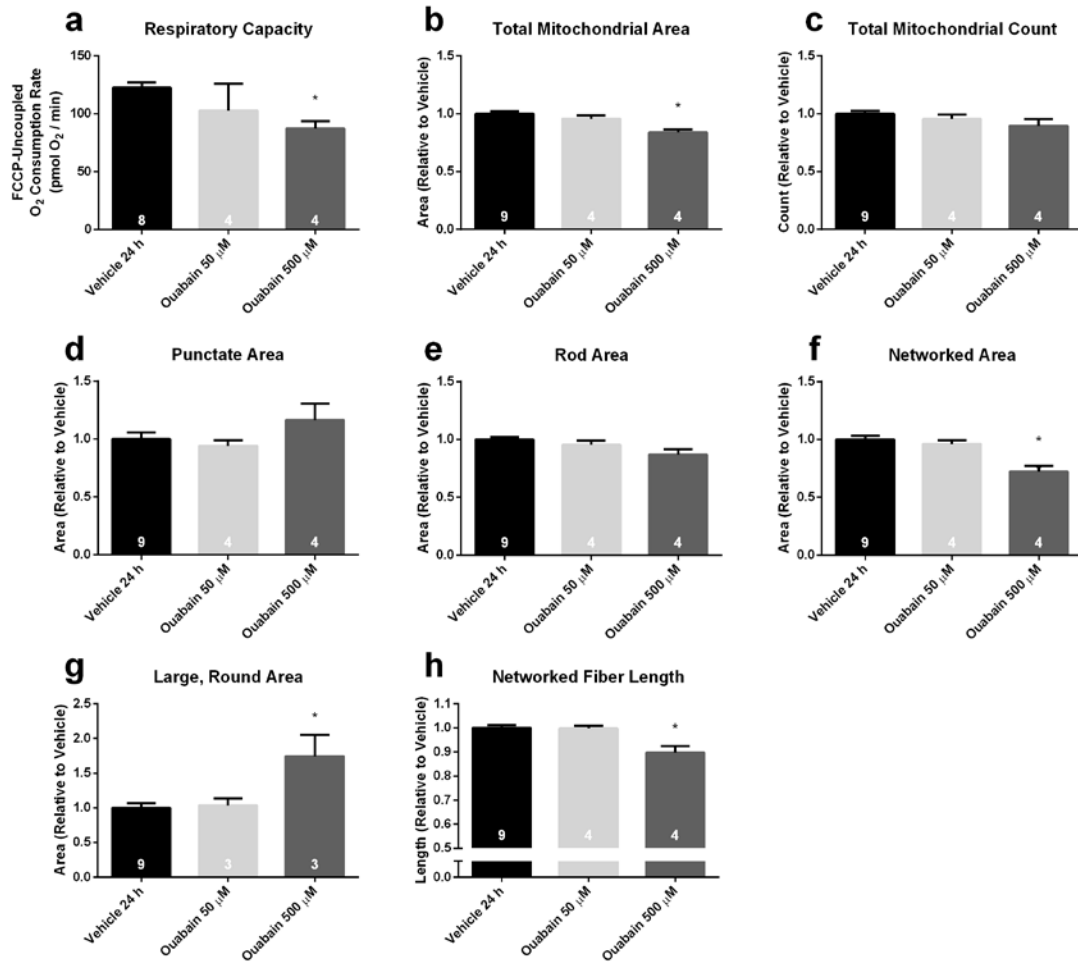
Supplementary Figure 9. Quantitative assessment of mitochondrial morphology after Na/K ATPase inhibition.

Carbonyl cyanide-p-trifluoromethoxyphenylhydrazone (FCCP)-uncoupled respiratory capacity (mitochondrial respiration) was measured via Seahorse XF96 respirometry following 24 h treatment with oligomycin at the concentrations indicated (a). Results of the corresponding mitochondrial morphological assessment (b-h). n=4-9 experiments (numbers on each bar), bars s.e.m. Data analyzed by Kruskal-Wallis followed by Dunn's post test, all groups versus vehicle only. *p<0.05 v. vehicle.

Treatment	Network	Rod	Puncta	Large & Round
Vehicle Control	60.9 ± 1.84%	28.4 ± 1.32%	9.0 ± 0.55%	1.7 ± 0.09%
TBHP 1 mM	45.4 ± 2.14%	34.3 ± 1.15%	16.2 ± 1.11%	4.0 ± 0.16%
Antimycin A 1 µM	56.8 ± 1.02%	30.0 ± 0.82%	10.7 ± 0.41%	2.5 ± 0.28%
Oligomycin 10 µM	45.5 ± 8.72%	33.0 ± 3.78%	16.8 ± 3.96%	4.7 ± 1.05%
Rotenone 10 µM	63.7 ± 2.32%	24.8 ± 1.22%	8.7 ± 0.60%	2.9 ± 0.58%
Ouabain 500 µM	52.5 ± 3.29%	31.9 ± 1.72%	12.4 ± 1.83%	3.2 ± 0.49%

Supplementary Table 3. Relative abundance of mitochondrial morphological subtypes.

Mean percentages of each subtype area within total mitochondria per cell are shown ± s.e.m. among n=4-9 experiments.

Treatment	Phenotype				
	Network	Rod	Puncta	Large & Round	Total
Vehicle	74.8 ± 7.32 µm²	38.9 ± 3.23 µm²	11.1 ± 0.73 µm²	2.2 ± 0.13 µm²	130.1 ± 11.1 µm²
TBHP 1 mM	60.8 ± 6.97 µm²	38.1 ± 4.27 µm²	16.4 ± 0.92 µm²	4.7 ± 0.15 µm²	123.3 ± 11.21 µm²
Antimycin A 1 µM	66.1 ± 20.42 µm²	36.5 ± 11.13 µm²	12.2 ± 3.89 µm²	2.82 ± 0.86 µm²	120.2 ± 37.31 µm²
Oligomycin 10 µM	30.5 ± 7.68 µm²	27.7 ± 8.66 µm²	16.2 ± 4.55 µm²	4.5 ± 1.29 µm²	78.6 ± 24.01 µm²
Rotenone 1 µM	86.0 ± 8.14 µm²	39.6 ± 3.30 µm²	13.1 ± 0.77 µm²	2.8 ± 0.18 µm²	144.4 ± 11.50 µm²
Ouabain 500 µM	66.5 ± 8.96 µm²	38.67 ± 0.77 µm²	16.4 ± 1.42 µm²	4.4 ± 0.53 µm²	172.5 ± 43.98 µm²

Supplementary Table 4. Absolute abundance of mitochondrial morphological subtypes.

Mean area of mitochondrial area of each subtype per cell per treatment group are shown ± s.e.m. among n=4-9 experiments.
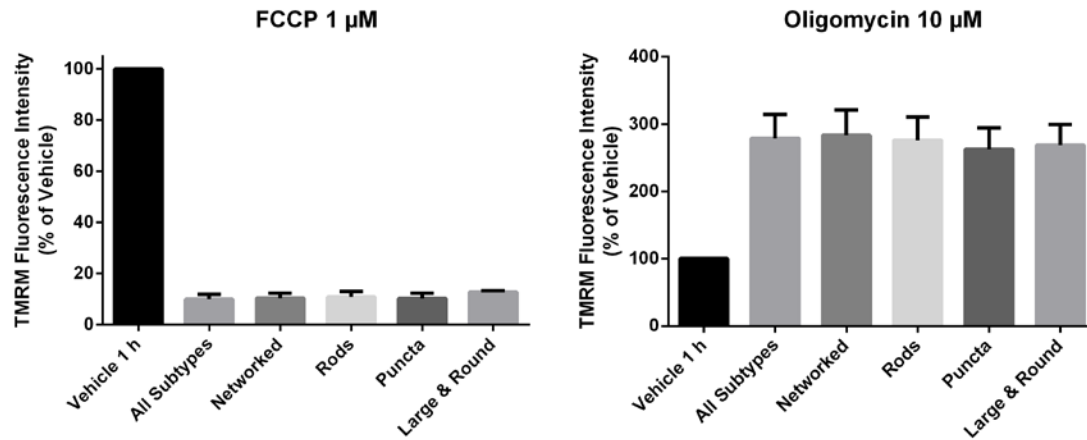
Supplementary Figure 10. Morphological subtypes are equally susceptible to depolarization.

Mean background-subtracted fluorescence intensity of tetramethylrhodamine methyl ester (TMRM) fluorescence was determined within each subtype of mitochondria or all subtypes in aggregate (All) for cells treated with 1 µM carbonyl cyanide-p-trifluoromethoxyphenylhydrazone (FCCP) (a) or 10 µM oligomycin (b) for 1 h. This value was then normalized by dividing the average background-corrected fluorescence intensity of the corresponding mitochondrial phenotype in cells treated with vehicle for each experimental n. Data shown in each column are each experimental mean (dots), mean of experiments (center long bar), and s.e.m. (shorter bars above and below mean). Comparisons were made amongst all subtype polarization ratios (excluding vehicle) using one-way ANOVA followed by pairwise comparisons with Holm-Sidak's correction to determine significant differences between groups. No multiplicity-adjusted p values were lower than 0.05.
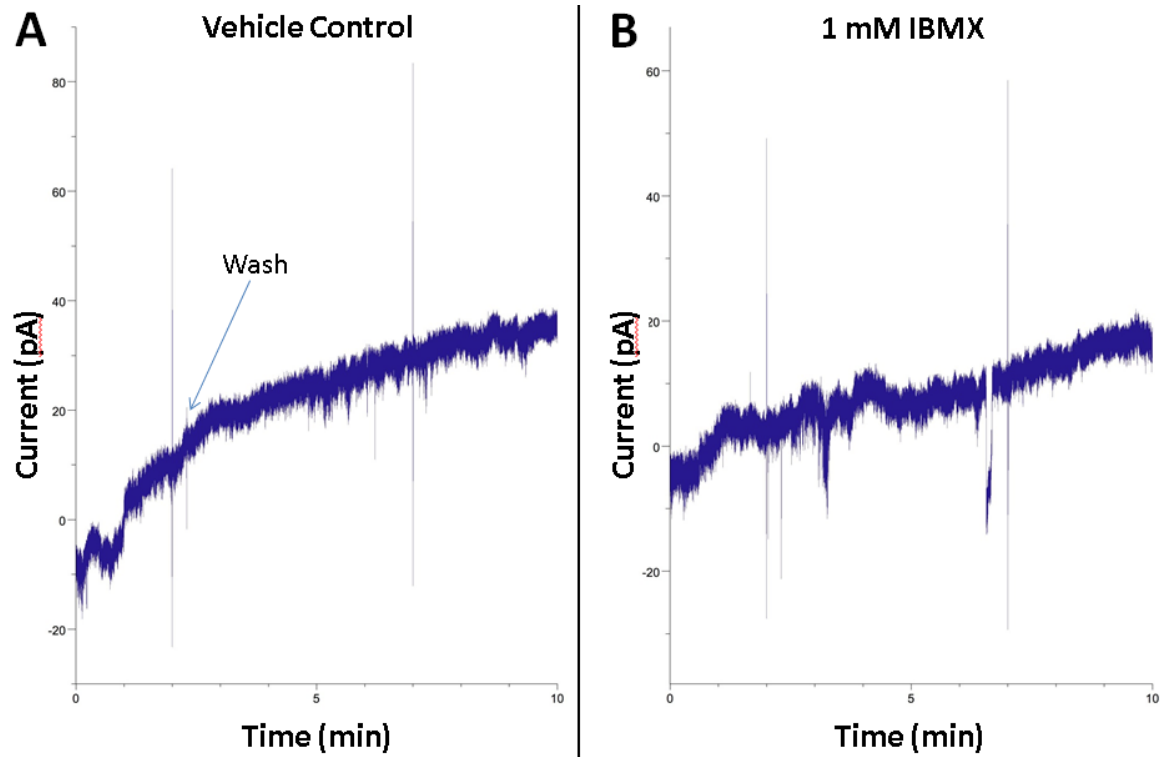
Supplementary Figure 11. IBMX Administration Fails to Induce Plasma Membrane Current in 661w

Vehicle (A) or IBMX (B) were administered to 661w cells by superfusion after collecting 2 min of baseline recording. After 5 min, the superfusate was changed to recording buffer and an additional 3 min of recording obtained. Data shown are baseline averages of n=3 cells in each group. The failure to observe deflections greater than 20 pA in magnitude and the absence of sustained deflections are interpreted as no IBMX-induced currents. Administration of 8-Br cGMP was also examined to induce no deflections (n=1).

A Networked Mitochondria

B Mitochondrial ΔΨ (All Subtypes)

Time (h)	IBMX 500 μM	Cyclosporin A 1 μM	10 μM
1	X	X	
24	X	X	X
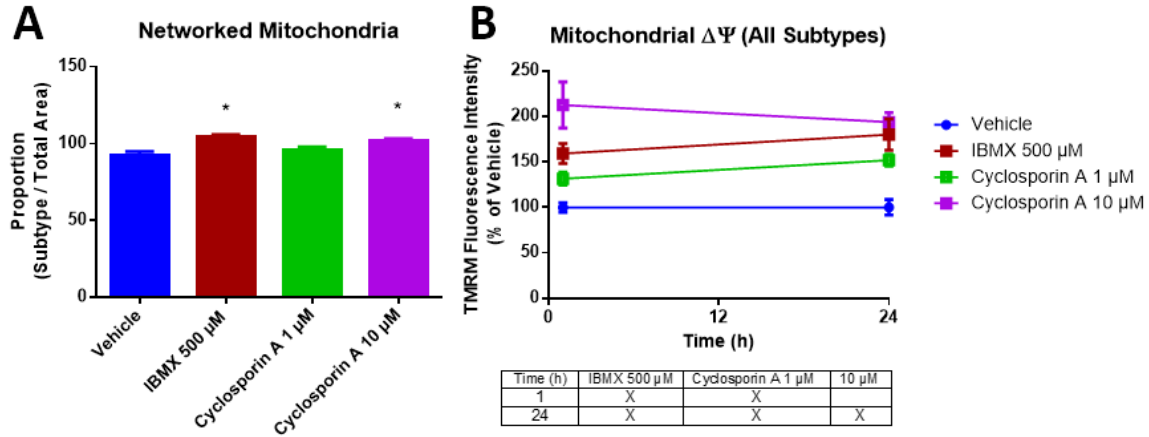
Supplementary Figure 12. Cyclosporin A Increases Membrane Potential and Mitochondrial Interconnectedness.

661w photoreceptor cell line mitochondria were subjected to morphological and membrane potential analysis as previously described [114]. Proportion of networked mitochondria following 24 h treatment is presented in (A), and mitochondrial membrane potential in (B). Data shown are mean ± s.e.m. of n=5 experiments. * or "X": multiplicity-adjusted $p < 0.05$. Analyzed by one-way (A) or two-way ANOVA (B), post-test treatment group versus vehicle at each time point.

A — Networked Mitochondria

B — Mitochondrial ΔΨ (All Subtypes)

Legend:
- Vehicle
- IBMX 500 µM
- Ascomycin 10 nM
- Ascomycin 100 nM
- Ascomycin 1 µM

Time (h)	IBMX 500 µM	Ascomycin 10 nM	100 nM	1 µM
1	X			
5	X			
24	X		X	X

Time (h)	IBMX 500 µM	Ascomycin 1 µM	100 nM	10 nM
1	X	X	X	
5	X	X	X	
24	X	X	X	X
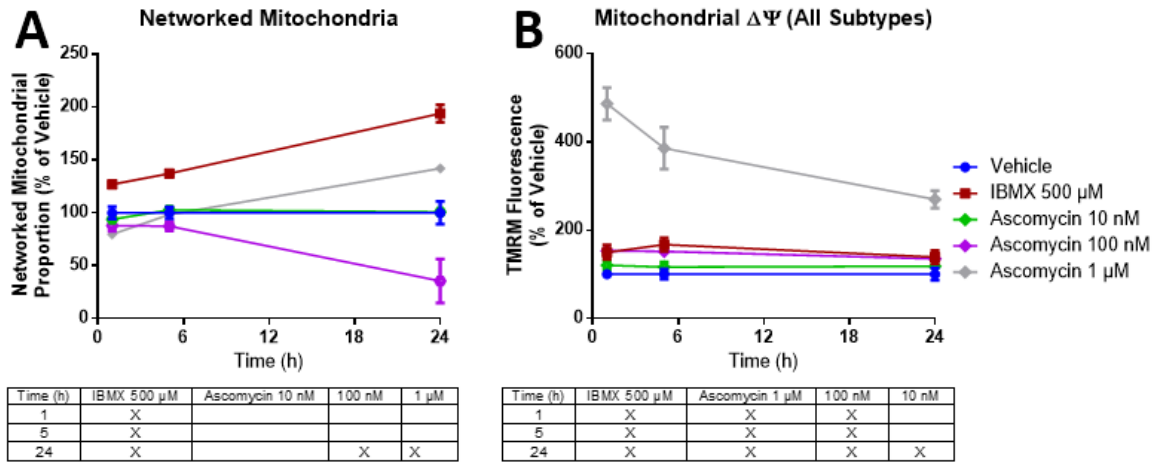
Supplementary Figure 13. Calcineurin (Ppp3ca) inhibition alters networked morphology and increases mitochondrial membrane potential.

661w photoreceptor cell line mitochondria were subjected to morphological and membrane potential analysis as previously described [114]. Proportion of networked mitochondria following 24 h treatment is presented in (A), and mitochondrial membrane potential in (B). Data shown are mean ± s.e.m. of n=4 experiments. "X": multiplicity-adjusted $p < 0.05$. Analyzed by one-way (A) or two-way ANOVA (B), post-test treatment group versus vehicle at each time point.

A Networked Mitochondria

B Mitochondrial ΔΨ (All Subtypes)

Time (h)	IBMX 500 µM	3F8 10 nM	100 nM	1 µM
1	X			
5	X			
24	X			

Time (h)	IBMX 500 µM	3F8 100 nM	1 µM
1	X	X	X
5	X	X	X
24	X		
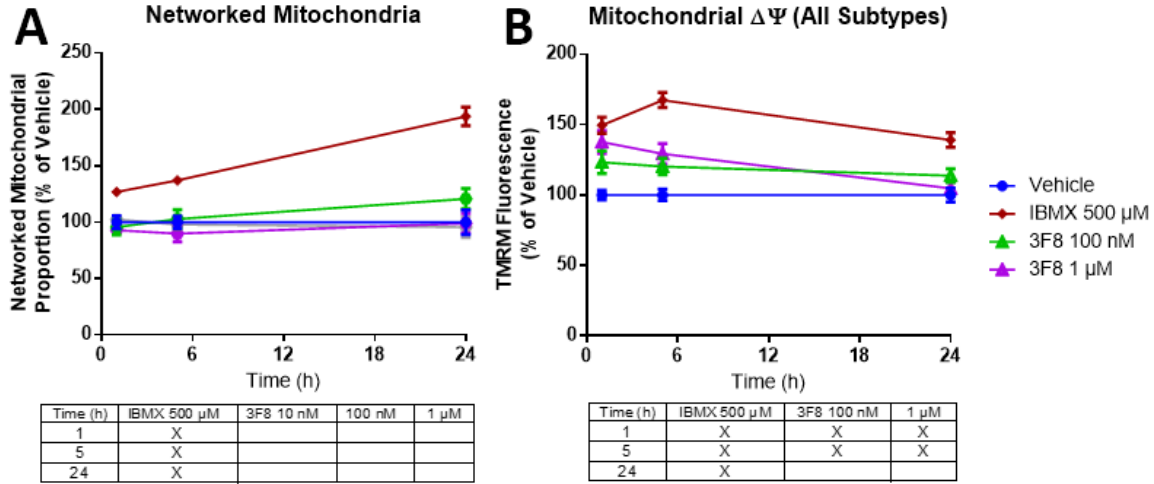
Supplementary Figure 14. GSK3-β (Gsk3b) inhibition transiently increases mitochondrial membrane potential.

661w photoreceptor cell line mitochondria were subjected to morphological and membrane potential analysis as previously described [114]. Proportion of networked mitochondria following 24 h treatment is presented in (A), and mitochondrial membrane potential in (B). Data shown are mean ± s.e.m. of n=4 experiments. "X": multiplicity-adjusted $p < 0.05$. Analyzed by one-way (A) or two-way ANOVA (B), post-test treatment group versus vehicle at each time point.

10. Appendix B—Computer Programs

10.1 dPsi.R: Example usage of data analysis functions

```
#########
#Mitochondrial Membrane Potential (dPsi) Analysis
#High Content Microscopic Analysis of Mitochondrial Morphology and
#Membrane Potential Using Morphological Binning
#2014, Anthony Leonard et. al. <leonara@musc.edu>, <apleonard@gmail.com>
#########


#change these to match the location of saved files from Supplementary File 3.zip
source('.\\annotateData.R')
source(".\\plotDensity.R")
library(XLConnect) #available in CRAN


#first load and annotate data


#load the platemap
yfile<-".\\platemaps.xlsx"
yfile<-file.choose() #use if not saved in same directory as this file


y=readWorksheet(loadWorkbook(yfile), sheet="8-2 dPsi")


#paste in locations of the datafile(s) extracted (Default C:/R/)


files<-c(
  "C:\\R\\n1 1h.csv",
  "C:\\R\\n2 1h.csv",
```

```
  "C:\\R\\n3 1h.csv",
  "C:\\R\\n4 1h.csv"
)
```

```
#using annotateData.R, includes analysis group info
#setting platenames=0 automatically assigns experimental n and time point to each plate
#e.g. a file named n2 1h.csv will set plate=2 and time=1
alldata<-
        batchAnnotate(files,y,fixText=TRUE,fixNAAreas=TRUE,platenames=1:4,xlsfiles=
        FALSE)
```

```
#save results
write.table(alldata,file="C:\\R\\dPsi.csv",sep=",",na="",dec=".",row.names=FALSE,col.names=TR
        UE)
```

```
#reload results from csv table (if already annotated, see data export at end of file)
# alldata <- read.csv(file=file.choose(),header=TRUE,sep=",")
```

```
#verify import integrity
str(alldata)
```

```
# make sure that group is treated as a number
alldata$group<-as.numeric(alldata$group)
```

```
#Generating Figure 6d (Oligomycin v. vehicle v. FCCP)
```

```
# calculate background-corrected intensity values
# by subtracting nuclear intensity
alldata$AllMitoBGCy3<-mapply(FUN=function(x,y) ifelse(is.na(x) | is.na(y),NA,max(x-y,0)),
              x=alldata$AllMitoCy3Intensity, y=alldata$NucCy3Intensity)
alldata$NetBGCy3<-mapply(FUN=function(x,y) ifelse(is.na(x) | is.na(y),NA,max(x-y,0)),
              x=alldata$NetCy3Intensity, y=alldata$NucCy3Intensity)
```

```
alldata$RodBGCy3<-mapply(FUN=function(x,y) ifelse(is.na(x) | is.na(y),NA,max(x-y,0)),
                x=alldata$RodCy3Intensity, y=alldata$NucCy3Intensity)
alldata$PunBGCy3<-mapply(FUN=function(x,y) ifelse(is.na(x) | is.na(y),NA,max(x-y,0)),
                x=alldata$PunCy3Intensity, y=alldata$NucCy3Intensity)
alldata$SwoBGCy3<-mapply(FUN=function(x,y) ifelse(is.na(x) | is.na(y),NA,max(x-y,0)),
                x=alldata$SwoCy3Intensity, y=alldata$NucCy3Intensity)


#calculate proportional data
#first, fix the NA values for zero area (they are indeed zero)
bkup<-alldata
alldata$NetTotalArea<-mapply(function(x) ifelse(is.na(x),0,x),x=alldata$NetTotalArea)
alldata$RodTotalArea<-mapply(function(x) ifelse(is.na(x),0,x),x=alldata$RodTotalArea)
alldata$PunTotalArea<-mapply(function(x) ifelse(is.na(x),0,x),x=alldata$PunTotalArea)
alldata$SwoTotalArea<-mapply(function(x) ifelse(is.na(x),0,x),x=alldata$SwoTotalArea)


#then calculate proportion of subtype area (divide by total area in each cell)
alldata$NetMitoP<-mapply(FUN=function(x,y) x/y, alldata$NetTotalArea, alldata$AllMitoArea)
alldata$RodMitoP<-mapply(FUN=function(x,y) x/y, alldata$RodTotalArea, alldata$AllMitoArea)
alldata$PunMitoP<-mapply(FUN=function(x,y) x/y, alldata$PunTotalArea, alldata$AllMitoArea)
alldata$SwoMitoP<-mapply(FUN=function(x,y) x/y, alldata$SwoTotalArea, alldata$AllMitoArea)


#set the groups used for plotting (defined in platemaps.xlsx)
groups<-c(1,18,5)
summary(alldata$AllMitoBGCy3[which(alldata$group %in% groups)])
# exclude plate 1 which had no response (oligomycin solubility)
plotDensity(dataset=alldata[which(alldata$plate!=1),],plotvar="AllMitoBGCy3",groups=groups,yli
                m=c(0.0001,0.25),xlim=c(0,150),addpvalues=FALSE)


grep("Pos",colnames(alldata))
#columns 3 and 4 are X and y location of cells, respectively
summary(alldata[,3:4])
#subset out the extreme edge cells (registration adds a bright white border, values invalid)
```

#removes the strange spikes in mitochondrial membrane potential (AllMitoBGCy3)
subset<-alldata[which(alldata[,3]>20 & alldata[,3]<360 & alldata[,4]>20 & alldata[,4]<360),]

#Plot for Figure 6d:
plotDensity(dataset=subset[which(subset$plate!=1),],plotvar="AllMitoBGCy3",groups=groups,yli
            m=c(0,0.3),xlim=c(0,150),addpvalues=FALSE,xlab="Background-Corrected
            TMRM Intensity (AU)",title="")

#Calculation of Kolmogorov-Smirnov statistics for comparisons in Figure 6d
#Vehicle v. FCCP 1 uM
ks.test(alldata$AllMitoBGCy3[which(alldata$treatment=="Vehicle")],
     alldata$AllMitoBGCy3[which(alldata$group==18)])

#vehicle versus oligomycin 10 uM
ks.test(alldata$AllMitoBGCy3[which(alldata$treatment=="Vehicle")],
     alldata$AllMitoBGCy3[which(alldata$group==5)])

#vehicle versus FCCP 1 uM
ks.test(alldata$AllMitoBGCy3[which(alldata$group==18)],
     alldata$AllMitoBGCy3[which(alldata$group==5)])

#Help to pick out representative cells for Figure 6 panels a-c:
#Control representative
summary(alldata$AllMitoBGCy3[which(alldata$treatment=="Vehicle")],na.rm=TRUE)
vcpick<-alldata[which(alldata$treatment=="Vehicle" &
                alldata$AllMitoBGCy3<30 & alldata$AllMitoBGCy3>29 &
                alldata$AllMitoArea<63 & alldata$AllMitoArea>62),]

#FCCP representative
summary(alldata$AllMitoBGCy3[which(alldata$group==18)],na.rm=TRUE)
fccppick<-alldata[which(alldata$group==18 &
                alldata$AllMitoBGCy3<2.7 & alldata$AllMitoBGCy3>2.2 &

```
                alldata$AllMitoArea<16 & alldata$AllMitoArea>15),]


#oligomycin representative

summary(alldata$AllMitoBGCy3[which(alldata$group==5)],na.rm=TRUE)

oligopick<-alldata[which(alldata$group==5 &

                alldata$AllMitoBGCy3<78 & alldata$AllMitoBGCy3>73 &

                alldata$AllMitoArea<72 & alldata$AllMitoArea>69),]

#end representative cell picking


#Other example plots (not in publication):

plotDensity(dataset=subset[which(subset$plate!=1),],plotvar="NetBGCy3",groups=groups,ylim=
                c(0,0.25),xlim=c(0,150),addpvalues=FALSE,xlab="Background-Corrected
                Networked TMRM Intensity (AU)",title="Networks")

plotDensity(dataset=subset[which(subset$plate!=1),],plotvar="RodBGCy3",groups=groups,ylim=
                c(0,0.3),xlim=c(0,150),addpvalues=FALSE,xlab="Background-Corrected Rod
                TMRM Intensity (AU)",title="Rods")

plotDensity(dataset=subset[which(subset$plate!=1),],plotvar="PunBGCy3",groups=groups,ylim=
                c(0,0.3),xlim=c(0,150),addpvalues=FALSE,xlab="Background-Corrected Puncta
                TMRM Intensity (AU)",title="Puncta")

plotDensity(dataset=subset[which(subset$plate!=1),],plotvar="SwoBGCy3",groups=groups,ylim
                =c(0,0.1),xlim=c(0,150),addpvalues=FALSE,xlab="Background-Corrected Large
                & Round TMRM Intensity (AU)",title="Large & Round")


#test for normality

summary(subset$SwoBGCy3[which(subset$group==1)])

test<-subset$SwoBGCy3[which(subset$group==1 & subset$plate!=1)]

testnorm<-test/mean(test, na.rm=TRUE)

testnorm<-testnorm[which(!is.na(testnorm))]

sd(testnorm)

ref<-rnorm(length(testnorm),mean=1,sd(testnorm))

plot(sort(ref),sort(testnorm),xlim=c(0,3),ylim=c(0,3),xlab="Normal Distribution",ylab="Normalized
                Swollen TMRM Intensity")

lines(x=c(0,3),y=c(0,3))

ks.test(ref,testnorm)
```

text(labels="Kolmogorov-Smirnov test p value: 0.8992",x=1.0,y=2.7)

#k-s test returns p value of 0.8992, suggesting the data are normally distributed

#thus, we have no evidence to suggest that there is a bimodal distrubtion of TMRM intensity
                within swollen subpopulation

#examples of data export:

#save all data

write.csv(alldata,file="C:/r/dPsi mitoproportion analysis.csv")

#automated collation of data (by mean or median, see line 170) for graphing software, e.g.
                GraphPad Prism 6.0

#first set: (membrane potential studies)

grep("BGCy3",colnames(alldata))

#columns 106-110 are the variables of interest

vars<-106:110

#second set: (morphometric studies)

grep("MitoP",colnames(alldata))

#columns 111-114 are the variables of interest

vars<-111:114

#to export all variables

vars<-106:114

#export in tab-delimited text (use Microsoft Excel to open files (wizard guides import), then copy
                and paste to GraphPad)

for (i in vars)

{

  x=tapply(subset[,i][which(subset$group %in% groups)],

        INDEX=list(subset$plate[which(subset$group %in% groups)],

```
            subset$treatment[which(subset$group %in% groups)],

            subset$time[which(subset$group %in% groups)]),

        FUN=median,na.rm=TRUE)


            write.ftable(ftable(x,row.vars=3,col.vars=c(2,1)),sep=",",file=file.path("C:/R",paste
            (colnames(subset)[i],".txt",sep="")),lsep=",",method="compact")

}


#example file structure:
# ""  "Vehicle"                        (TREATMENT)
#,        "1"      "2"      "3"      "4"   (EXPERIMENTAL REPLICATE)
# "1"      30.5900  31.4980  28.6390  28.5355
# "2"      27.7100  33.8690  32.0895  29.7730
# "3"      29.2220  35.0730  32.0790  30.3250
# "4"      31.3430  37.1510  34.4820  31.5570
# "5"      33.4670  36.7395  34.7665  32.4240


#time points (in hours on the y axis)

#experimental replicates are split across the x, first by treatment group, and then by plate # (true
            replicate)Supplementary Figure 1
```

10.2 plotDensity.R: a function for density plotting and hypothesis testing

```
#######################
# Conditional inference machine-learning based method for mitochondrial
# classification.  Leonard et. al. 2014 "Automated High Content Analysis
# of Mitochondrial Morphology and Membrane Potential Using
# Morphological Binning"

# plotDensity - a function for density plotting and hypothesis testing
# Plots a univariate data distribution from one or more groups
# Calculates the median for each group (by subgroups, such as an experiment)
# and performs multiple t-tests with Holm-Sidak's correction for
# multiple comparisons, reporting p values

# Author contact information: Anthony Leonard: apleonard@gmail.com
#######################

library(plotrix)
plotDensity<-function(dataset,groups,plotvar="AllMitoTMRM", ylim=c(0,70),xlim=c(1,1.6),

                colors=c("black","darkred","blue","darkgreen","slategray1","tomato","yellowgreen"
                ,"orange"),

                addpvalues=TRUE,trimdata=TRUE,pairFUN="median",legendloc=0.5,title="defa
                ult",xlab=plotvar,...) {
  if(title=="default") {
    title=unique(dataset$treatment[which(dataset$group==groups[2])])
    title=substr(title,1,regexpr(" [0-9]{1,4} ",title)-1)
    title=paste(title,"-",plotvar)
    title=paste(title,"-",unique(dataset$time),"h")
  }
  groupnames=as.character(dataset$treatment[match(groups,dataset$group)])
  nplates=1:length(groups)
```

```r
ncells=1:length(groups)
#plot the first instance of the variable found in the dataset matching
var<-grep(plotvar,colnames(dataset))[[1]]

if(trimdata)
  dataset<-dataset[which(dataset[,var]<xlim[2] & dataset[,var]>xlim[1]),]

for (i in 1:length(groups)) {
  if (!i==1) {
    lines(density(dataset[,var][which(dataset$group==groups[i])]),col=colors[i],lwd=2)


  }
  else (
    plot(kern<-
              density(dataset[,var][which(dataset$group==groups[i])]),xlim=xlim,ylim=ylim,main
              =title,lwd=2,xlab=xlab,ylab="Kernel Density Estimate")
  )
  nplates[i] = length(unique(dataset$plate[which(dataset$group==groups[i])]))
  ncells[i] = length(dataset$plate[which(dataset$group==groups[i])])
  groupnames[i] <- paste("G",groups[i],": ",groupnames[i]," | N=",nplates[i]," exps., n=",ncells[i],"
              cells",sep="")
}

legend(x=xlim[1]+((legendloc-0.15)*(xlim[2]-xlim[1])),y=ylim[2]-(0.0*ylim[2]-
              ylim[1]),legend=groupnames,bty="n",
      fill=colors#, border=c("black","dark red","blue")
      ,bg="light gray",box.lwd=2)

if(pairFUN=="median") {
  x=tapply(X=dataset[,var][which(dataset$group %in% groups)],
      INDEX=list(dataset$group[which(dataset$group %in% groups)],
              dataset$plate[which(dataset$group %in% groups)]),
      FUN=median,na.rm=TRUE)
```

```r
#make the array pretty
attr(x,"dimnames")[[1]]<-paste("G",groups,sep="")


#names take up too much space, use group # instead
#uncomment the line below if your dataset has a 'treatment' variable that you'd prefer versus
        a group number


        #factor(x=attr(x,"dimnames")[[1]],levels=groups,labels=as.character(dataset$treat
        ment[match(sort(groups),dataset$group)]))


x2<-stack(data.frame(t(x)))


#now perform pairwise t tests by row (or transpose and go by column...)
test<-pairwise.t.test(x=x2$values,g=x2$ind,p.adjust.method="holm")


}
else if (pairFUN=="mean") {
 x=tapply(dataset[,var][which(dataset$group %in% groups)],
        INDEX=list(dataset$group[which(dataset$group %in% groups)],
                dataset$plate[which(dataset$group %in% groups)]),
        FUN=mean,na.rm=TRUE)


 #names take up too much space, use group # instead
 #uncomment the line below if your dataset has a 'treatment' variable that you'd prefer versus
        a group number


        #factor(x=attr(x,"dimnames")[[1]],levels=groups,labels=as.character(dataset$treat
        ment[match(sort(groups),dataset$group)]))


x2<-stack(data.frame(t(x)))


#now perform pairwise t tests by row (or transpose and go by column...)
```

```
    test<-pairwise.t.test(x=x2$values,g=x2$ind,p.adjust.method="holm")


  }
  else {
    print("pairwise stats function not understood, all data points treated as individual
                experiments")
    print("use 'mean' or 'median' for meaningful stats")
    test<-pairwise.t.test(x=x,

                  g=dataset$group[which(dataset$group %in% groups)], p.adj = "holm")
  }

if(addpvalues) {
    stats=round(test$p.value,digits=5)
    addtable2plot(x=xlim[1]+(legendloc*(xlim[2]-xlim[1])),y=ylim[2]-(0.5*(ylim[2]-
                ylim[1])),xjust=0,yjust=0,
            display.colnames=TRUE,display.rownames=TRUE, hlines=TRUE,vlines=TRUE,
            table=stats,title="Pairwise t-tests w/ Holm-Sidak Correction")
  }
  return(test)
}
```

10.3 annotateData.R: a function for annotation of GE INCell Analyzer Developer Toolbox high content analysis data output (v. 1.9.1)

```
#################
# Conditional inference machine-learning based method for mitochondrial
# classification.  Leonard et. al. 2013 "Automated High Content Analysis
# of Mitochondrial Morphology and Membrane Potential Using
# Morphological Binning"

# annotateData - a function for annotating high content imaging data
# obtained from the GE INCell Analyzer 2000 automated epifluorescence
# microscope and INCell Developer Toolbox. Accepts two inputs:
# a platemap spreadsheet and the unannotated cytometric data output
# from Developer Toolbox (one row of data per cell)

# Author contact information: Anthony Leonard: apleonard@gmail.com
#################

options (java.parameters = "-Xmx8024m")
library(XLConnect)

#example usage:
#x<-annotateData(platedata=readWorksheet(loadWorkbook(choose.files(caption = "Select Data
            Sheet",multi=FALSE)),sheet="Cytoplasm"),
#           platemap=readWorksheet(loadWorkbook(choose.files(caption = "Select
            PlateMap")),sheet=1),
#           fixNAAreas=TRUE, fixText=TRUE, platename=1, time=1);

annotateData <- function (x=dataframe,y=platemap, fixNAAreas=TRUE, fixtext=TRUE,
            platename=NULL,time=0) {
  #annotate all cells with well, column, row, field, and time
  #assign group numbers to treatments, and label these numbers using factor()
```

```r
#first, set up a few vars
x$well = as.character("A - 0");

x$row = as.character("A");

x$col = as.numeric(0)

x$rownum = as.numeric(0)

x$wellnum = as.numeric(0)

x$time = as.numeric(time)

x$group = as.numeric(0)

x$rep = as.numeric(0)

x$field =as.numeric(1);


x$treatment = "A"


if(is.null(platename)) {
  #do nothing
}
else if(is.numeric(platename)) {
  x$plate <- as.numeric(platename)
}
else {
  x$plate = as.factor(platename)
}


if(!is.na(y[23,3])) # initialize analysis group only if there is data to use
{
  x$anzgroup = as.numeric(0)
}


#next, define the regions from platemap for replicate and grouping data
txlist <- y[33:128,2]
```

```
group <- y[12:19,2:13]
rep <- y[34:41,6:17]
anzgroup <- y[22:29,2:13]

#shorten txlist to only have valid (nonzero) groups
txlabels = which(!is.na(txlist))

#Now assign the metadata to each row
x$well=sapply(x[,1],FUN=substr,start=1,stop=6);
x$row=sapply(x[,1],FUN=substr,start=1,stop=1);
x$col=sapply(x$well,FUN=getCol);
x$rownum = sapply(x$row,FUN=getRowNum);
x$field = sapply(x[,1],FUN=fieldFind);
x$wellnum = mapply(FUN=getWellNum,x$rownum,x$col);
x$group <- mapply(function(row,column) as.numeric(group[row, column]), x$rownum, x$col);
x$rep <- mapply(function(row,column) rep[row, column], x$rownum, x$col)
x$treatment <- factor(x$group,levels=1:length(txlabels),
                labels=txlist[1:length(txlabels)],exclude=0)
x$anzgroup <- mapply(function(row,column) anzgroup[row,column], x$rownum, x$col)

#use this function to get rid of the " um2" that gets added to all of the measures
if(fixNAAreas) {
  cols2Replace= c(grep("Area",colnames(x), ignore.case=
              TRUE),grep("InThisCell",colnames(x), ignore.case=
              TRUE),grep("tPerim",colnames(x), ignore.case= TRUE))
  xsub<-x[,cols2Replace]
  xsub[is.na(xsub)] <- 0
  x[,cols2Replace] <- xsub
}

cols2Fix = grep("Pos",colnames(x), ignore.case= TRUE)
```

```r
  #only run this function if the user wants it run and it is needed (a number input into trimChars()
              returns an NA)
  if(fixtext && !is.numeric(x[1,cols2Fix[1]])) {
    xsub<-x[,cols2Fix];
    x[,cols2Fix] <- apply(xsub,MARGIN=2,FUN=trimChars)
  }


  #ensure that measures that can be read as numeric are forced to be numeric
  for (i in 1:length(x[1,])) {
    if (is.numeric(x[,i]))
      x[,i]<-as.numeric(x[,i])
  }


  return (as.data.frame(x))
}


getRowNum <- function(row="A") {
  result=0;
  for (i in 1:26) {
    if (LETTERS[i]==row)
      result=i;
  }
  return (result)
}


getCol <- function(well="A - 1") {
  result=0;
  result=as.numeric(substr(well,5,6));
  return(result)
}


getWellNum <- function(rownum,colnum) {
```

```
return((rownum-1)*12 + colnum);
}


fieldFind <- function(str="A - 1 (fld 1)") {
  field = substr(str,start=regexpr("fld",str)+4,stop=regexpr(")",str)-1)


  if (field=="") {
    return (1)
  }
  else return(as.numeric(field))
}


trimLoc <- function(input="4.01 µm") { # function returns the location of the first non-digit for
                substringing and converting values to numeric
  return(regexpr(pattern="[^0-9.]",text=input));
  #above function necessary since some data columns from InCellAnalyzer Dev Toolbox
                obligatorily add "um" to label values
}


trimChars <- function(inputstring = "14.107 pixel") {
  if (is.numeric(inputstring))
    result=inputstring
  else {
    result=as.numeric(substr(x=inputstring, start=1, stop=trimLoc(inputstring)))
  }
  return(result)
}


# a wrapper function that reads in plate number and time information from the directory in which
              files are stored
# e.g. n1 1h reads in plate # 1, 1 hour time point
```

```
batchAnnotate <-
            function(filelist,platemap,fixText=TRUE,fixNAAreas=TRUE,platenames=1:99,xlsfi
            les=FALSE,sheet="Cytoplasm",startRow=2,...) {
 original<-data.frame();
 excluded<-data.frame();
 result<-data.frame();
 x<-data.frame()


 for (i in 1:length(filelist)) {
  rowtitle <-paste("plate",i)
  nowdir<-dirname(filelist[i])
  nowname<-basename(filelist[i])
  if(regexpr("[n][0-9]{1,2}[ ][0-9]{1,2}[h]",nowdir,ignore.case=TRUE)==-1)
  {#if the n1 1h format isn't found in the directory path, then use the filename to find it
    nowdir<-nowname
  }
  infoloc<-regexpr("[n][0-9]{1,2}[ ][0-9]{1,2}[h]",nowdir,ignore.case=TRUE)
  metadata<-substr(nowdir,start=infoloc,stop=infoloc + attr(infoloc,"match.length")-1)
  timeloc<-regexpr("[0-9]{1,2}[h]",metadata,ignore.case=TRUE)
  time<-as.numeric(substr(metadata,start=timeloc,stop=timeloc+attr(timeloc,"match.length")-2))
  if(platenames[1]==0)
  {
    plate<-as.numeric(substr(metadata,start=2,stop=attr(regexpr("[n][0-
            9]{1,2}",metadata,ignore.case=TRUE),"match.length")))
  }
  else
  {
    plate<-platenames[i]
  }

  if(xlsfiles) {
```

```r
#read in the cytometric data from Dev toolbox

platedata<-
              readWorksheet(loadWorkbook(filename=filelist[i]),sheet=sheet,startRow=startRo
              w)
}
else {
  platedata<-read.csv(file=filelist[i],header=TRUE,sep=",",dec=".",skip=1)
}
#annotate using annotateData function

#    x<-annotateData(...,platedata, platemap, fixNAAreas,
#                fixText,
#                platename=plate, time=time)
  tryCatch(x<-annotateData(...,platedata, platemap, fixNAAreas,
                      fixText,
                      platename=plate, time=time),error = function(e) {
                        print(paste("Error Annotating",filelist[i])) #for debugging
                        e})
if (i==1) {
  original<-x[which(!is.na(x[,2])),]
}
else {
  cols <- intersect(colnames(original), colnames(x))
  original<-rbind(original[,cols], x[which(!is.na(x[,2])),cols])
}
x$metadata<-metadata
}

# at the very end, make sure (one last time!) that all variables that can be treated as numeric
              are.
for (i in 1:length(original[1,])) {
```

```r
    if (is.numeric(original[,i]))
      original[,i]<-as.numeric(original[,i])
  }
  #and finally drop the mysterious "X" column if it still exists, without removing Pos..X
  cols2 <- setdiff(grep("X",colnames(original)),grep(".X",colnames(original)))
  if(length(cols2)==1)
    original<-original[,c(1:(cols2-1),(cols2+1):ncol(original))]
  return (original)
}
```

10.4 parallelImageReg.R: a function to parallelize image registration

###############

wrapper function to parallelize image registration

Anthony Leonard, <leonara@musc.edu>

default behavior is to split the task up according to number of processor cores

Images are registered sequentially, saving the original, unregistered image in the
     "unregistered" subdirectory

###############

library(oro.nifti)

library(tiff)

library(parallel)

library(RNiftyReg)

affinelistold <- c(.002061,-3.436325e-05,0,0,7.618232e-05,1.002105,0,0,0,0,1,0,2.209438,-
     2.706979,0,1);

affinelist <- c(1.00198,-1.37093e-05,0,0,7.60416e-07,1.00205,0,0,0,0,1,0,3.55669,-2.04304,0,1)

affine <- matrix(affinelist, 4, 4);

#Function usage:

#suggested usage at end of file (just "source" this file to run interactively)

#source is image that is out of alignment (e.g. Cy3 filter imaged TMRM stained mitochondria)

#target is image that contains the true location of source image

#(in focus slice of MitoTracker Deep Red stained mitochondria)

#ncores=0 (default) uses all available cores

#suppresswarning is recommended to be set as TRUE unless a job is stopped prior to
     completion

#optimize is a switch that when TRUE adapts the initial affine to match each image (slower,
     more accurate)

and when FALSE, just applies the affine that is defined using the parameters on lines 84
     and 85

parImageReg<-
     function(source,target,affine,ncores=0,suppresswarning=TRUE,optimize=TRUE)

```
{
  if(file.exists(file.path(dirname(source[1]),"unregistered"))) {
    if(!suppresswarning){
      r<-readline(prompt="/unregistered subdirectory exists, registration may have already been
                  performed - do you wish to continue? (y/n)")
      if(r=="n" | r=="N") {
        stop("execution stopped, images/directory not modified")
      }
      r<-readline(prompt="Do you wish to register only the unregistered images?")
      if(r=="y" | r=="Y") {
        print("eliminating registered images from list")
        print(paste("original image count:",length(source)))
        list<-!file.exists(file.path(dirname(source),"unregistered",basename(source)))
        source<-source[which(list)]
        target<-target[which(list)]
        print(paste("unregistered images found:",length(source)))
        if(length(source)==0 | is.null(source)){
          stop("No images to register!")
        }
      }
    }
    else{
      print("eliminating registered images from list")
      print(paste("original image count:",length(source)))
      list<-!file.exists(file.path(dirname(source),"unregistered",basename(source)))
      source<-source[which(list)]
      target<-target[which(list)]
      print(paste("unregistered images found:",length(source)))
      if(length(source)==0 | is.null(source)){
        stop("No images to register!")
      }
    }
```

```
}
else {
  print("Setting read/write permissions")
  Sys.chmod(list.dirs(file.path(dirname(source[1]))),"777")
  f <- list.files(list.dirs(file.path(dirname(source[1]))), all.files = TRUE, full.names = TRUE,
              recursive = TRUE);
  Sys.chmod(f, (file.info(f)$mode | "664"))
  print("Creating 'unregistered' subdirectory for original files")
  dir.create(file.path(dirname(source[1]),"unregistered"))
}


#initialize the cluster
#default to use all cores available
if(ncores==0) {
  cl<-makePSOCKcluster(names<-detectCores())
  print(paste(names, "processors detected,", names, "processors will be used"))
}
else  {
  cl<-makePSOCKcluster(names<-min(ncores,detectCores()))
  print(paste(detectCores(), "processors detected,", names, "processors will be used"))
}


imagelist<-cbind(source,target)
#definitely want to have the algorithm save images as it goes along
print("Beginning image registration")
clusterMap(cl, fun=function(x,y,z=optimize){
  library(oro.nifti)
  library(tiff)
  library(parallel)
  library(RNiftyReg)
  affinelist <- c(.002061,-3.436325e-05,0,0,7.618232e-05,1.002105,0,0,0,0,1,0,2.209438,-
              2.706979,0,1);
```

```r
    affine <- matrix(affinelist, 4, 4);

    print("copying file to unregistered")

    file.copy(x,file.path(dirname(x),"unregistered",basename(x)))

    print(paste("analyzing:",x))

    if(optimize)

    {

      writeTIFF(what=niftyreg.linear(as.nifti(readTIFF(x)), as.nifti(readTIFF(y)),

                        scope="affine", initAffine=affine, verbose=FALSE, nLevels=2)[1],

          where=x, bits.per.sample=16, reduce=TRUE)

    }
#    else { #nonfunctional
#      writeTIFF(what=applyAffine(affine=affine,as.nifti(readTIFF(x)), as.nifti(readTIFF(y)))[1],
#            where=x, bits.per.sample=16, reduce=TRUE)
#    }
    else {

      writeTIFF(what=niftyreg.linear(as.nifti(readTIFF(x)), as.nifti(readTIFF(y)),

                        scope="affine", initAffine=affine, verbose=FALSE, nLevels=0)[1],

          where=x, bits.per.sample=16, reduce=TRUE)

    }
  }, x=imagelist[,1], y=imagelist[,2])


  print("Killing Cluster")

  stopCluster(cl)

  print("Cluster killed, waiting 5 seconds")

  Sys.sleep(time=5)

  print("Image Stack Completed, Please Kill R process to free memory")


  return("Image Stack Completed")
}


# regImage<-function(source,target){
```

```r
#   library(oro.nifti)
#   library(tiff)
#   library(parallel)
#   library(RNiftyReg)
#   affinelist <- c(.002061,-3.436325e-05,0,0,7.618232e-05,1.002105,0,0,0,0,1,0,2.209438,-
                2.706979,0,1);
#   affine <- matrix(affinelist, 4, 4);
#   writeTIFF(what=niftyreg.linear(as.nifti(readTIFF(source)), as.nifti(readTIFF(target)),
#                     scope="affine", initAffine=affine, verbose=FALSE, nLevels=2)[1],
#           where=source, bits.per.sample=16, reduce=TRUE)
# }


getImageList<-function(source="Cy3 - Cy3",source2=NULL) {
 print("Please select the first in focus MTDR Image")
 file<-file.choose()
 zloc<-regexpr(pattern=" z [0-9]{1,3}",basename(file))
 z<-as.numeric(substr(basename(file),zloc+3,zloc-1+attr(zloc,"match.length")))
 zsearch<-paste(" z ",z,sep="")
 dirloc<-dirname(file)
 filelist<-dir(dirname(file))
 targetlist<-filelist[which(grepl(zsearch,filelist)&!grepl("poly",filelist))]
 sourcelist<-filelist[which(grepl(source,filelist)&!grepl("poly",filelist))]
 if(!is.null(source2)) {
   sourcelist2<-filelist[which(grepl(source2,filelist)&!grepl("poly",filelist))]
   imagelist<-cbind(file.path(dirloc,sourcelist),file.path(dirloc,targetlist),
               file.path(dirloc,sourcelist2))
 }
 else {
   imagelist<-cbind(file.path(dirloc,sourcelist),file.path(dirloc,targetlist))
 }
 print(paste(nrow(imagelist),"images (sets) to analyze"))
 return(imagelist)
```

```
}
```

#general usage for aligning two images to another image that is very simliar

#(e.g. TMRM in Cy3 to MitoTracker Deep Red in Cy5 and NAO in FITC to MitoTracker Deep Red in Cy5)

imagepaths<-getImageList("Cy3 - Cy3","Cy3 - Cy5")

print(imagepaths[1,1])

parImageReg(imagepaths[,1],imagepaths[,2],affine,ncores=8)

parImageReg(imagepaths[,3],imagepaths[,2],affine,ncores=8)

# #

print(imagepaths[1,1])

#for Brett's Imaging 3/13/14

imagepaths<-getImageList("Cy3 - Cy3","FITC - FITC")

#print out the first Cy3 image so we can keep track of which image the algorithm is working on

print(imagepaths[1,3])

#register Cy3 images

parImageReg(imagepaths[,1],imagepaths[,2],affine,ncores=8,optimize=TRUE) #set optimize=TRUE only if Cy3 images are TMRM or some other mitochondrial stain

#register FITC images

print("First set of images done, registering second set")

parImageReg(imagepaths[,3],imagepaths[,2],affine,ncores=8,optimize=TRUE) #in this case, we know CellROX Green

#(in the FITC channel, column 3 of imagepaths) does not line up with mitochondria,

#so we set optimize=FALSE to use stored affine transformation

#print out the first image again so we can keep track of which image the algorithm just finished

print(imagepaths[1,1])

11. Bibliography

1. Leonard, A.P., et al., *A high-content, live-cell, and real-time approach to the quantitation of ligand-induced beta-Arrestin2 and Class A/Class B GPCR mobilization.* Microsc Microanal, 2013. **19**(1): p. 150-70.

2. Ferrick, D.A., A. Neilson, and C. Beeson, *Advances in measuring cellular bioenergetics using extracellular flux.* Drug Discovery Today, 2008. **13**(5-6): p. 268-274.

3. Sharma, A.K. and B. Rohrer, *Sustained elevation of intracellular cGMP causes oxidative stress triggering calpain-mediated apoptosis in photoreceptor degeneration.* Curr Eye Res, 2007. **32**(3): p. 259-69.

4. Perron, N.R., C. Beeson, and B. Rohrer, *Early alterations in mitochondrial reserve capacity; a means to predict subsequent photoreceptor cell death.* J Bioenerg Biomembr, 2013. **45**(1-2): p. 101-9.

5. Pagon, R.A., *Retinitis pigmentosa.* Surv Ophthalmol, 1988. **33**(3): p. 137-77.

6. Daiger, S.P., L.S. Sullivan, and S.J. Bowne, *Genes and mutations causing retinitis pigmentosa.* Clin Genet, 2013. **84**(2): p. 132-41.

7. Sahni, J.N., et al., *Therapeutic challenges to retinitis pigmentosa: from neuroprotection to gene therapy.* Curr Genomics, 2011. **12**(4): p. 276-84.

8. Caspi, R.R., *Ocular autoimmunity: the price of privilege?* Immunol Rev, 2006. **213**: p. 23-35.

9. *Online Mendelian Inheritance in Man, OMIM®.* 2014, McKusick-Nathans Institute of Genetic Medicine, Johns Hopkins University: Baltimore, MD.

10. Vlachantoni, D., et al., *Evidence of severe mitochondrial oxidative stress and a protective effect of low oxygen in mouse models of inherited photoreceptor degeneration.* Hum Mol Genet, 2011. **20**(2): p. 322-35.

11. Portera-Cailliau, C., et al., *Apoptotic photoreceptor cell death in mouse models of retinitis pigmentosa.* Proc Natl Acad Sci U S A, 1994. **91**(3): p. 974-8.

12. Lasansky, A. and E. De Robertis, *Submicroscopic analysis of the genetic distrophy of visual cells in C3H mice.* J Biophys Biochem Cytol, 1960. **7**: p. 679-84.

13. Farber, D.B. and R.N. Lolley, *Cyclic guanosine monophosphate: elevation in degenerating photoreceptor cells of the C3H mouse retina.* Science, 1974. **186**(4162): p. 449-51.

14. Carter-Dawson, L.D., M.M. LaVail, and R.L. Sidman, *Differential effect of the rd mutation on rods and cones in the mouse retina.* Invest Ophthalmol Vis Sci, 1978. **17**(6): p. 489-98.

15. Doonan, F., M. Donovan, and T.G. Cotter, *Activation of multiple pathways during photoreceptor apoptosis in the rd mouse.* Invest Ophthalmol Vis Sci, 2005. **46**(10): p. 3530-8.

16. Miller, W.H., R.E. Gorman, and M.W. Bitensky, *Cyclic adenosine monophosphate: function in photoreceptors.* Science, 1971. **174**(4006): p. 295-7.

17. Ukena, D., C. Schudt, and G.W. Sybrecht, *Adenosine receptor-blocking xanthines as inhibitors of phosphodiesterase isozymes.* Biochem Pharmacol, 1993. **45**(4): p. 847-51.

18. al-Ubaidi, M.R., et al., *Bilateral retinal and brain tumors in transgenic mice expressing simian virus 40 large T antigen under control of the human interphotoreceptor retinoid-binding protein promoter.* J Cell Biol, 1992. **119**(6): p. 1681-7.

19. Tan, E., et al., *Expression of cone-photoreceptor-specific antigens in a cell line derived from retinal tumors in transgenic mice.* Invest Ophthalmol Vis Sci, 2004. **45**(3): p. 764-8.

20. Tang, P.H., et al., *RPE65 is present in human green/red cones and promotes photopigment regeneration in an in vitro cone cell model.* J Neurosci, 2011. **31**(50): p. 18618-26.

21. Liu, C., T. Sherpa, and M.D. Varnum, *Disease-associated mutations in CNGB3 promote cytotoxicity in photoreceptor-derived cells.* Mol Vis, 2013. **19**: p. 1268-81.

22. Fitzgerald, J.B., et al., *Functional expression of cone cyclic nucleotide-gated channel in cone photoreceptor-derived 661W cells.* Adv Exp Med Biol, 2008. **613**: p. 327-34.

23. Ames, A., 3rd and M. Barad, *Metabolic flux of cyclic GMP and phototransduction in rabbit retina.* J Physiol, 1988. **406**: p. 163-79.

24. Zhang, X., Q. Feng, and R.H. Cote, *Efficacy and Selectivity of Phosphodiesterase-Targeted Drugs in Inhibiting Photoreceptor Phosphodiesterase (PDE6) in Retinal Photoreceptors.* Investigative Ophthalmology & Visual Science, 2005. **46**(9): p. 3060-3066.

25. Bender, A.T. and J.A. Beavo, *Cyclic nucleotide phosphodiesterases: molecular regulation to clinical use.* Pharmacol Rev, 2006. **58**(3): p. 488-520.

26. Wallis, R.M., *The pharmacology of sildenafil, a novel and selective inhibitor of phosphodiesterase (PDE) type 5.* Nihon Yakurigaku Zasshi, 1999. **114 Suppl 1**: p. 22P-26P.

27. Turko, I.V., et al., *Inhibition of cyclic GMP-binding cyclic GMP-specific phosphodiesterase (Type 5) by sildenafil and related compounds.* Mol Pharmacol, 1999. **56**(1): p. 124-30.

28. Sanyal, S. and A.K. Bal, *Comparative light and electron microscopic study of retinal histogenesis in normal and rd mutant mice.* Z Anat Entwicklungsgesch, 1973. **142**(2): p. 219-38.

29. McLaughlin, M.E., et al., *Recessive mutations in the gene encoding the beta-subunit of rod phosphodiesterase in patients with retinitis pigmentosa.* Nat Genet, 1993. **4**(2): p. 130-4.

30. Paquet-Durand, F., et al., *A key role for cyclic nucleotide gated (CNG) channels in cGMP-related retinitis pigmentosa.* Hum Mol Genet, 2011. **20**(5): p. 941-7.

31. Barabas, P., C. Cutler Peck, and D. Krizaj, *Do Calcium Channel Blockers Rescue Dying Photoreceptors in the Pde6b (rd1) Mouse?* Adv Exp Med Biol, 2010. **664**: p. 491-9.

32. Paquet-Durand, F., et al., *PKG activity causes photoreceptor cell death in two retinitis pigmentosa models.* J Neurochem, 2009. **108**(3): p. 796-810.

33. Nivison-Smith, L., et al., *Sildenafil alters retinal function in mouse carriers of Retinitis Pigmentosa.* Exp Eye Res, 2014. **128**: p. 43-56.

34. Ignarro, L.J., et al., *Endothelium-derived relaxing factor produced and released from artery and vein is nitric oxide.* Proc Natl Acad Sci U S A, 1987. **84**(24): p. 9265-9.

35. Russwurm, M., et al., *NO/cGMP: the past, the present, and the future.* Methods Mol Biol, 2013. **1020**: p. 1-16.

36. Whitaker, R.M., et al., *cGMP-selective phosphodiesterase inhibitors stimulate mitochondrial biogenesis and promote recovery from acute kidney injury.* J Pharmacol Exp Ther, 2013. **347**(3): p. 626-34.

37. Maurice, D.H., et al., *Advances in targeting cyclic nucleotide phosphodiesterases.* Nat Rev Drug Discov, 2014. **13**(4): p. 290-314.

38. Asirvatham, A.L., et al., *A-kinase anchoring proteins interact with phosphodiesterases in T lymphocyte cell lines.* J Immunol, 2004. **173**(8): p. 4806-14.

39. Rogne, M., et al., *Mutually exclusive binding of PP1 and RNA to AKAP149 affects the mitochondrial network.* Hum Mol Genet, 2009. **18**(5): p. 978-87.

40. Merrill, R.A., et al., *Mechanism of neuroprotective mitochondrial remodeling by PKA/AKAP1.* PLoS Biol, 2011. **9**(4): p. e1000612.

41. Li, H., et al., *Adenosine and Dopamine Receptors Coregulate Photoreceptor Coupling via Gap Junction Phosphorylation in Mouse Retina.* J Neurosci, 2013. **33**(7): p. 3135-50.

42.   Philipp, S., et al., *Postconditioning protects rabbit hearts through a protein kinase C-adenosine A2b receptor cascade.* Cardiovasc Res, 2006. **70**(2): p. 308-14.

43.   Cohen, M.V., C.P. Baines, and J.M. Downey, *Ischemic preconditioning: from adenosine receptor to KATP channel.* Annu Rev Physiol, 2000. **62**: p. 79-109.

44.   Grenz, A., et al., *The Reno-Vascular A2B Adenosine Receptor Protects the Kidney from Ischemia.* PLoS Med, 2008. **5**(6): p. e137.

45.   Dos Santos-Rodrigues, A., et al., *Nucleoside transporters in the purinome.* Neurochem Int, 2014.

46.   Mundell, S.J., J.L. Benovic, and E. Kelly, *A dominant negative mutant of the G protein-coupled receptor kinase 2 selectively attenuates adenosine A2 receptor desensitization.* Mol Pharmacol, 1997. **51**(6): p. 991-8.

47.   Mundell, S.J., et al., *Arrestin isoforms dictate differential kinetics of A2B adenosine receptor trafficking.* Biochemistry, 2000. **39**(42): p. 12828-36.

48.   Crosson, C.E., R. DeBenedetto, and J.M. Gidday, *Functional evidence for retinal adenosine receptors.* J Ocul Pharmacol, 1994. **10**(2): p. 499-507.

49.   Brandli, A. and J. Stone, *Remote ischemia influences the responsiveness of the retina: observations in the rat.* Invest Ophthalmol Vis Sci, 2014. **55**(4): p. 2088-96.

50.   Rey, H.L. and B. Burnside, *Adenosine stimulates cone photoreceptor myoid elongation via an adenosine A2-like receptor.* J Neurochem, 1999. **72**(6): p. 2345-55.

51.   McIntosh, H.H. and C. Blazynski, *Characterization and localization of adenosine A2 receptors in bovine rod outer segments.* J Neurochem, 1994. **62**(3): p. 992-7.

52.   Blazynski, C. and H. McIntosh, *Characterization of adenosine A2 receptors in bovine retinal membranes.* Exp Eye Res, 1993. **56**(5): p. 585-93.

53.   Krishnamoorthy, R.R., et al., *Characterization of a transformed rat retinal ganglion cell line.* Brain Res Mol Brain Res, 2001. **86**(1-2): p. 1-12.

54.   Krishnamoorthy, R.R., et al., *A forensic path to RGC-5 cell line identification: lessons learned.* Invest Ophthalmol Vis Sci, 2013. **54**(8): p. 5712-9.

55.   Sippl, C. and E.R. Tamm, *What is the Nature of the RGC-5 Cell Line?* Adv Exp Med Biol, 2014. **801**: p. 145-54.

56.   Ju, W.K., et al., *Elevated hydrostatic pressure triggers mitochondrial fission and decreases cellular ATP in differentiated RGC-5 cells.* Invest Ophthalmol Vis Sci, 2007. **48**(5): p. 2145-51.

57.   Ju, W.K., et al., *Elevated hydrostatic pressure triggers release of OPA1 and cytochrome C, and induces apoptotic cell death in differentiated RGC-5 cells.* Mol Vis, 2009. **15**: p. 120-34.

58.   Cassidy-Stone, A., et al., *Chemical Inhibition of the Mitochondrial Division Dynamin Reveals Its Role in Bax/Bak-Dependent Mitochondrial Outer Membrane Permeabilization.* Dev Cell, 2008. **14**(2): p. 193-204.

59.   Frank, S., et al., *The Role of Dynamin-Related Protein 1, a Mediator of Mitochondrial Fission, in Apoptosis.* Developmental Cell, 2001. **1**(4): p. 515-525.

60.   Chang, C.R. and C. Blackstone, *Cyclic AMP-dependent protein kinase phosphorylation of Drp1 regulates its GTPase activity and mitochondrial morphology.* J Biol Chem, 2007. **282**(30): p. 21583-7.

61.   Tanaka, A. and R.J. Youle, *A chemical inhibitor of DRP1 uncouples mitochondrial fission and apoptosis.* Mol Cell, 2008. **29**(4): p. 409-10.

62.   Yamano, K. and R.J. Youle, *Coupling mitochondrial and cell division.* Nat Cell Biol, 2011. **13**(9): p. 1026-7.

63.   Karbowski, M., et al., *Role of Bax and Bak in mitochondrial morphogenesis.* Nature, 2006. **443**(7112): p. 658-62.

64.	Wang, H., et al., *Parkin ubiquitinates Drp1 for proteasome-dependent degradation: implication of dysregulated mitochondrial dynamics in Parkinson disease.* J Biol Chem, 2011. **286**(13): p. 11649-58.

65.	Waterham, H.R., et al., *A Lethal Defect of Mitochondrial and Peroxisomal Fission.* New England Journal of Medicine, 2007. **356**(17): p. 1736-1741.

66.	Ishihara, N., et al., *Mitochondrial fission factor Drp1 is essential for embryonic development and synapse formation in mice.* Nature Cell Biology, 2009. **11**(8): p. 958-966.

67.	Lee, Y.-j., et al., *Roles of the Mammalian Mitochondrial Fission and Fusion Mediators Fis1, Drp1, and Opa1 in Apoptosis.* Mol. Biol. Cell, 2004. **15**(11): p. 5001-5011.

68.	Yamaguchi, R., et al., *Opa1-mediated cristae opening is Bax/Bak and BH3 dependent, required for apoptosis, and independent of Bak oligomerization.* Mol Cell, 2008. **31**(4): p. 557-69.

69.	Youle, R.J. and A.M. van der Bliek, *Mitochondrial fission, fusion, and stress.* Science, 2012. **337**(6098): p. 1062-5.

70.	Zhan, M., et al., *Mitochondrial dynamics: regulatory mechanisms and emerging role in renal pathophysiology.* Kidney Int, 2013. **83**(4): p. 568-81.

71.	Chevrollier, A., et al., *Standardized mitochondrial analysis gives new insights into mitochondrial dynamics and OPA1 function.* Int J Biochem Cell Biol, 2012. **44**(6): p. 980-8.

72.	Peng, J.Y., et al., *Automatic morphological subtyping reveals new roles of caspases in mitochondrial dynamics.* PLoS Comput Biol, 2011. **7**(10): p. e1002212.

73.	Lihavainen, E., et al., *Mytoe: Automatic analysis of mitochondrial dynamics.* Bioinformatics, 2012. **28**(7): p. 1050-1.

74.	Reis, Y., et al., *Multi-Parametric Analysis and Modeling of Relationships between Mitochondrial Morphology and Apoptosis.* PLoS ONE, 2012. **7**(1): p. e28694.

75.	Koopman, W.J., et al., *Simultaneous quantitative measurement and automated analysis of mitochondrial morphology, mass, potential, and motility in living human skin fibroblasts.* Cytometry A, 2006. **69**(1): p. 1-12.

76.	Hothorn, T., K. Hornik, and A. Zeileis, *Unbiased Recursive Partitioning: A Conditional Inference Framework.* Journal of Computational and Graphical Statistics, 2006. **15**(3): p. 651-674.

77.	Thompson, C.M. *Detecting a Cell Using Image Segmentation*. 2013 [cited 2013 9/4/2013]; R2013a:[MATLAB Version R2013a Documentation, Image Processing Toolbox, Image Processing Toolbox Examples]. Available from: http://www.mathworks.com/help/images/examples/detecting-a-cell-using-image-segmentation.html.

78.	Buades, A., B. Coll, and J. Morel, *A Review of Image Denoising Algorithms, with a New One.* Multiscale Modeling & Simulation, 2005. **4**(2): p. 490-530.

79.	Robert J. Marks, I., *6.2.1 The Nyquist Density*, in *Introduction to Shannon Sampling and Interpolation Theory*. 1991, Springer Verlag: New York. p. 322.

80.	Collins, T.J., et al., *Mitochondria are morphologically and functionally heterogeneous within cells.* EMBO J, 2002. **21**(7): p. 1616-27.

81.	Therneau, T., *rpart: Recursive Partitioning*. 2013. p. Recursive partitioning and regression trees.

82.	Breiman, L. *Random Forests*. 2004 [cited 2012 March 1]; A Description of the Random Forest algorithm for machine learning-based classification]. Available from: http://www.stat.berkeley.edu/~breiman/RandomForests/cc_home.htm.

83.	Clayden, J., *RNiftyReg*. 2013. p. RNiftyReg: Medical image registration using the NiftyReg library. Based on original code by Marc Modat and Pankaj Daga.

84.	Bates, D., *R: A Language and Environment for Statistical Computing*. 2013, R Foundation for Statistical Computing: Vienna, Austria. p. R: A Language and Environment for Statistical Computing.

85.   Ferrick, D.A., A. Neilson, and C. Beeson, *Advances in measuring cellular bioenergetics using extracellular flux.* Drug Discov Today, 2008. **13**(5-6): p. 268-74.

86.   Lenth, R., *Java Applets for Power and Sample Size* 2006-2009: University of Iowa. p. Java Applets for Power and Sample Size.

87.   Steyerberg, E.W., et al., *Internal and external validation of predictive models: a simulation study of bias and precision in small samples.* J Clin Epidemiol, 2003. **56**(5): p. 441-7.

88.   Van Houwelingen, J.C. and S. Le Cessie, *Predictive value of statistical models.* Stat Med, 1990. **9**(11): p. 1303-25.

89.   Funk, J.A., S. Odejinmi, and R.G. Schnellmann, *SRT1720 Induces Mitochondrial Biogenesis and Rescues Mitochondrial Function After Oxidant Injury in Renal Proximal Tubule Cells.* J Pharmacol Exp Ther, 2010. **333**(2): p. 593-601.

90.   Kakkar, P., S. Mehrotra, and P.N. Viswanathan, *tBHP induced in vitro swelling of rat liver mitochondria.* Mol Cell Biochem, 1996. **154**(1): p. 39-45.

91.   Masaki, N., et al., *Mitochondrial damage as a mechanism of cell injury in the killing of cultured hepatocytes by tert-butyl hydroperoxide.* Arch Biochem Biophys, 1989. **270**(2): p. 672-80.

92.   Koopman, W.J., et al., *Mammalian Mitochondrial Complex I: Biogenesis, Regulation and Reactive Oxygen Species Generation.* Antioxid Redox Signal, 2010. **12**(12): p. 1431-70.

93.   Rieske, J.S., *Changes in oxidation-reduction potential of cytochrome b observed in the presence of antimycin A.* Arch Biochem Biophys, 1971. **145**(1): p. 179-93.

94.   Symersky, J., et al., *Oligomycin frames a common drug-binding site in the ATP synthase.* Proc Natl Acad Sci U S A, 2012. **109**(35): p. 13961-5.

95.   Pilati, C.F. and N.F. Paradise, *Ouabain-induced mechanical toxicity: aberrations in left ventricular function, calcium concentration, and ultrastructure.* Proc Soc Exp Biol Med, 1984. **175**(3): p. 342-50.

96.   Lemasters, J.J., et al., *Measurement of electrical potential, pH, and free calcium ion concentration in mitochondria of living cells by laser scanning confocal microscopy.* Methods Enzymol, 1995. **260**: p. 428-44.

97.   Distelmaier, F., et al., *Life cell quantification of mitochondrial membrane potential at the single organelle level.* Cytometry A, 2008. **73**(2): p. 129-38.

98.   Lemasters, J.J., et al., *The mitochondrial permeability transition in cell death: a common mechanism in necrosis, apoptosis and autophagy.* Biochim Biophys Acta, 1998. **1366**(1-2): p. 177-96.

99.   Saunders, J.E., C.C. Beeson, and R.G. Schnellmann, *Characterization of functionally distinct mitochondrial subpopulations.* J Bioenerg Biomembr, 2013. **45**(1-2): p. 87-99.

100.   Suranyi, E.M. and Y. Avi-Dor, *Effect of Potassium and Ouabain on Swelling of Rat Liver Mitochondria.* Biochem Biophys Res Commun, 1965. **19**: p. 215-30.

101.   Blondin, G.A. and D.E. Green, *The mechanism of mitochondrial swelling.* Proc Natl Acad Sci U S A, 1967. **58**(2): p. 612-9.

102.   Distelmaier, F., et al., *Trolox-sensitive reactive oxygen species regulate mitochondrial morphology, oxidative phosphorylation and cytosolic calcium handling in healthy cells.* Antioxid Redox Signal, 2012. **17**(12): p. 1657-69.

103.   Lemasters, J.J., *Selective mitochondrial autophagy, or mitophagy, as a targeted defense against oxidative stress, mitochondrial dysfunction, and aging.* Rejuvenation Res, 2005. **8**(1): p. 3-5.

104.   Lemasters, J.J., et al., *Mitochondrial calcium and the permeability transition in cell death.* Biochim Biophys Acta, 2009. **1787**(11): p. 1395-401.

105.   Wang, X., et al., *Superoxide flashes: elemental events of mitochondrial ROS signaling in the heart.* J Mol Cell Cardiol, 2012. **52**(5): p. 940-8.

106. Orvedahl, A., et al., *Image-based genome-wide siRNA screen identifies selective autophagy factors.* Nature, 2011. **480**(7375): p. 113-7.
107. Hasson, S.A., et al., *High-content genome-wide RNAi screens identify regulators of parkin upstream of mitophagy.* Nature, 2013. **504**(7479): p. 291-5.
108. Gomes, L.C. and L. Scorrano, *Mitochondrial morphology in mitophagy and macroautophagy.* Biochimica et Biophysica Acta (BBA) - Molecular Cell Research, 2013. **1833**(1): p. 205-212.
109. Suen, D.F., et al., *Parkin overexpression selects against a deleterious mtDNA mutation in heteroplasmic cybrid cells.* Proc Natl Acad Sci U S A, 2010. **107**(26): p. 11835-40.
110. Lightowlers, R.N., et al., *Mammalian mitochondrial genetics: heredity, heteroplasmy and disease.* Trends in Genetics, 1997. **13**(11): p. 450-455.
111. Carelli, V., et al., *Retinal ganglion cell neurodegeneration in mitochondrial inherited disorders.* Biochim Biophys Acta, 2009. **1787**(5): p. 518-28.
112. Amiott, E.A., et al., *Mitochondrial fusion and function in Charcot-Marie-Tooth type 2A patient fibroblasts with mitofusin 2 mutations.* Exp Neurol, 2008. **211**(1): p. 115-27.
113. Valsecchi, F., et al., *Primary fibroblasts of NDUFS4(-/-) mice display increased ROS levels and aberrant mitochondrial morphology.* Mitochondrion, 2012. **13**(5): p. 436-43.
114. Leonard, A.P., et al., *Quantitative analysis of mitochondrial morphology and membrane potential in living cells using high-content imaging, machine learning, and morphological binning.* Biochim Biophys Acta, 2014. **1853**(2): p. 348-360.
115. Sharma, A.K. and B. Rohrer, *Calcium-induced Calpain Mediates Apoptosis via Caspase-3 in a Mouse Photoreceptor Cell Line.* J. Biol. Chem., 2004. **279**(34): p. 35564-35572.
116. Rohrer, B., et al., *Multidestructive pathways triggered in photoreceptor cell death of the rd mouse as determined through gene expression profiling.* J Biol Chem, 2004. **279**(40): p. 41903-10.
117. Maldonado, E.N., et al., *Free tubulin modulates mitochondrial membrane potential in cancer cells.* Cancer Res, 2010. **70**(24): p. 10192-201.
118. Lemasters, J.J., et al., *Regulation of mitochondrial function by voltage dependent anion channels in ethanol metabolism and the Warburg effect.* Biochim Biophys Acta, 2012. **1818**(6): p. 1536-44.
119. Park, J.-S., et al., *Parkinson's disease-associated human ATP13A2 (PARK9) deficiency causes zinc dyshomeostasis and mitochondrial dysfunction.* Human Molecular Genetics, 2014.
120. Souness, J.E., et al., *Evidence that cyclic AMP phosphodiesterase inhibitors suppress TNF alpha generation from human monocytes by interacting with a 'low-affinity' phosphodiesterase 4 conformer.* Br J Pharmacol, 1996. **118**(3): p. 649-58.
121. Smith, S.J., et al., *Discovery of BRL 50481 [3-(N,N-dimethylsulfonamido)-4-methyl-nitrobenzene], a Selective Inhibitor of Phosphodiesterase 7: In Vitro Studies in Human Monocytes, Lung Macrophages, and CD8+ T-Lymphocytes.* Molecular Pharmacology, 2004. **66**(6): p. 1679-1689.
122. Boess, F.G., et al., *Inhibition of phosphodiesterase 2 increases neuronal cGMP, synaptic plasticity and memory performance.* Neuropharmacology, 2004. **47**(7): p. 1081-92.
123. Hidaka, H., et al., *Selective inhibitor of platelet cyclic adenosine monophosphate phosphodiesterase, cilostamide, inhibits platelet aggregation.* J Pharmacol Exp Ther, 1979. **211**(1): p. 26-30.
124. Lohr, H.R., et al., *Multiple, parallel cellular suicide mechanisms participate in photoreceptor cell death.* Exp Eye Res, 2006. **83**(2): p. 380-9.
125. Lolley, R.N., H. Rong, and C.M. Craft, *Linkage of photoreceptor degeneration by apoptosis with inherited defect in phototransduction.* Investigative Ophthalmology & Visual Science, 1994. **35**(2): p. 358-62.

126. Fox, D.A., A.T. Poblenz, and L. He, *Calcium overload triggers rod photoreceptor apoptotic cell death in chemical-induced and inherited retinal degenerations.* Ann N Y Acad Sci, 1999. **893**: p. 282-5.

127. Griciuc, A., et al., *Proteomic survey reveals altered energetic patterns and metabolic failure prior to retinal degeneration.* J Neurosci, 2014. **34**(8): p. 2797-812.

128. D. Piwnica, S.R.W., T. Jolas, G. Néliat, B. Fouchaq, *Inverse agonist properties of the A2A adenosine receptor antagonist IBMX in HEK 293 cells.* 2006.

129. Ribelayga, C. and S.C. Mangel, *A circadian clock and light/dark adaptation differentially regulate adenosine in the mammalian retina.* J Neurosci, 2005. **25**(1): p. 215-22.

130. Zimmerman, M.A., et al., *Signaling through hepatocellular A2B adenosine receptors dampens ischemia and reperfusion injury of the liver.* Proc Natl Acad Sci U S A, 2013. **110**(29): p. 12012-7.

131. Eckle, T., et al., *Adora2b-elicited Per2 stabilization promotes a HIF-dependent metabolic switch crucial for myocardial adaptation to ischemia.* Nat Med, 2012. **18**(5): p. 774-82.

132. Laubach, V.E., B.A. French, and M.D. Okusa, *Targeting of adenosine receptors in ischemia-reperfusion injury.* Expert Opin Ther Targets, 2011. **15**(1): p. 103-18.

133. Porkka-Heiskanen, T., et al., *Adenosine: a mediator of the sleep-inducing effects of prolonged wakefulness.* Science, 1997. **276**(5316): p. 1265-8.

134. McIntosh, V.J. and R.D. Lasley, *Adenosine receptor-mediated cardioprotection: are all 4 subtypes required or redundant?* J Cardiovasc Pharmacol Ther, 2012. **17**(1): p. 21-33.

135. Headrick, J.P., et al., *Cardiovascular adenosine receptors: expression, actions and interactions.* Pharmacol Ther, 2013. **140**(1): p. 92-111.

136. Haas, H.L. and O. Selbach, *Functions of neuronal adenosine receptors.* Naunyn Schmiedebergs Arch Pharmacol, 2000. **362**(4-5): p. 375-81.

137. Jacobson, K.A., et al., *G protein-coupled adenosine (P1) and P2Y receptors: ligand design and receptor interactions.* Purinergic Signal, 2012. **8**(3): p. 419-36.

138. Nicholson, C.D., S.A. Jackman, and R. Wilke, *The ability of denbufylline to inhibit cyclic nucleotide phosphodiesterase and its affinity for adenosine receptors and the adenosine re-uptake site.* Br J Pharmacol, 1989. **97**(3): p. 889-97.

139. Fiebich, B.L., et al., *IL-6 expression induced by adenosine A2b receptor stimulation in U373 MG cells depends on p38 mitogen activated kinase and protein kinase C.* Neurochem Int, 2005. **46**(6): p. 501-12.

140. Bruce Alberts, A.J., Julian Lewis, Martin Raff, Keith Roberts, and Peter Walter, *Molecular Biology of The Cell.* 4th ed. 2002: Garland Science.

141. Wu-Zhang, A.X. and A.C. Newton, *Protein kinase C pharmacology: refining the toolbox.* Biochem J, 2013. **452**(2): p. 195-209.

142. Saraiva, L., et al., *Characterization of phorbol esters activity on individual mammalian protein kinase C isoforms, using the yeast phenotypic assay.* Eur J Pharmacol, 2004. **491**(2-3): p. 101-10.

143. Bogoyevitch, M.A., P.J. Parker, and P.H. Sugden, *Characterization of protein kinase C isotype expression in adult rat heart. Protein kinase C-epsilon is a major isotype present, and it is activated by phorbol esters, epinephrine, and endothelin.* Circ Res, 1993. **72**(4): p. 757-67.

144. Schulte, G. and B.B. Fredholm, *The G(s)-coupled adenosine A(2B) receptor recruits divergent pathways to regulate ERK1/2 and p38.* Exp Cell Res, 2003. **290**(1): p. 168-76.

145. Iancu, R.V., et al., *Cytoplasmic cAMP concentrations in intact cardiac myocytes.* American Journal of Physiology - Cell Physiology, 2008. **295**(2): p. C414-C422.

146. Kuno, A., et al., *Protein kinase C protects preconditioned rabbit hearts by increasing sensitivity of adenosine A2b-dependent signaling during early reperfusion.* J Mol Cell Cardiol, 2007. **43**(3): p. 262-71.

147. Costa, A.D., et al., *cGMP signalling in pre- and post-conditioning: the role of mitochondria.* Cardiovasc Res, 2008. **77**(2): p. 344-52.

148. Gong, J., et al., *Two protein kinase C isoforms, delta and epsilon, regulate energy homeostasis in mitochondria by transmitting opposing signals to the pyruvate dehydrogenase complex.* FASEB J, 2012. **26**(8): p. 3537-49.

149. Grube, K., et al., *Evidence for an intracellular localization of the adenosine A2B receptor in rat cardiomyocytes.* Basic Res Cardiol, 2011. **106**(3): p. 385-96.

150. Di Benedetto, G., et al., *Mitochondrial Ca2+ Uptake Induces Cyclic AMP Generation in the Matrix and Modulates Organelle ATP Levels.* Cell Metabolism, 2013. **17**(6): p. 965-975.

151. Acin-Perez, R., et al., *A phosphodiesterase 2A isoform localized to mitochondria regulates respiration.* J Biol Chem, 2011. **286**(35): p. 30423-32.

152. Schulte, G. and B.B. Fredholm, *Signalling from adenosine receptors to mitogen-activated protein kinases.* Cellular Signalling, 2003. **15**(9): p. 813-827.

153. Yang, X., et al., *A2B adenosine receptors inhibit superoxide production from mitochondrial complex I in rabbit cardiomyocytes via a mechanism sensitive to Pertussis toxin.* Br J Pharmacol, 2011. **163**(5): p. 995-1006.

154. Hua, X., et al., *Gs-coupled adenosine receptors differentially limit antigen-induced mast cell activation.* J Pharmacol Exp Ther, 2013. **344**(2): p. 426-35.

155. Thimm, D., et al., *Ligand-specific binding and activation of the human adenosine A(2B) receptor.* Biochemistry, 2013. **52**(4): p. 726-40.

156. Cohen, M.V., X. Yang, and J.M. Downey, *A(2b) adenosine receptors can change their spots.* Br J Pharmacol, 2010. **159**(8): p. 1595-7.

157. Valsecchi, F., et al., *cAMP and mitochondria.* Physiology (Bethesda), 2013. **28**(3): p. 199-209.

158. Schmitz, A.L., et al., *A cell-permeable inhibitor to trap Galphaq proteins in the empty pocket conformation.* Chem Biol, 2014. **21**(7): p. 890-902.